DESIGN OF A 2R1T MECHANISM WITH REMOTE CENTER OF MOTION FOR MINIMALLY INVASIVE TRANSNASAL SURGERY APPLICATIONS

A Thesis Submitted to the
Graduate School of Engineering and Sciences of
İzmir Institute of Technology
in Partial Fulfillment of the Requirements for the Degree of

MASTER OF SCIENCE

in Mechanical Engineering

by
Abdullah YAŞIR

July 2018
İZMİR

We approve the thesis of **Abdullah YAŞIR**

Examining Committee Members:

Prof. Dr. Enver TATLICIOĞLU
Department of Electrical & Electronics Engineering, İzmir Institute of Technology

Assoc. Prof. Dr. Gökhan KİPER
Department of Mechanical Engineering, İzmir Institute of Technology

Assist. Prof. Dr. Erkin GEZGİN
Department of Mechatronics Engineering, İzmir Katip Çelebi University

6 July 2018

Assoc. Prof. Dr. Gökhan KİPER
Supervisor
Department of Mechanical Engineering
İzmir Institute of Technology

Assoc. Prof. Dr. M. İ. Can DEDE
Co-Supervisor
Department of Mechanical Engineering
İzmir Institute of Technology

Prof. Dr. Metin TANOĞLU
Head of the Department of
Mechanical Engineering

Prof. Dr. Aysun SOFUOĞLU
Dean of the Graduate School of
Engineering and Sciences

ACKNOWLEDGMENTS

First and foremost, I would like to express my deepest and sincere gratitude to my supervisor Assoc. Prof. Dr. Gökhan Kiper for his inspirational perspective and his ceaseless guidance throughout my academic life. I also would like to express my sincere gratitude to my co-advisor Assoc. Prof. Dr. Mehmet İsmet Can Dede for his insight and encouragement throughout this research project.

I would like to thank my jury members; Prof. Dr. Enver Tatlıcıoğlu and Assist. Prof. Dr. Erkin Gezgin for their attendance at my thesis defence seminar and their valuable recommendations.

I would like to thank my beloved family for standing by me all the time. I would not be able to complete this study without their trusting support.

Also, I would like to thank my dear friends who share the same laboratory and project with me, especially to my dear friend Oğulcan Işıtman for making this project more fun together. I would especially like to thank Dilay Bodur for her valuable support.

Finally, I would like to thank Mete Aytaç and Coşkun Sakarya for their interest and hardwork in the manufacturing stage.

This study is funded by 1003 - Support Program for R&D Projects in Priority Areas (Öncelikli Alanlar Ar-Ge Projeleri Destekleme Programı) of The Scientific and Technological Research Council of Turkey (TÜBİTAK) with the project name "NeuRoboScope - Robot assisted endoscope control that can be controlled by the surgical tools" and the grant number 115E726.

ABSTRACT

DESIGN OF A 2R1T MECHANISM WITH REMOTE CENTER OF MOTION FOR MINIMALLY INVASIVE TRANSNASAL SURGERY APPLICATIONS

In minimally invasive surgery, use of robotic manipulators is becoming more and more common in order to have more precise operations and better post-operative processes. Such operations are often performed through an incision port (a pivot point) on the patient's body. Since the manipulator should move about the pivot point, it should have a remote center of motion.

In this regard, the main objective of this thesis is designing a 3-dof (degrees-of-freedom) surgical robotic arm that is capable of 2R1T (R: rotation, T: translation) motion pattern and is structured as a remote center of motion mechanism for minimally invasive surgery applications.

First, the structural synthesis of a 3-dof manipulator with 2R1T motion pattern is performed. The synthesized structures also can be used for any kind of 2R1T-type applications. Then, the manipulators with various kinematic structures are evaluated for a transnasal surgery according to several evaluation criteria such as feasibility of construction for a remote center of motion mechanism, ease of balancing, number of links, structural symmetry, decoupling of the joint inputs and the output motion of the platform and the number of actuators connected to the base. The best option is evaluated as a parallel manipulator with two 1 F_0-system and one 1 F_0-1 F_∞-system leg structures. Afterwards, kinematic analysis of the spatial parallel manipulator is formulated with a simplified kinematic model consisting of three intersecting planes so that dimensional design is done for a desired dexterous workspace. Finally, constructional design is completed and a prototype is manufactured and tested.

ÖZET

MİNİMAL İNVAZİV TRANSNAZAL CERRAHİ UYGULAMALARI İÇİN UZAK HAREKET MERKEZLİ 2R1T MEKANİZMASI TASARIMI

Son yıllarda robot manipülatörlerin minimal invaziv cerrahi alanındaki kullanımı daha yüksek operasyon hassasiyetleri ve operasyon sonrasında daha hızlı iyileşme süreçleri sağladıklarından dolayı artış göstermiştir. Bu tip cerrahi operasyonlar hastanın vücuduna açılan ve pivot noktası olarak adlandırılan küçük bir delikten girilerek yapılmaktadır. Manipülatörün, bu nokta etrafında hareket etmesi gereksiniminden dolayı bir uzak hareket merkezine sahip olması gerekmektedir.

Bu bağlamda bu tezin temel hedefi minimal invaziv cerrahi uygulamalarında kullanılmak üzere 3 serbestlik dereceli ve uzak hareket merkezi etrafında 2-dönme 1-öteleme (2R1T) hareketleri yapabilen bir cerrahi robot kol tasarlamaktır.

İlk olarak, 2-dönme 1-öteleme hareketlerine haiz 3 serbestlik dereceli bir manipülatör için yapısal sentez yapıldı. Bu sentez sonucunda elde edilen mimariler aynı zamanda herhangi bir 2R1T uygulaması için de kullanılmaya uygundur. Sonra, bir transnasal cerrahi uygulaması için farklı kinematik yapılara sahip manipülatör alternatifleri belirli değerlendirme kıstaslarına göre karşılaştırıldı. Bu kıstaslara uzak hareket merkezli bir mekanizma olarak üretilebilmeye uygunluk, dengeleme kolaylığı, uzuv sayısı, yapısal simetri, mafsal girdileri ile platform hareket çıktısı arasındaki ilişkinin basitliği ve zemine sabitlenebilecek eyleyici sayısı örnek olarak verilebilir. Yapılan karşılaştırmanın sonucunda en iyi sonuç iki tane 1 F_0 ve bir tane 1 F_0-1 F_∞ kısıt sistemli bacaklardan oluşan ve paralel yapıya sahip bir manipülatör olarak değerlendirildi. Daha sonrasında, seçilen uzaysal paralel manipülatörün kinematik yapısı üç tane kesişen düzleme indirgenerek kinematik analiz yapıldı ve istenen çalışma uzayı için boyutlar eniyilendi. Son olarak, yapılan konstrüksiyonel tasarımından sonra bir prototip üretilip testleri yapıldı.

TABLE OF CONTENTS

LIST OF FIGURES

Figure **Page**

LIST OF TABLES

CHAPTER 1

INTRODUCTION

Use of robotic devices in surgical applications has recently become widespread in the world. Robotic surgery was firstly introduced by laparoscopic cholecystectomy in late 1980s (Vierra, 1995). As robotic systems can provide the movements of a surgeon's hand with a greater precision by no tremor problem, they increase the comfort of surgeon by promoting surgery ergonomics (Baek and Kim, 2014). Some of these devices are directly used in operations while others are being developed as assistive devices. The former type is called a surgical robot, which is controlled by a surgeon to perform a surgical operation. Compared with conventional surgical applications, robotically operated surgeries appear to be more precise because the damage that may be caused by the negligence or fault of the surgeon is reduced (Kuo and Dai, 2009). On the other hand, assistive surgical robots are used in case where a surgeon conducts the surgery, but there is a robot assisting the surgeon for sensing or load carrying purposes. This thesis is on the design of an assistive robotic manipulator for guiding the camera system (endoscope) in a minimal invasive pituitary gland tumor resection surgery. The following sections explain the problem definition, motivation and aim of the thesis.

1.1. Problem Definition

Pituitary gland is an endocrine gland, which secretes vital hormones in human body. Hence, any possible pathologies around this gland like tumors can cause significant health problems (Levy, 2014). These tumors are conventionally treated by opening the scull and applying conventional surgery methods or by using some special surgical tools and an endoscope through the nostril without opening skull. The second method is a type of minimal invasive surgery and is called transnasal/endonasal pituitary surgery, which is more preferable and cost-efficient than the first method (Komotar, 2012). As depicted in Figure 1.1, once the endoscope has been placed through the nostril of the patient, the pituitary gland tumor is removed by surgical tools inserted also through the nostril (Laws et al., 2015). When compared with the conventional methods, using this surgery method results in a decrease in hospitalization time while resulting in an increase in resection

rates of tumors, patient comfort and efficiency of the treatment (Almeida et al., 2015; Berker et al., 2014).

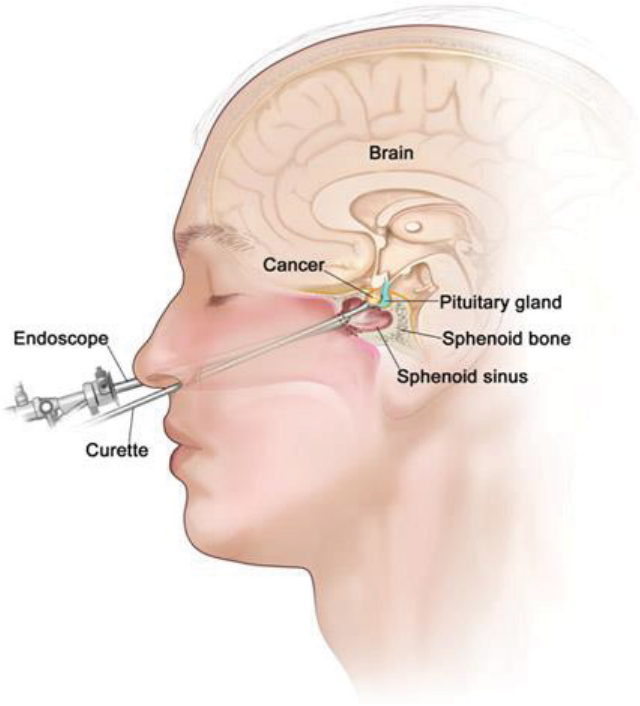

Figure 1.1. Endonasal pituitary surgery
(Source: Best Spine & Neuro Care In India, 2018)

Figure 1.2. Hands of the surgeon and assistant in a surgery
(Source: Dede et al., 2017)

In transnasal surgeries, when the endoscope is manually operated by the surgeon, the surgeon has to spare one hand in order to hold and move the endoscope 2-4 hours

during the surgery (Dede et al., 2017). As a result, the surgeon gets tired and loses his operation efficiency. Figure 1.2 illustrates a surgeon holding the endoscope with his left hand.

Some solutions to eliminate the aforementioned problems are such as getting help from an assistant to hold the endoscope or using a fixed endoscope holder. However, this causes some communication and coordination problems especially in a limited surgical area. On the other hand, fixed endoscope holders are not preferred, because they can only provide a single view angle once the camera angle is set, and it is time consuming to change the view angle. Current problems and their conventional solutions are summarized in Table 1.1. A robotic endoscope holder can be used to overcome these problems.

Table 1.1. Problems in pituitary surgery and its solutions

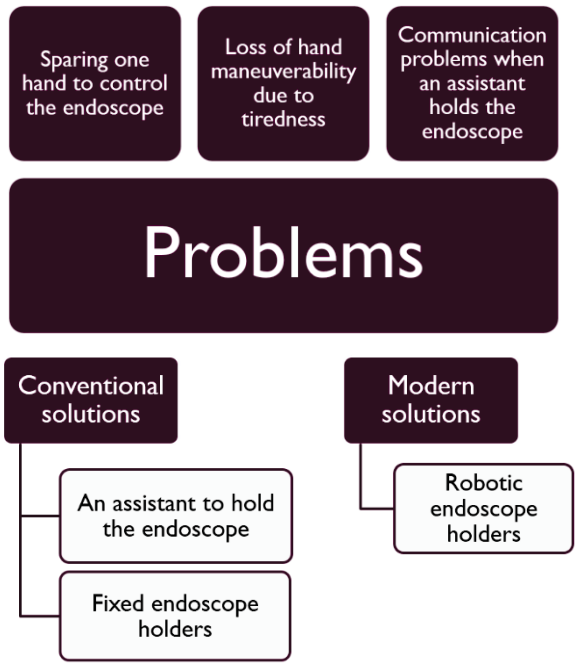

1.2. Aim of the Thesis

To eliminate the problems mentioned in the previous section, Dede et al. (2017) proposed a teleoperation robot system called the name “NeuRoboScope - Robot assisted endoscope control that can be controlled by the surgical tools” to assist the endoscopic pituitary surgery. This robot system has two main mechanical parts: a passive arm and an active arm. The surgeon manually performs the gross motions such as taking the robot

from its home position to the surgical area, by manually backdriving the passive arm which holds the active arm. The active arm is to be designed as a slave component in a teleoperation system that has 3 degrees-of-freedom (dof) 2R1T (R: rotation, T: translation) motion (Dede et al. 2017).

In this context, this thesis concerns with the active endoscope holding part of the robotic system. According to the design requirements listed in Table 1.2, the aim of the thesis is designing a non-parasitic surgical robotic arm with a remote center of motion (RCM) which is capable of 2R1T motion such that an endoscope can be precisely manipulated without damaging the ease of access of the surgeon to the operation area.

Table 1.2. Design requirements of the system

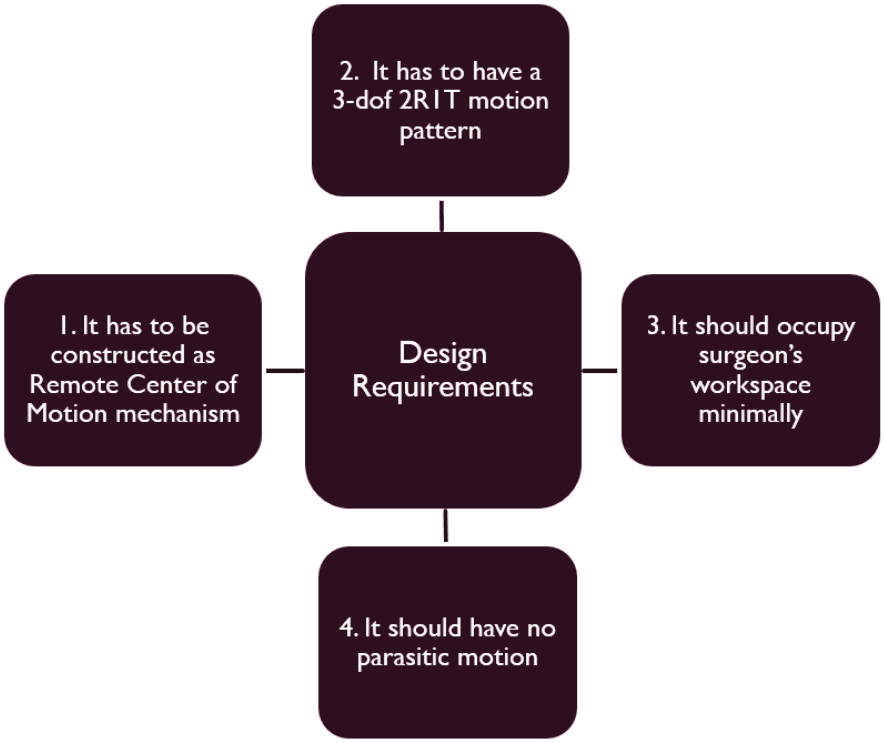

The methodological steps for the design of such a manipulator are given in Table 1.3. The organization of the thesis is constituted in accordance with these steps.

Table 1.3. Methodological steps of the study

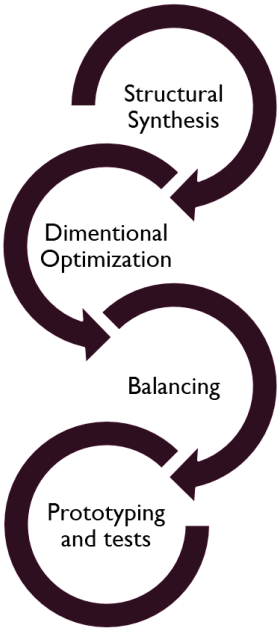

A literature survey on minimal invasive surgery, robotic systems used in these surgeries and their patents are presented in Chapter 2. In Chapter 3, the structural synthesis of a 3-dof manipulator with 2R1T motion pattern and an RCM is carried out. Then, different kinematic structures are evaluated and an appropriate structure is selected. Chapter 4 presents the kinematic analysis of the parallel manipulator selected in Chapter 3. Then, link dimensions are optimized for the desired workspace. In Chapter 5, constructional design, balancing, prototype manufacturing and the tests are presented. Finally, Chapter 6 concludes the thesis.

CHAPTER 2

LITERATURE SURVEY

The use of robots in the medical field started by adapting industrial robots to surgical applications (Kwoh et al., 1988; Cinquin et al., 1992). These industrial robots were used after some modifications to guarantee the surgical requirements such as safey and sterility. Firstly in 1985, Kwoh et al. (1988) used a PUMA 560 industrial robot to locate a neurosurgical tool next to the head of the patient. Organizational scheme of this system is depicted in Figure 2.1. Recently robots began to take place in surgical rooms as assistive devices for the surgeons (Kuo and Dai, 2009). However, industrial robots and surgical robots differ from each other in their priorities. Tanigucci (2010) states that an industrial robot requires “high power" and "high speed" while a surgical robot requires "safety" and "cleanness".

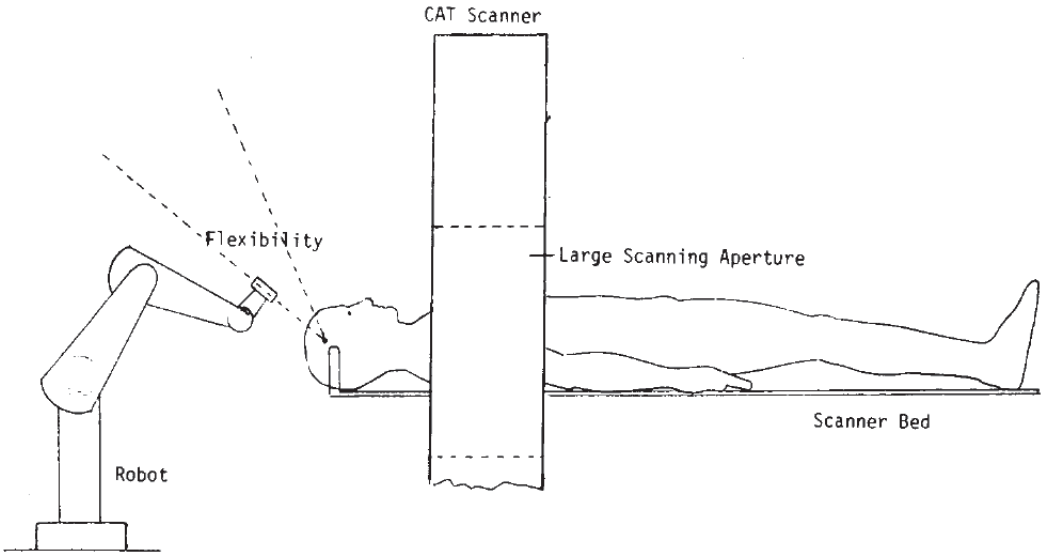

Figure 2.1. Organization of surgery field with PUMA 560
(Source: Kwoh et al., 1988)

Due to the specific requirements of surgical applications, more specialized systems were needed over time (Taylor et al., 2008). Surgical robots are usually used in minimally invasive surgery applications. Minimally invasive surgery (MIS) is performed with surgical tools inserted through a small hole (incision port) into the patient’s body.

Surgeons and patients prefer it since these operations can be completed in less time with less pain, less blood loss and lower risk of infection. The post-operative process also results in faster recovery and smaller surgical scars (Li et al., 2015). MIS has a wide range of use in specific fields of surgery such as endoscopy, laparoscopic surgery, keyhole surgery, and microsurgery (Kuo and Dai, 2009). "Probot" is the first robot assisted device, which is developed in Imperial College London to be clinically used in a minimal invasive prostate surgery in 1991 (Kuo and Dai, 2009) (Figure 2.2). After Probot, robotically assisted MIS applications rapidly developed and gained a worldwide reputation. For example, the "da Vinci" surgical system developed by Intuitive Surgical Inc. (Figure 2.3) has been globally accepted by many surgeons and patients. Among commercial MIS robots, the FDA (U.S. Food and Drug Administration) approved da Vinci surgical robotic system is probably the most well known and successful one (Guthard and Salisbury, 2000). Lie et al. (2015) noted that more than 3000 da Vinci robots are in operation all over the world. Today, Intuitive Surgical Inc. (2018) states that every 60 seconds, a surgeon somewhere in the world uses a da Vinci Surgical System for a MIS application.

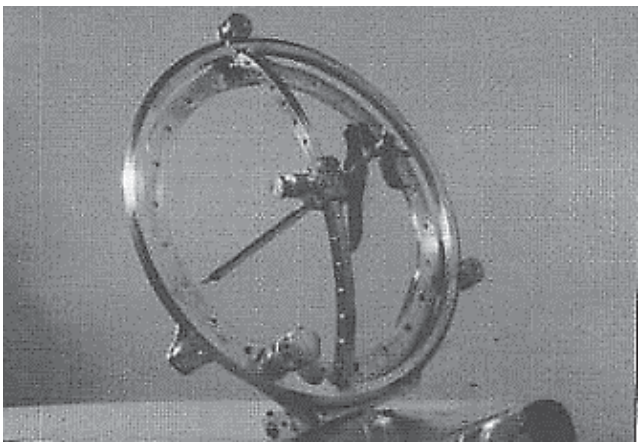

Figure 2.2. Probot System
(Source: Davies et al., 1996)

In robotically assisted MIS applications, assistive devices are generally used to hold or guide an endoscope, which is a slender camera to display inside the patient's body. During a surgery, providing surgeon with a clear view of the surgery area inside the body is crucial. To realize that, various endoscope holders were developed. Some of these systems are just simple mechanical holders while others being motorized.

Figure 2.3. The da Vinci System
(Source: Intuitive Surgical Inc., 2018)

Mechanical holders are used by adjusting a passive arm to locate the endoscope in a desired position, where the mechanism is locked. “Robotrac” and “Aesculap” can be given as examples of these mechanical holders (Bihlmaier, 2016). Also, various motorized endoscope holding systems are developed for the surgeries where endoscopes are used as imaging devices. Taniguchi et al. (2010) states that 27 endoscope robots had been developed between 1994-2009 and 8 of them had been used on humans while others had been used on animals or stayed as a model. In most of these systems, endoscope is positioned with a robotic arm and surgeon controls this robotic arm with different tools or ways such as using a controller, giving voice commands, making head movements or using an image processing system tracking the surgical tools in the surgeon’s hand. Bihlmaier (2016) explains the main examples of the motorized endoscope holding robots in literature in a chronological order of development. According to that study, a comparison chart was prepared to compare different endoscope holder systems (Table 2.1). As a result, most of them are designed for laparoscopic surgery applications and have serial structures with various dof’s.

Table 2.1 Comparison chart for MIS robots

System	DOF_{total}	DOF_{active}	Kinematic Structure	Field of Application
SMART/P-Arm	6	4	Hybrid	Laparoscopy
Naviot	5	2	Hybrid	Laparoscopy
Lapman	6	3	Hybrid	Gynecology
AESOP	6	4	Serial	Laparoscopy
EndoAssist	3 + gooseneck	3	Serial	Laparoscopy
ENDEX	7	1	Serial	Gynecology
CRS A-460	6	6	Serial	Laparoscopy
HISAR	7	5	Serial	Laparoscopy
LARS	5	4	Serial	Laparoscopy
SoloAssist	5	2	Serial	Gynecology, Urology
IBIS IV	4	4	Serial	Laparoscopy
FIPS ENDOARM	6	3	Serial	Laparoscopy
NeuroArm	7	6	Serial	Neurosurgery

2.1. Kinematic Design Considerations for MIS Robots

The kinematic design stage is one of the most important stages in designing a MIS robot since it predetermines some crucial MIS concerns such as safety, accuracy, dexterity and ergonomics. Therefore, kinematic design considerations such as pivoting motion, decoupled motion, backdrivability, redundancy, workspace and isotropy should be taken into account to fulfil specific surgical requirements (Kuo et al., 2012).

Pivoting motion is required due to the necessity of moving a tool or camera through an incision port in MIS. This requirement can be satisfied in two different ways: by using a mechanical RCM or a non-mechanical RCM. The first way is to force the surgical tool mechanically to move around a center of motion that is outside the robot. RCM is a point where one or more rotational and translational movements are pivoted outside the mechanism. This concept allows MIS robots to work in a large workspace outside the body of the patient while providing the desired pivoting movements to the surgical tool. In addition, as it moves, the robot's control, patient and surgeon are automatically protected against damages from any possible control or coordination error

(Kuo and Dai, 2009). In robotic MIS systems, mechanical RCMs can be obtained by using several concepts: iso-centers, circular tracking arcs, parallelograms, synchronous belt transmissions, spherical linkages, parallel mechanisms and gear trains (Kuo et al., 2012). In Table 2.2, different RCM concepts and their applications to MIS robots are presented.

The second way is to use non-mechanical RCM concept. In non-mechanical RCMs, the desired pivoted motion can be obtained by the control of a redundant robot. In this concept, end-effector of the robot is virtually pivoted at a predefined pivot point. However, Liu et al. (2016) state that compared to non-mechanical ones, mechanical RCMs are more reliable and considered more suitable for clinical practice.

In MIS, a surgical tool may have up to 4-dof through the incision port: pitch, yaw, roll and heave motions (Liu et al., 2016). In Figure 2.4, ${}^{P}\theta_x$, ${}^{P}\theta_y$, ${}^{E}\theta_w$ and ${}^{E}d_w$ represent pitch, yaw, roll and heave motions, respectively where P(x, y, z) is a reference frame attached to the pivoting point and E(u, v, w) is a reference frame attached to the surgical tool (Kuo et al., 2012).

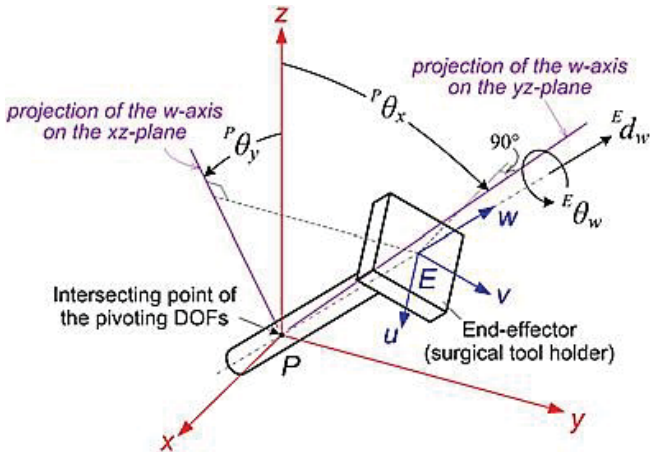

Figure 2.4 4-dof motion of a MIS tool
(Source: Kuo et al., 2012)

However, for endoscope holding robots, Taniguchi et al. (2010) state that pitch, yaw and heave movements are sufficient for endoscope movements. These three motions define a 2R1T motion pattern where the translation direction is perpendicular to the plane defined by the orthogonally intersecting rotation axes. The intersection point of the rotation axes is the pivot point.

Various parallel manipulators with 1T2R-type platform motion, which is the kinematic inversion of 2R1T-type, also can be seen in many applications such as contour

Table 2.2. RCM mechanisms and their applications to MIS robots (Source: Kuo et al., 2012)

RCM type	*Kinematic structure sketch*	*Sampled MIS Robot*
Isocenter	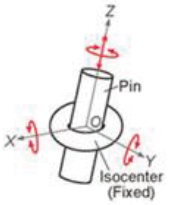	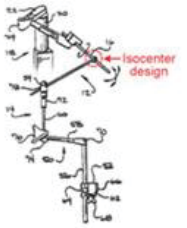
Circular tracking arc	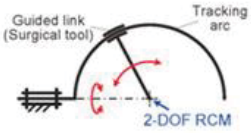	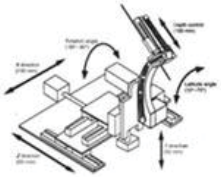
Parallelogram	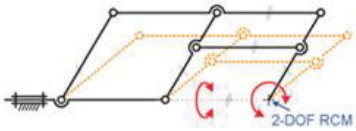	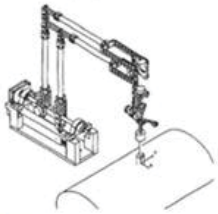
Belt	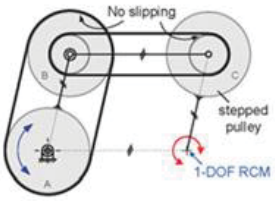	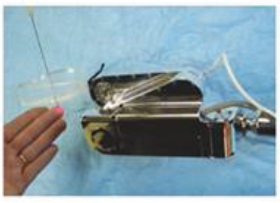
Spherical linkage	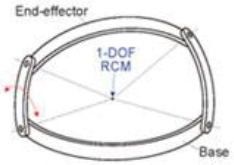	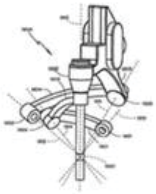
Gimbal	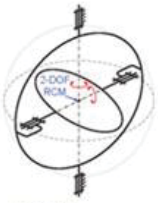	
Parallel wrist mechanism	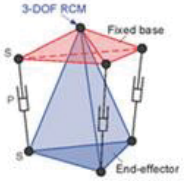	
Gear train	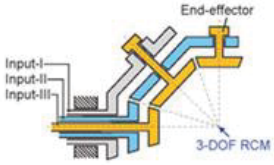	

machining, material handling, automated assembling, telescopes, antennas, guns and solar panels (Gogu, 2012).

2.2. Literature Survey for 2R1T Mechanisms

In this section, patents and scientific studies on the manipulators, with 2R1T motion are presented. Some serial manipulators are issued in the patents US7395607, US9510911, US2017035518 and WO2017114860A1. In the patents FR2974322 and DE102010018802, some hybrid structures comprising a P joint serially connected to a 2-dof spherical mechanism are presented. This type of mechanisms can be also found in scientific publications (Lum et al., 2009). In the patents US5397323, US6441577 and US2006196299, the second R motion of the 2R1T motion is obtained by a parallel mechanism while other motions are obtained via serial chains connected to the parallel mechanism. So, these manipulators have a serial-parallel-serial ordered hybrid kinematic structure. Some scientific publications are also available for this type of kinematic structures (Madhani et al., 1998; Kim et al., 2010).

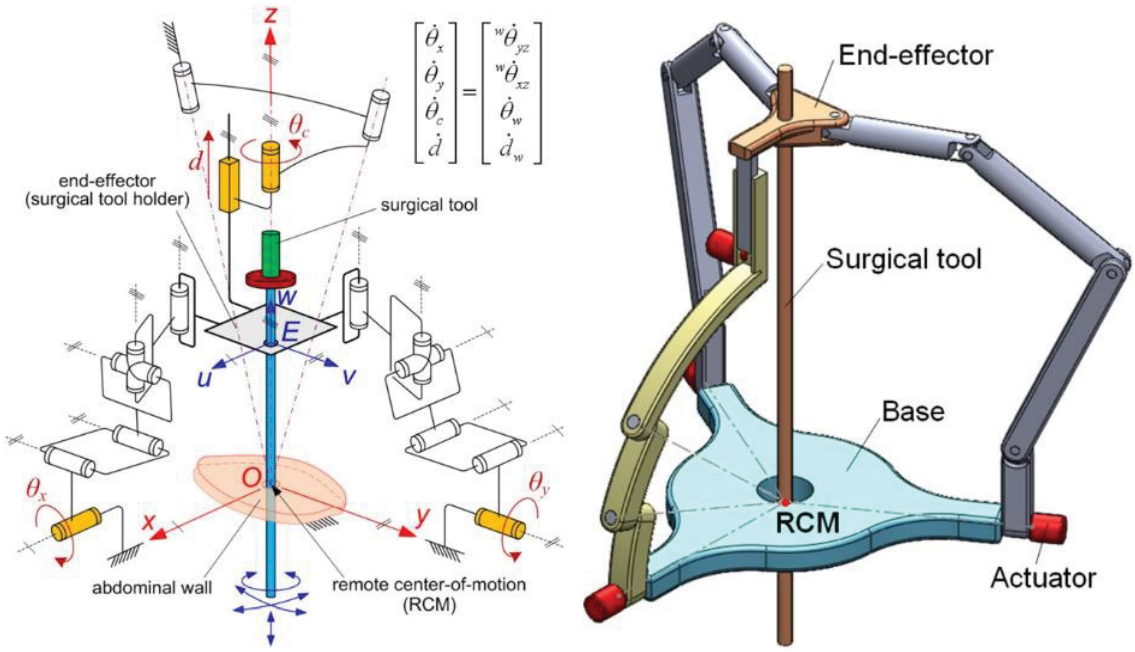

Figure 2.5. The kinematic diagram (left) and the CAD model (right) of a fully decoupled 4-DOF parallel manipulator (Source: Kuo and Dai, 2012)

Even though any patent could not be found on fully parallel kinematic structures whose end-effector has 2R1T motion with an RCM, some scientific publications are encountered. Kuo and Dai (2012) presented 3-legged RCM parallel manipulator. In

Figure 2.5, the axes of all revolute joints in the spherical leg intersect each other at an RCM and this leg is connected to the platform with a prismatic joint. Also, two links of the side legs move on a plane due to the three parallel revolute joint axes.

Li et al. (2013) presented two manipulators with 2R1T motion and an RCM. As can be seen in Figure 2.6, three legs seem to be identical for each manipulator. For both manipulators, legs move on a plane, which can be rotated around a revolute joint axis passing through the RCM. However, except the figure, no information about the kinematic structure is given in (Li et al., 2013).

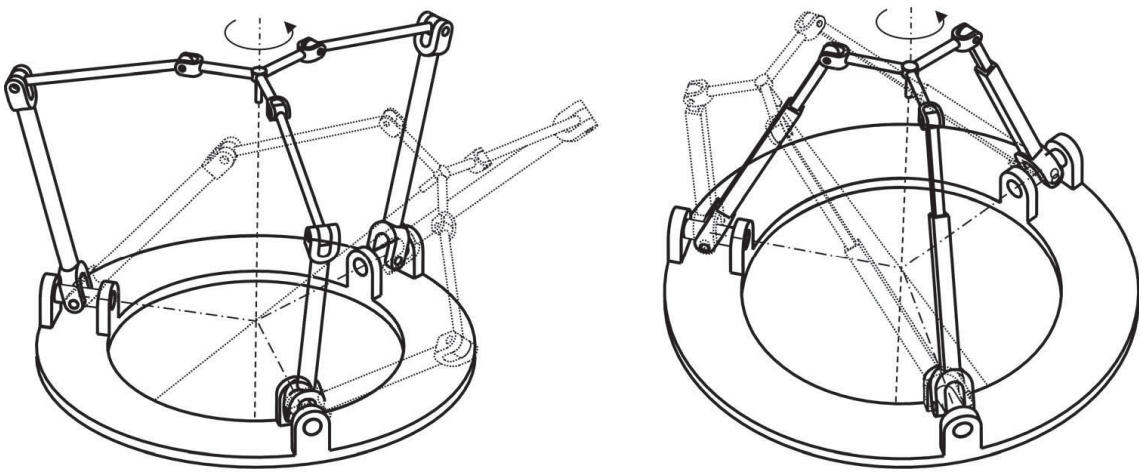

Figure 2.6. 2R1T RCM mechanisms
(Source: Li et al., 2013)

Recently, Zhang et al. (2018) presented a 2R1T RCM mechanism with 2CRRR-CRR kinematic structure. In Figure 2.7, the cylindrical joint axes of the three legs intersect at the RCM. Also, each leg moves on a plane, which can be rotated about the cylindrical joint axes. These last mechanism examples comprise radial symmetrically distributed legs, which is not a suitable solution for a transnasal MIS.

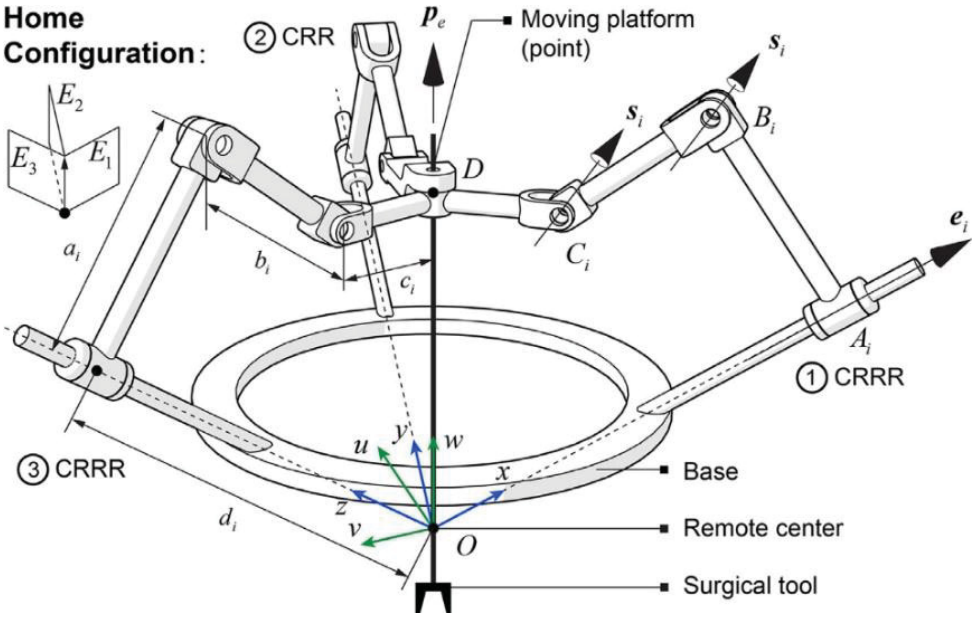

Figure 2.7. 2CRRR-CRR kinematic structure
(Source: Zhang et al., 2018)

CHAPTER 3

STRUCTURAL SYNTHESIS[1]

In this Chapter, it is aimed to perform the structural synthesis for non-parasitic 3-dof parallel manipulators (PM) with 2R1T motion pattern. Non-parasitic motions refer to the motions of the end-effector of a manipulator which can be decomposed into the translations along or rotations about Cartesian axes with number of independent motions being equal to the manipulator's dof and without any extra undesired motions along or about other axes. An example for a PM with parasitic motion is a 3-RRS PM issued by Tetik (2016). The mobile platform of a 3-RRS PM can translate in all directions and rotate about two axes, but the PM has 3-dof. Two of the translational dofs of this PM are parasitic. Such parasitic motions are undesired in RCM applications.

Various kinematic manipulator architectures can provide a non-parasitic 2R1T motion. RRP serial manipulator has the simplest possible kinematic structure. In the RRP structure, the R joint axes orthogonally intersect each other and the P joint direction is perpendicular to the plane defined by the R joint axes.

Hybrid kinematic structure types generating 2R1T motion can be listed as:

Type 1: The first R of the 2R1T motion is serially connected to a 2-dof parallel kinematic chain (PKC) for the RT motion.

Type 2: 2R motion is obtained with a PKC while the T motion is connected serially.

Type 3: Second R motion is obtained with a PKC while the first R and the T motion are serially connected.

Li and Hervé (2010) used group theory for the classification of PMs with non-parasitic 1T2R motion, which is the kinematic inversion of 2R1T motion. The results presented in this Chapter are comparable with Li and Hervé's (2010) results. In this thesis, Kong and Gosselin's (2007) type synthesis method is followed for the classification of PMs with non-parasitic 2R1T motion. The method is based on virtual chain concept and uses screw theory. Section 3.1 defines the virtual chain concept. Section 3.2 presents the procedure of type synthesis method for RRP PMs. In Section 3.3, the decomposition of the wrench systems of RRP PKCs is discussed. Section 3.4 deals with the type synthesis of the legs. The assemblies of the legs that generate the virtual chain are presented in

[1] The content of this chapter were previously published by Yaşır and Kiper (2017).

Section 3.5. Finally, evaluation of these PM assemblies together with the serial and hybrid architectures according to some design criteria are presented in Section 3.6.

3.1. Wrench System of an RRP Parallel Kinematic Chain

Kong and Gosselin (2007) describe a virtual chain as a kinematic chain connecting the fixed base of a PM to the moving platform which has a prescribed motion pattern. This kinematic chain can be serial or parallel and is not unique for one prescribed motion pattern. However, the simplest one is generally preferred. The simplest virtual chain (VC) corresponding to the 2R1T motion pattern is a serial RRP chain. In screw theory, the motions of a kinematic chain are represented by twist systems while constraints of a kinematic chain are represented by wrench systems (Kong and Gosselin, 2007). The wrench system of the motion of an RRP= PKC is a 2 F_0-1 F_∞ system (Figure 3.1.a), where F_0 and F_∞ correspond to 0-pitch and ∞-pitch wrenches, respectively. Henceforth, the VC joints are represented with bold letters (*i.e.* **RRP**) to distinguish them from the actual joints of the PM.

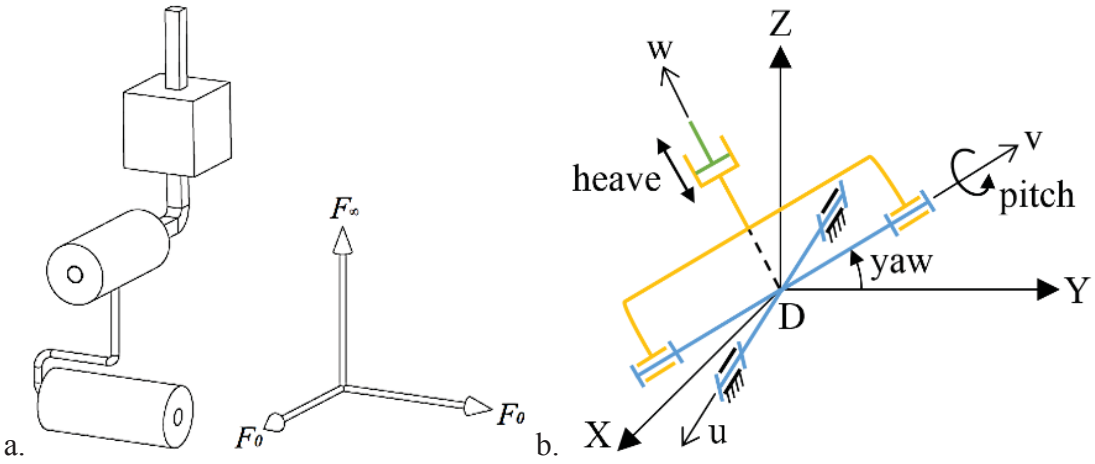

Figure 3.1. a. 2-F_0-1 F_∞ system b. Description of the **RRP** VC

In Figure 3.1.b, an illustrative scheme for an **RRP** VC is given. The R joint axes of the VC are represented by u- and v- axes. They are associated with yaw and pitch motions, respectively. In addition, they intersect at point D, which is the pivot point. w-axis which is along the direction of the P joint also passes through this pivot point. The

u-axis is defined with the following two conditions: it passes through the pivot point and it is perpendicular to the w-axis. Therefore, the u-axes attached to different legs do not have to be in the same direction. In Figure 3.1.b, when yaw and pitch angles are equal to zero, the uv-plane coincides with the XY-plane and the w-axis is coincident with the Z-axis of the XYZ frame, which is attached to the base.

3.2. Procedure for the Type Synthesis of RRP Parallel Manipulators

The type synthesis of RRP= Parallel Manipulators are performed in four steps:

Step 1: Decomposition of wrench systems of RRP= PKCs

Step 2: Type synthesis of legs for RRP= PKCs

Step 3: Assembly of legs to generate RRP= PKCs

Step 4: Evaluation of the RRP= PKCs generated in Step 3

Each of these steps are respectively discussed in detail in the following sections and an optimal structure is selected at the end of the Chapter.

3.3. Step 1: Decomposition of the Wrench System

The leg constraint degrees for PKCs can be found using the following equation:

$$c^1 + c^2 + \ldots + c^m = M + \Delta \tag{3.1}$$

where c^i denotes the degrees of leg constraint, m denotes the number of legs, M denotes the dof of PKC and Δ denotes the total degree of overconstraint of the PKC. Combinations of leg constraint degrees for 3-legged 3-dof PKCs are listed in Table 3.1.

Table 3.1. Combinations of c^i for 3-legged 3-dof PKCs

Δ	**6**	**5**	**4**		**3**			**2**			**1**			**0**		
c^1	3	3	3	3	3	3	2	3	3	2	3	2	2	3	2	1
c^2	3	3	3	2	3	2	2	2	1	2	1	2	1	0	1	1
c^3	3	2	1	2	0	1	2	0	1	1	0	0	1	0	0	1

As mentioned above, the wrench system of the moving platform in this study is a 2 F_0-1 F_∞-system. This means that the legs may have one of the following sub-systems: 2 F_0-1 F_∞-, 1 F_0-1 F_∞-, 2 F_0-, 1 F_0-, 1 F_∞- or 0-system. The wrench system of the moving platform can be found by linearly combining the leg-wrench systems (Kong and Gosselin, 2007). After combining the leg-wrench systems, the ones that do not have two F_0- and one F_∞-system in total will not produce the wrench system of the platform. So, these combinations are disregarded. Feasible and disregarded combinations are listed in Table 3.2 and Table 3.3, respectively.

Table 3.2. Combinations of leg-wrench systems for 3-legged **RRP**= PKCs

Δ	**6**	**5**	**4**					**3**							**2**				
$\mathbf{c^1,c^2,c^3}$	3,3,3	3,3,2	3,3,1		3,2,2			3,3,0		3,2,1			2,2,2		3,2,0		3,1,1		
2 F_0-1 F_∞	3	2	2	2	2	1	1	1	2	1	1	1	1	0	0	0	1	1	1	1	1
1 F_0-1 F_∞	0	1	0	0	0	2	0	1	0	1	1	0	0	3	2	1	1	0	0	0	0
2 F_0	0	0	1	0	0	0	2	1	0	0	0	1	1	0	1	2	0	1	0	0	0
1 F_0	0	0	0	1	0	0	0	0	0	1	0	0	1	0	0	0	0	0	2	0	1
1 F_∞	0	0	0	0	1	0	0	0	0	0	1	1	0	0	0	0	0	0	0	2	1
0	0	0	0	0	0	0	0	0	1	0	0	0	0	0	0	0	1	1	0	0	0

Δ	**2**					**1**								**0**					
$\mathbf{c^1,c^2,c^3}$	2,2,1					3,1,0		2,2,0		2,1,1				3,0,0	2,1,0			1,1,1	
2 F_0-1 F_∞	0	0	0	0	0	1	1	0	0	0	0	0	0	1	0	0	0	0	0
1 F_0-1 F_∞	2	0	2	1	1	0	0	2	1	1	0	1	0	0	1	1	0	0	0
2 F_0	0	2	0	1	1	0	0	0	1	0	1	0	1	0	0	0	1	0	0
1 F_0	1	0	0	1	0	1	0	0	0	2	0	1	1	0	1	0	0	2	1
1 F_∞	0	1	1	0	1	0	1	0	0	0	2	1	1	0	0	1	1	1	2

Table 3.3. Disregarded combinations of leg-wrench systems for 3-legged **RRP**= PKCs

Δ	**3**	**2**	**1**		**0**		
c^1, c^2, c^3	2,2,2	2,2,1	2,2,0	2,1,1	2,1,0	1,1,1	
2-F_0-1-F_∞	0	0	0	0	0	0	0
1-F_0-1-F_∞	0	0	0	0	0	0	0
2-F_0	3	2	2	1	1	0	0
1-F_0	0	1	0	2	1	3	0
1-F_∞	0	0	0	0	0	0	3
0	0	0	1	0	1	0	0

3.4. Step 2: Type Synthesis of Legs

A single loop kinematic chain (SLKC) can be considered as a serial chain whose end-links are connected to each other (Kong and Gosselin, 2007). Let f and c denote the

total dof of all joints and order of the wrench system of this serial chain, respectively. So, the number of the joints in this SLKC can be found as follows:

$$f = (6 - c) + M \tag{3.2}$$

3.4.1. 2 F_0-1 F_∞-system

In a 2 F_0-1 F_∞-system, using (3.2) for c = 3 and M = 3, number of the joints in a virtual loop (VL) including the VC should be equal to 6. Since three of the joints already belong to the **RRP** VC, there should be three remaining joints on the leg. For obtaining a 2 F_0-1 F_∞-system, two coaxial 3 F_0-2 F_∞-systems and one codirectional 2 F_0-3 F_∞-system compositional units (CU) are needed to be combined (see Table 3.3 in (Kong and Gosselin, 2007)). Coaxial or codirectional CUs are denoted by $(\ )_L$. Inside the parenthesis, R or P joints can be written, for instance such as $(RPR)_L$. A coaxial CU is composed of one or more R joints with coincident axes, whereas a codirectional CU is composed of one or more P joints with parallel directions. When we consider the **RRP** VC (or can be written as $(\mathbf{R})_L(\mathbf{R})_L(\mathbf{P})_L$ VC), no feasible solutions can be found for a VL since the leg would have multiple coaxial R joints or codirectional P joints. However, the VC itself (**RRP** VC) can be used as a leg. So, leg structure alternatives are $(R)_L(R)_L(P)_L$ where two R joints constitute a U (Figure 3.2) and $(R)_L(RR)_A$, where $(\ )_A$ represents a parallel axis CU – a CU with parallel R joint axes.

3.4.2. 1 F_0-1 F_∞-system

This system can be obtained by combining a coaxial CU and a planar CU which is denoted by $(\ )_E$. There are seven joints in the VL and four of them are on the leg. A planar CU can be formed with at least two joints, where at least one of them is an R joint. All R joint axes of a planar CU are parallel to each other. Having more than two P joints or more than one coaxial R joints in the leg is not allowed because, it results in an internal mobility in the leg. The coaxial unit needs to be a part of the VC, because the R axes in the VC are perpendicular to each other. In addition, some part of the coaxial unit has to be in the remaining part of the loop as well, otherwise, an internal mobility occurs due to

having a coplanar 4-joint leg. For example, a coplanar 4R chain in a leg constitutes a 4-bar mechanism, which results in an extra 1-dof. Thus, there is only one possible structure as $((R\mathbf{R})_L\mathbf{RP}E)_E$, where E denotes a planar joint. When the construction of an E joint is

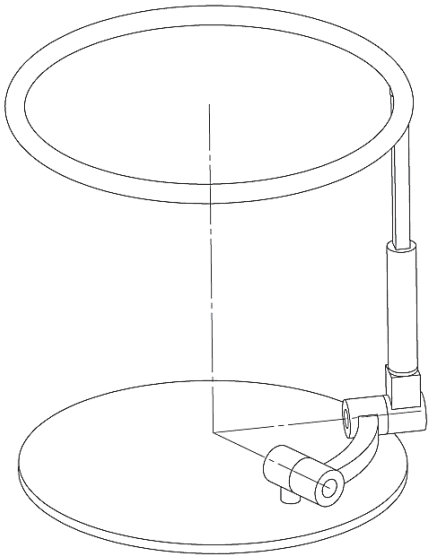

Figure 3.2. 2 F_0-1 F_∞ system leg structure: UP

considered, there may be a bunch of alternatives: planar RRR, PRR, RPR, RRP, PPR, PRP or RPP chain. Considering ease of construction and operation, it is better to minimize the number of the unactuated P joints in a mechanism. So, the solutions with multiple P joints are disregarded. The feasible alternatives are $((R)_LRRR)_E$, $((R)_LRRP)_E$, $((R)_LRPR)_E$ and $((R)_LPRR)_E$. The first three legs correspond to URR, URP and UPR legs, respectively. For the last alternative, if the P direction is along the $(R)_L$ axis, this specific case constitutes a CRR chain. Note that $(R)_L$ is written inside the parenthesis $(\ )_E$ since it can be positioned anywhere inside the planar chain part of the leg. Lastly, UPR leg is illustrated in Figure 3.3 as an example for a 1 F_0-1 F_∞-system leg structure.

3.4.3. 2 F_0-system

A 2 F_0-system is composed of a spherical CU which is represented by $(\ )_S$ and a codirectional CU. There are four joints in the VL excluding the VC. The rule for a spherical CU is having at least two R joints with intersecting axes. A codirectional CU

needs to have at least one P joint. Practically, two or more codirectional P joints are not suitable within the leg. Hence, the only structure is $(SRR)_S(PP)_L$, where S corresponds to a spherical joint. By excluding VC, it can be seen that the leg has an SP structure.

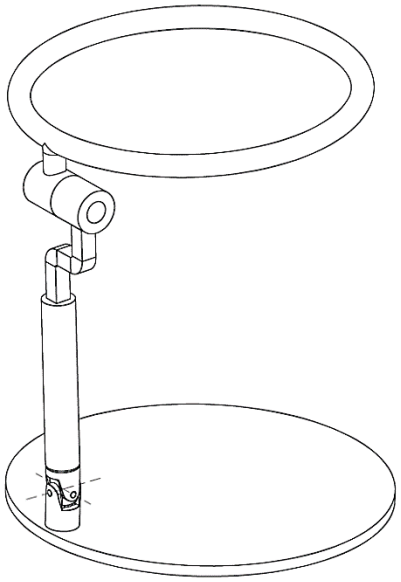

Figure 3.3. 1 F_0-1 F_∞-system leg structure alternative: UPR

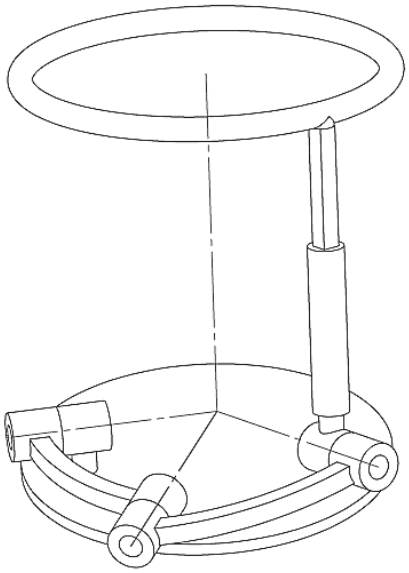

Figure 3.4. 2 F_0-system leg structure: SP

A practical alternative can be $(RRR)_S(P)_L$ leg for this structure and it is depicted in Figure 3.4.As can be seen, all the revolute joint axes intersect each other and the direction of P joint in the leg is parallel to the direction of the P joint in VC.

3.4.4. 1 F_0-system

There must be eight joints in the VL of this wrench system. In Table 3.4 in (Kong and Gosselin, 2007), six different ways to obtain a 1 F_0 system are given as:

a) composing a planar CU and a spherical CU,
b) two spherical CUs with distinct centers
c) inserting two coaxial CUs into a SLKC composed of a planar CU
d) inserting two coaxial CUs into a SLKC composed of a spherical CU
e) inserting a coaxial and a codirectional CU into a SLKC composed of a spherical CU
f) inserting two codirectional CUs into a SLKC composed of a spherical CU

Case a: This case is achieved in two forms: $(RR\mathbf{R})_S(\mathbf{RP}E)_E$ and $(RRR\mathbf{R})_S(\mathbf{RP}\,.\,.\,)_E$ where each dot corresponds to an R or P joint. So, leg structures can be in the form of UE and $S(\,.\,.\,)_E$, respectively. The centers of the U and S joint should be on the u-axis and the plane of the U joint should not be parallel to the u-axis. Planes of the E joint and $(\,.\,.\,)_E$ should be perpendicular to the v-axis. As an example, UE leg is demonstrated in Figure 3.5.a.

Cases b and d: The VC is not compatible with a SLKC composed of a spherical CU not including any codirectional CU since it has a P joint inside. So, these cases are not feasible.

Case c: The only possible structure of the VL is $((R)_L(R\mathbf{R})_L\mathbf{RP}E)_E$ because other structure options result in either more than one coaxial R's or coplanar 4-joint subchains in the loop. So, leg structure is $((R)_L(R)_LE)_E$. Conditions for this structure are as follows:

- the axis of the first $(R)_L$ is along the u-axis
- the axis of the second $(R)_L$ is along the virtual **P** direction
- plane of the E joint should be perpendicular to the v-axis
- $(R)_L$'s can be distributed in the E joint, *i.e.* $((R)_LE(R)_L)_E$

$((R)_LE(R)_L)_E$ structure is illustrated as a $((R)_LRPR(R)_L)_E$ leg where the first two R joints are illustrated as an U joint in Figure 3.5.b.

Case e: The possible structures for the VL are $(RRR\mathbf{RR})_S(\mathbf{P}P)_L(R)_L$ and $((R\mathbf{R})_L\mathbf{R}(\mathbf{P}P)_LRRR)_S$. Thus, the first leg structure can be $S(R)_L(P)_L$ which is demonstrated in Figure 3.5.c. The conditions for this structure are as follows:

- center of the S joint is on the pivot point
- the axis of the $(R)_L$ does not pass through the pivot point
- direction of $(P)_L$ is along the w-axis

Likewise, the second structure can be $((R)_LS(P)_L)_S$, where the conditions are as follows:

- the axis of $(R)_L$ is along the u-axis,
- the center of the S joint is on the v-axis
- direction of $(P)_L$ is along the w-axis

Case f: For this case, two possibilities are available: $(S\mathbf{RR}(\mathbf{P}P)_L(P)_L)_S$ or $(RRR(P)_L(P)_L)_S$ and $(SR\mathbf{RR}(\mathbf{P})_L(P)_L)_S$ or $(SR(P)_L)_S$. The first option is not preferable due to two P joints in the leg while the second one is not feasible because of its internal mobility in the spherical 4R in the leg.

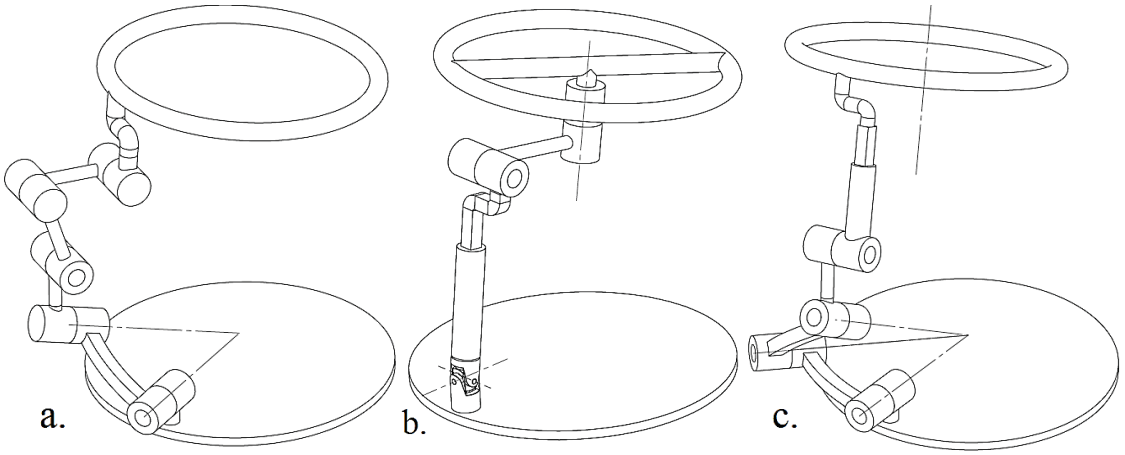

Figure 3.5. 1-F_0 system leg structures: a. UE leg b. $((R)_LRPR(R)_L)_E$ leg c. $S(R)_L(P)_L$

3.4.5. 1 F_∞-system

In such a system, there must be eight joints in the VL. So, there are five joints without VC. According to (Kong and Gosselin, 2007), the following options can be used for obtaining this wrench system:

a) combining two parallel axis CUs or planar CUs

b) inserting a coaxial CU into the SLKC composed of a parallel axis CU or planar CU

Case a: In practice, a planar CU is more desirable than a parallel axis CU in the aspects of ease of construction. So, only planar CUs are considered here for the synthesis. Possible VLs with two planar CUs are (. . **R**)$_E$(**RP** . . .)$_E$ and (. . . **R**)$_E$(**RP** . .)$_E$. So the leg structure is (. .)$_E$E or E(. .)$_E$ where . . may be RR, RP or PR. In Figure 3.6, (RR)$_E$(RRR)$_E$ structure is demonstrated as an example. The conditions for these structures are as follows:

- plane of the first ( )$_E$ is perpendicular to the u-axis
- plane of the second ( )$_E$ is perpendicular to the v-axis

Case b: Possible structures for the VL are in the form of ((R**R**)$_L$**RP** . . . .)$_A$. So the leg can be ((R)$_L$RRRP)$_A$, ((R)$_L$RRPR)$_A$, ((R)$_L$RPRR)$_A$ or ((R)$_L$PRRR)$_A$ where the conditions are:

- (R)$_L$ is coaxial with the u-axis
- the remaining R joint axes are all parallel to the v-axis

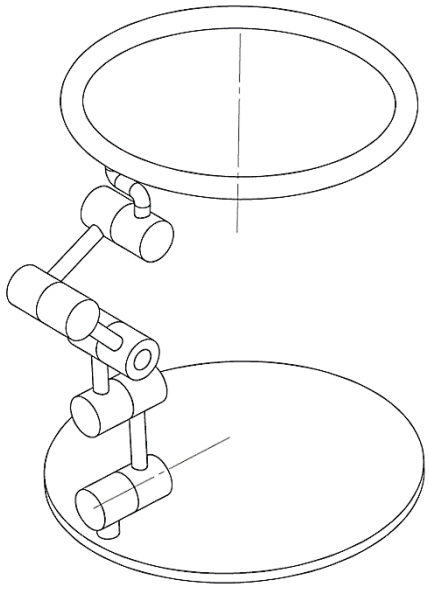

Figure 3.6. 1-F$_\infty$ system leg structure alternative: (RR)$_E$(RRR)$_E$

3.4.6. 0-system

In this system, the leg has no constraints, *i.e.* c = 0. Therefore, there are six joints in the VL and any 6-dof chain can be selected as a leg. UPS can be an example for this system (Figure 3.7).

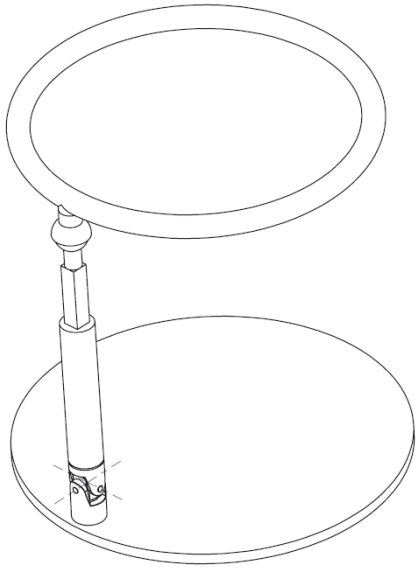

Figure 3.7. 0-system leg structure alternative: UPS

Type synthesis of the legs for 2 F_0-1 F_∞-system and its all subsystems are performed and the results are summarized in Table 3.4.

3.5. Step 3: Assembly of the Legs

After enumerating all possible leg configurations in the Section 3.4, the legs are assembled in this Section according to combinations of leg-wrench systems given in Table 3.2. **RRP**= PKCs can be generated by assembling three of the alternative leg structures given in Table 3.4. For each of the six alternative leg-wrench systems in Table 3.4, a representative leg is selected and listed in Table 3.5.

In assembling representative legs, two or three legs of UP, which has a 2 F_0-1 F_∞ type leg-wrench system, cannot be used in the PKC since the centers of the universal (U) joints of multiple legs would necessarily be at the pivot point, hence resulting in a hybrid mechanism. Therefore the columns in Table 3.2 with more than one 2 F_0-1 F_∞-system are

Table 3.4. Leg alternatives for each leg-system

System	Leg Structure Alternatives
2 F_0-1 F_∞	$(R)_L(R)_L(P)_L$
1 F_0-1 F_∞	$(R)_L$E ($(R)_L$ is co-axial with 1st R joint axis of the VC): $((R)_LRRR)_E$ or URR; $((R)_LPRR)_E$ (may be CRR); $((R)_LRPR)_E$ or UPR; $((R)_LRRP)_E$ or URP
2 F_0	SP (The center of S joint should be coincident with the pivot point D)
1 F_0	a) UE (center of U joint is on u-axis; plane of U joint is not parallel to u-axis; plane of E joint is perpendicular to v-axis): $S(RR)_E$, $S(RP)_E$, $S(PR)_E$, $U(PRR)_E$; $S(\ .\ .\ )_E$ (center of S joint is on u-axis; plane of $(\ )_E$ joint is perpendicular to v-axis): $S(RR)_E$, $S(RP)_E$ c) $((R)_L(R)_LE)_E$ (axis of 1st $(R)_L$ is along u-axis; axis of 2nd $(R)_L$ is parallel to w-axis; plane of joint E is perpendicular to v-axis; $(R)_L$'s can be distributed in E joint) e) $S(R)_L(P)_L$ (center of S joint is on pivot point; axis of $(R)_L$ does not pass through pivot point; direction of $(P)_L$ is along w-axis) or $((R)_LS(P)_L)_S$ (axis of $(R)_L$ is along u-axis; center of S joint is on v-axis; direction of $(P)_L$ is along w-axis)
1 F_∞	1) $(\ .\ .\ )_E$E (plane of $(\ )_E$ is perpendicular to u-axis; plane of E joint is perpendicular to v-axis): $(RR)_E(RRR)_E$, $(RR)_E(RRP)_E$, $(RR)_E(RPR)_E$, $(RR)_E(PRR)_E$; $(RP)_E(RRR)_E$; $(PR)_E(RRR)_E$; $E(RR)_E$: $(RRR)_E(RR)_E$, $(RRP)_E(RR)_E$, $(RPR)_E(RR)_E$, $(PRR)_E(RR)_E$; $(RRR)_E(RP)_E$; $(RRR)_E(PR)_E$ 2) $((R)_LRRRP)_A$, $((R)_LRRPR)_A$, $((R)_LRPRR)_A$, $((R)_LPRRR)_A$
0	Example: UPS

Table 3.5. Representative leg structures for each leg-system

System	Representative Legs
2 F_0-1 F_∞	$(R)_L(R)_L(P)_L$ or UP
1 F_0-1 F_∞	$((R)_LRPR)_E$ or UPR
2 F_0	$(RRR)_SP$ or SP
1 F_0	$((R)_LRPR(R)_L)_E$ or UPRR
1 F_∞	$(RR)_E(RRR)_E$
0	UPS

disregarded. Also, some of the assemblies result in 4-dof platform motion due to dependency of the leg wrench systems. So they are disregarded as well. For example using more than one UPR leg in an assembly results in either an extra translational dof for the moving platform (except using two UPR leg with a UE leg which is a 1-F_0 system leg) or having bifurcated and non 2R1T motion platform (Li et al., 2012). So the columns in Table 3.2 with more than one 1 F_0-1 F_∞-system leg (except the column with two 1 F_0-1 F_∞- and one 1 F_0-system legs) are disregarded. Lastly, the columns consisting of same type of leg-wrench systems except 0-system is more desirable over the ones with 0-systems. To illustrate, the column having two 1 F_0-1 F_∞-system and one 1 F_0-system is more preferable than the one having one 1 F_0-1 F_∞-, one 1 F_0- and one 0-system. So, only the preferable ones are taken into evaluation.

According to Table 3.2, possible assemblies are constructed in a CAD program. Even though some of the assemblies have the 2R1T platform motion, they were not suitable to be constructed as an RCM mechanism and they are disregarded too. As a result, selected structures are 1 (2 F_0-1 F_∞-system) 1(1 F_0-1 F_∞-system) 1 (1 F_∞-system), 1 (2 F_0-1 F_∞-system) 2 (1 F_∞-system), 2 (1 F_0-1 F_∞-system) 1 (1 F_0-system), 1 (1 F_0-1 F_∞-system) 2 (1 F_0-system), 2 (1 F_0-system) 1 (1 F_∞-system) and they are listed in Figure 3.8 as a, b, c, d and e, respectively.

3.6. Step 4: Evaluation of Assemblies

For the assemblies that satisfy both the 2R1T motion and the RCM concept, the options for the three joints to be actuated are evaluated. Preferably, the actuated joints should be connected to the base. Also for some of the assemblies obtained in Section 3.5 the legs share the first R axes on the base, hence they actually have a hybrid type 1 kinematic structure. All the manipulators obtained in Section 3.5 are evaluated along with hybrid types 2 and 3 and serial assemblies. All alternatives are compared with each other considering the following evaluation criteria:

- Ease of dynamic balancing
- Number of links
- Structural symmetry
- Decoupling of the inputs and the output 2R1T motion
- Number of actuators connected to the base

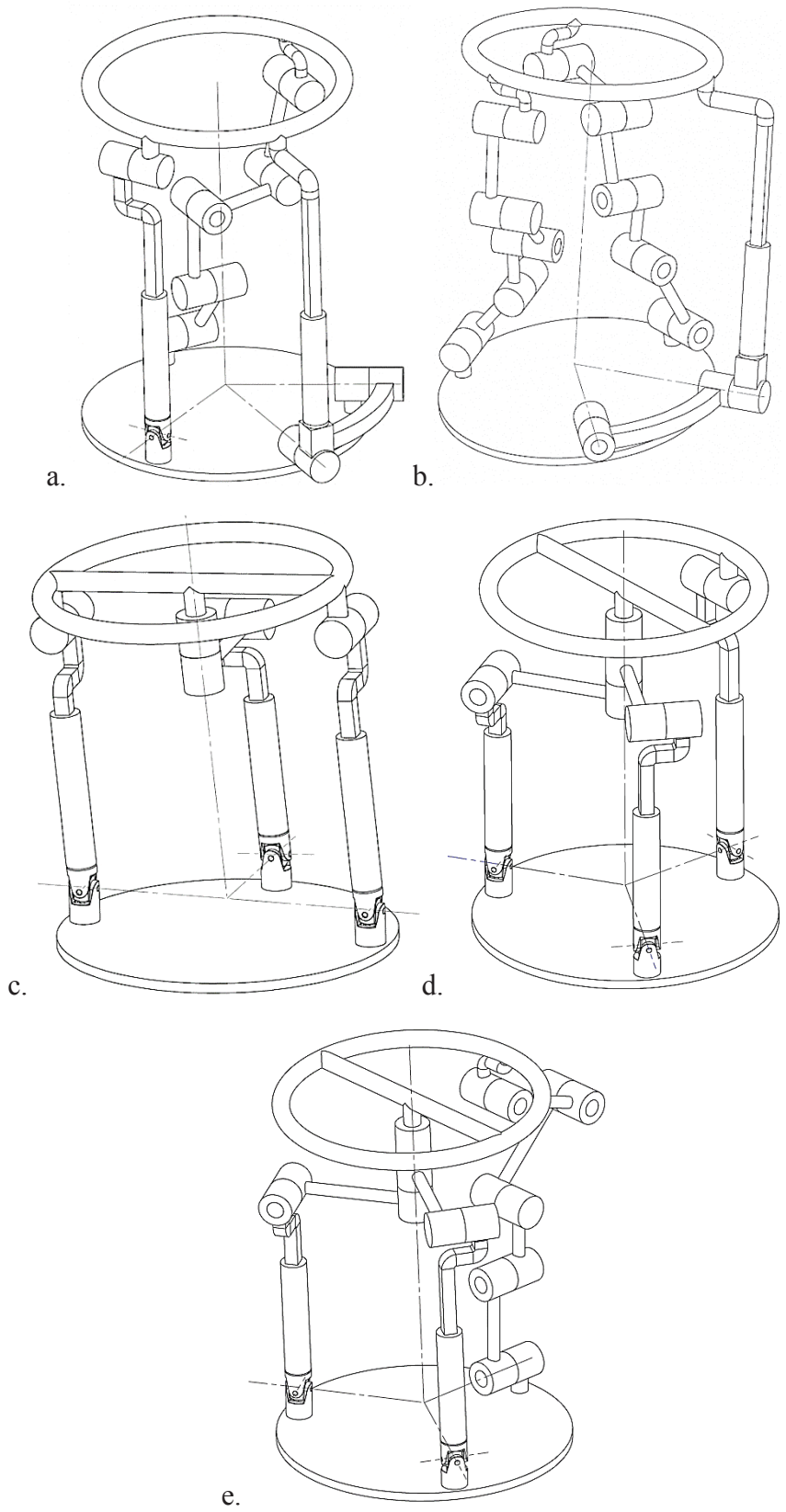

Figure 3.8. Selected 2R1T RCM structures:
a) UR-UPR-RRE b) UP-2-RRE c) 2-UPR-UPRR d) UPR-2-UPRR e) 2-URRR-RRE

These evaluation criteria have various weight factors in accordance with the priorities in design requirements and the weight factors are 3/9, 1/9, 1/9, 2/9 and 2/9, correspondingly. “Ease of balancing” is the most dominant criterion. It is graded between 1-9 according to joint types to be balanced in the legs. “Number of links” criterion is graded between 1-5 such that maximum number of links gets the minimum grade. Other criteria are graded between 1-3. Evaluation chart can be found in Table 3.6.

Table 3.6. Evaluation Chart for possible alternatives

				Evaluation Criteria										
				Balancing		# of limb links		Structural symmetry		Decoupling		Actuation		
Structure Type	no.	Leg-Wrench Systems	Kinematic Structure	Grade	Weighted Grade	Grade	Weighted Grade	Grade	Weighted Grade	Grade	Weighted Grade	Grade	Weighted Grade	Total Grade
Parallel	1	1 (2-F_0-1-F_∞) 2 (1-F_0-1-F_∞)	UR-2-URR	5	18,5	5	11,1	2	7,4	2	14,8	1	7	**59,3**
Parallel	2	1 (2-F_0-1-F_∞) 1 (1-F_0-1-F_∞) 1 (1-F_∞)	UR-URR-RER	5	18,5	2	4,4	1	3,7	2	14,8	2	15	**56,3**
Parallel	3	3 (1-F_0-1-F_∞)	URR-2RE	5	18,5	4	8,9	2	7,4	2	14,8	1	7	**57,0**
Parallel	4	1 (2-F_0-1-F_∞) 2 (1-F_∞)	UR-2RER	5	18,5	1	2,2	2	7,4	2	14,8	2	15	**57,8**
Parallel	5	2 (1-F_0-1-F_∞) 1 (1-F_∞)	2-URR-RRRRR	8	29,6	1	2,2	1	3,7	3	22,2	2	15	**72,6**
Serial	6	spherical 2R and P serial	RRP	3	11,1	5	11,1	1	3,7	1	7,4	1	7	**40,7**
Hybrid	7	2+1 type (two R parallel, P serial)	-	1	3,7037	3	6,7	2	7,4	1	7,4	2	15	**40,0**
Hybrid	8	1+1+1 type (first R and P serial, other R parallel)	-	7	25,9259	4	8,9	0	0,0	3	22,2	1	7	**64,4**

As can be seen in the “Kinematic Structure” column of Table 3.6, all joints are selected as R joints due to ease of construction and balancing. The kinematic structure with the highest grade in the evaluation chart has a 1 (1 F_0-1 F_∞-system) and 2 (1 F_0-system) leg structure. A conceptual CAD model of such a system designed as an RCM manipulator for transnasal surgery is depicted in Figure 3.9. The PM in Figure 3.9 has 2URRR-URR kinematic structure. For this PM, the R joint axes on the base should be intersecting at the pivot point, but the angles between the axes are arbitrary. The R axes of the URRR legs connected to the platform should be concurrent along the w-axis.

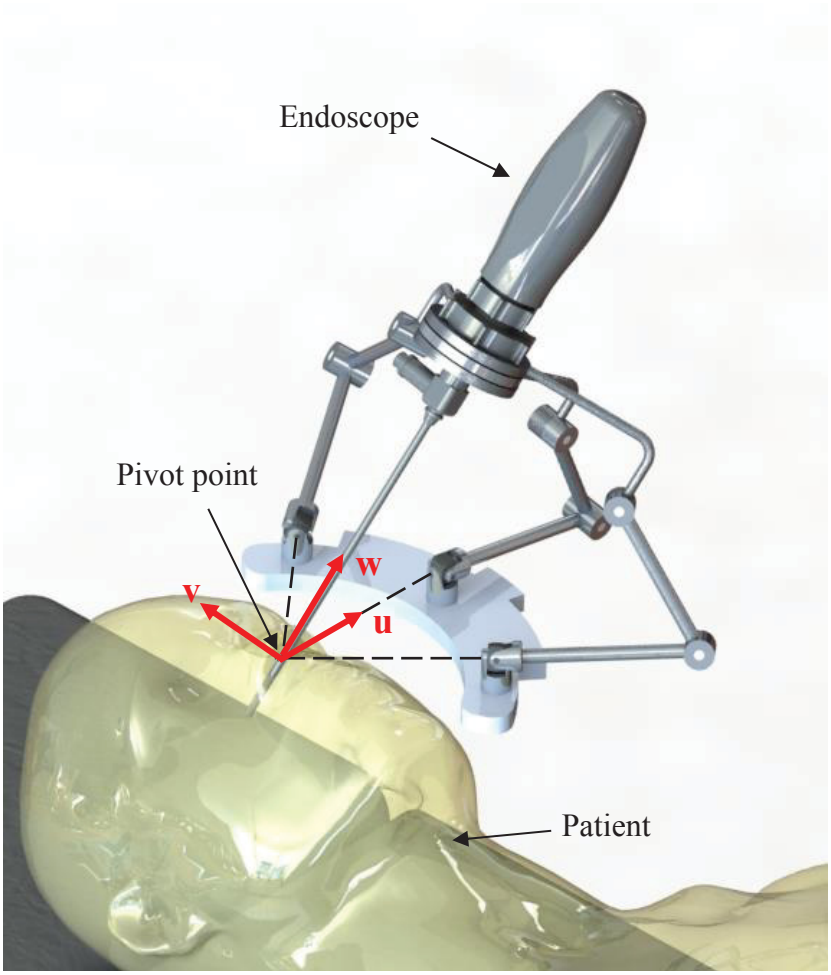

Figure 3.9. Conceptual CAD design of 2URRR-URR RCM manipulator

CHAPTER 4

KINEMATICS

As concluded in the Section 3.6, the kinematic structure of the PM is selected as 2URRR-URR. Kinematic diagram of the mechanism is given in Figure 4.1. In Figure 4.1, the limbs are not distributed with radial symmetry. Normally, it is better to distribute the limbs symmetrically over the base so that the legs balance each other. However, in our case, it is preferred to place them in one side for the sake of providing the surgeon with some open space to perform the surgery. The URR leg is selected as the middle leg while the two URRR legs are selected as the side legs. Except the R joints at A_3 and C_3, all legs have the same kinematic structure as the URR structure, which contains 3 parallel revolute joints. It means that the leg can move on a plane and the angle of this plane can be changed by a revolute joint whose axis is within that plane. Hence, kinematic diagram can be represented by a simpler model which consists of three planes intersecting along

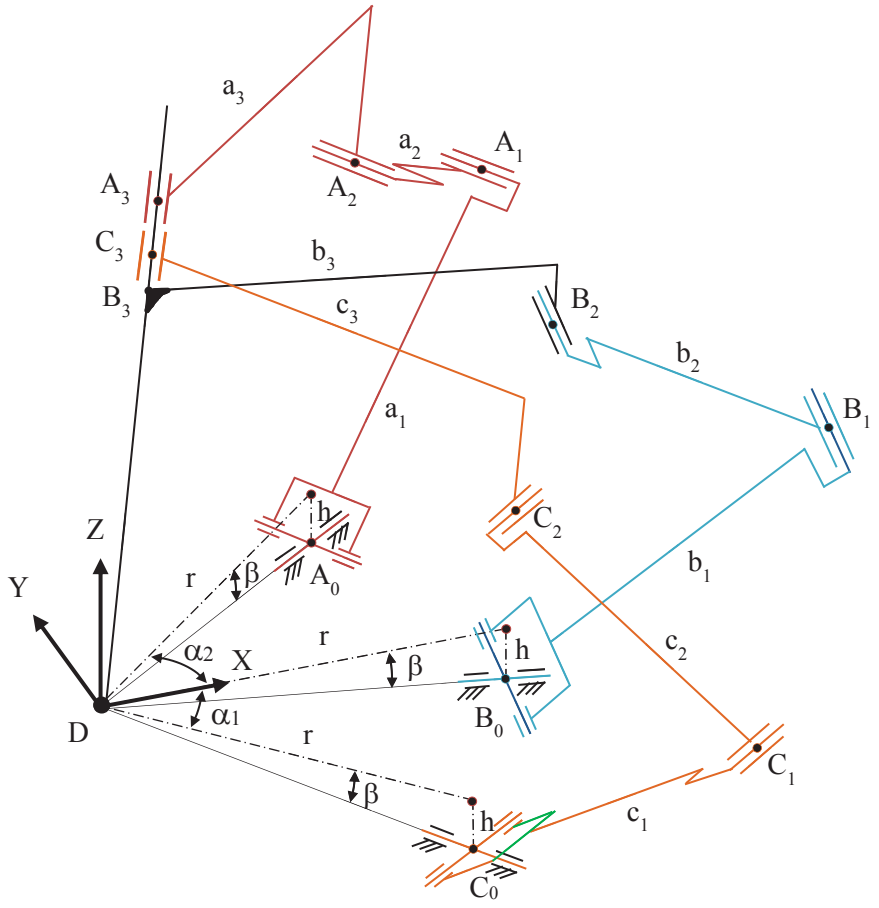

Figure 4.1. Kinematic diagram of the mechanism

a line and the angle of each plane can be changed. As can be seen in Figure 4.2, there are three planes each representing an RRR leg. The planes are intersecting along $\vec{w}$ - unit vector along the end-effector axis. The angles of the side planes are θ_1 and θ_2. Once θ_1 and θ_2 are defined, the angle of the middle plane is already determined because they all have to include $\vec{w}$. Also, unit normal vectors of each plane is shown as $\vec{n}_1$, $\vec{n}_2$, $\vec{n}_3$, respectively. $\hat{X}(\cdot)$, $\hat{Y}(\cdot)$ and $\hat{Z}(\cdot)$ represent the fundamental rotation matrices about X-, Y- and Z-axes, respectively. With the intersecting planes concept, direct and inverse kinematics of the mechanism can easily be formulated. This also results in ease of control for the robot.

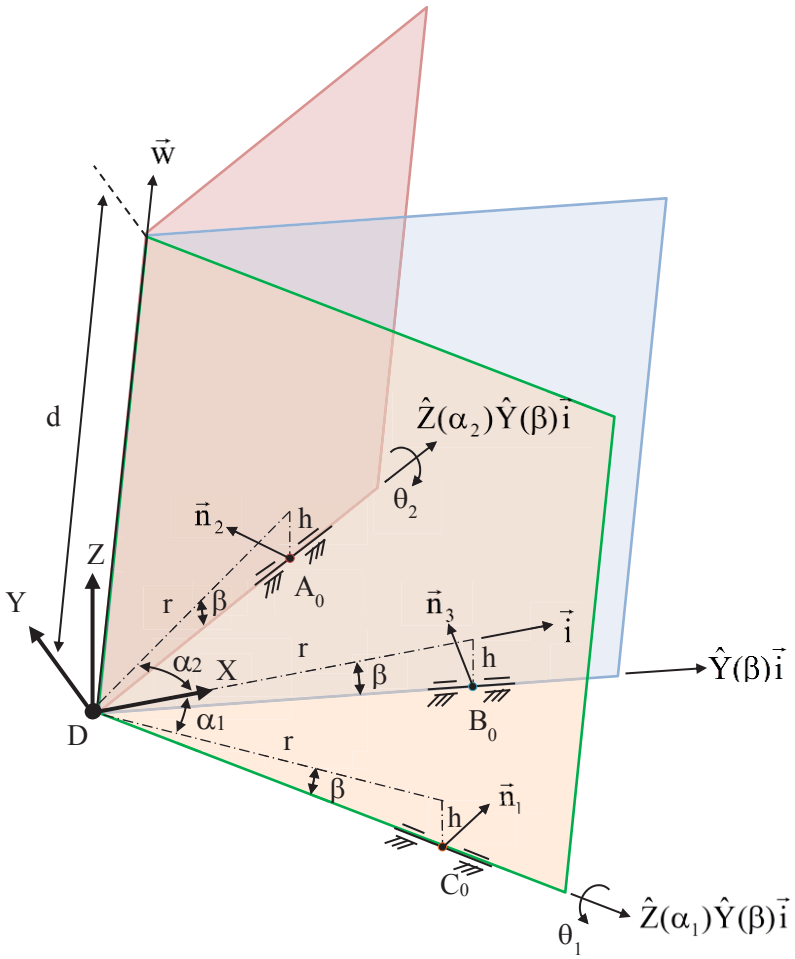

Figure 4.2. Simplified kinematic diagram with three intersecting planes

4.1. Kinematic Analysis

Let ϕ be the angle of $\vec{w}$ with respect to the XZ-plane (corresponding to the yaw motion) and ψ be the angle of $\vec{w}$ with respect to the YZ-plane (corresponding to the pitch motion). Then, $\vec{n}_1$, $\vec{n}_2$ and $\vec{w}$ vectors can be found as follows:

$$\vec{n}_1 = \hat{Z}(\alpha_1)\hat{Y}(\beta)\hat{X}(\theta_1)\begin{bmatrix}0\\1\\0\end{bmatrix} = \begin{bmatrix}c\alpha_1 & -s\alpha_1 & 0\\ s\alpha_1 & c\alpha_1 & 0\\ 0 & 0 & 1\end{bmatrix}\begin{bmatrix}c\beta & 0 & s\beta\\ 0 & 1 & 0\\ -s\beta & 0 & c\beta\end{bmatrix}\begin{bmatrix}1 & 0 & 0\\ 0 & c\theta_1 & -s\theta_1\\ 0 & s\theta_1 & c\theta_1\end{bmatrix}\begin{bmatrix}0\\1\\0\end{bmatrix} \tag{4.1}$$

$$\Rightarrow \vec{n}_1 = \begin{bmatrix}c\alpha_1 s\beta s\theta_1 - s\alpha_1 c\theta_1\\ s\alpha_1 s\beta s\theta_1 + c\alpha_1 c\theta_1\\ c\beta s\theta_1\end{bmatrix} \tag{4.2}$$

$$\vec{n}_2 = \hat{Z}(\alpha_2)\hat{Y}(\beta)\hat{X}(\theta_2)\begin{bmatrix}0\\1\\0\end{bmatrix} = \begin{bmatrix}c\alpha_2 s\beta s\theta_2 - s\alpha_2 c\theta_2\\ s\alpha_2 s\beta s\theta_2 + c\alpha_2 c\theta_2\\ c\beta s\theta_2\end{bmatrix} \tag{4.3}$$

$$\vec{w} = \begin{bmatrix}s\psi\\ -s\phi\\ \sqrt{1-s^2\phi-s^2\psi}\end{bmatrix} \tag{4.4}$$

where $c\alpha$ and $s\psi$ refer to $\cos\alpha$ and $\sin\psi$, respectively. From Figure 4.2:

$$\vec{w} = \begin{bmatrix}s\psi\\ -s\phi\\ \sqrt{1-s^2\phi-s^2\psi}\end{bmatrix} = \frac{\vec{n}_1 \times \vec{n}_2}{|\vec{n}_1 \times \vec{n}_2|} \tag{4.5}$$

where

$$\vec{n}_1 \times \vec{n}_2 = \begin{vmatrix} \mathbf{i} & \mathbf{j} & \mathbf{k} \\ c\alpha_1 s\beta s\theta_1 - s\alpha_1 c\theta_1 & s\alpha_1 s\beta s\theta_1 + c\alpha_1 c\theta_1 & c\beta s\theta_1 \\ c\alpha_2 s\beta s\theta_2 - s\alpha_2 c\theta_2 & s\alpha_2 s\beta s\theta_2 + c\alpha_2 c\theta_2 & c\beta s\theta_2 \end{vmatrix} \tag{4.6}$$

$$\vec{n}_1 \times \vec{n}_2 = \begin{bmatrix} (s\alpha_1 - s\alpha_2)c\beta s\beta s\theta_1 s\theta_2 + c\alpha_1 c\beta c\theta_1 s\theta_2 - c\alpha_2 c\beta s\theta_1 c\theta_2 \\ (c\alpha_2 - c\alpha_1)c\beta s\beta s\theta_1 s\theta_2 - s\alpha_2 c\beta s\theta_1 c\theta_2 + s\alpha_1 c\beta c\theta_1 s\theta_2 \\ s(\alpha_2 - \alpha_1)(c\theta_1 c\theta_2 + s^2\beta s\theta_1 s\theta_2) + c(\alpha_2 - \alpha_1)s\beta s(\theta_1 - \theta_2) \end{bmatrix} \tag{4.7}$$

Let $\alpha_1 = -\alpha$ and $\alpha_2 = \alpha$. Then,

$$\vec{n}_1 \times \vec{n}_2 = \begin{bmatrix} -s\alpha s2\beta s\theta_1 s\theta_2 + c\alpha c\beta s(\theta_2 - \theta_1) \\ -s\alpha c\beta s(\theta_1 + \theta_2) \\ s2\alpha(c\theta_1 c\theta_2 + s^2\beta s\theta_1 s\theta_2) + c2\alpha s\beta s(\theta_1 - \theta_2) \end{bmatrix} \tag{4.8}$$

$$\Rightarrow |\vec{n}_1 \times \vec{n}_2| = \sqrt{\begin{matrix} (-s\alpha s2\beta s\theta_1 s\theta_2 + c\alpha c\beta s(\theta_2 - \theta_1))^2 + (s\alpha c\beta s(\theta_1 + \theta_2))^2 \\ + (s2\alpha(c\theta_1 c\theta_2 + s^2\beta s\theta_1 s\theta_2) + c2\alpha s\beta s(\theta_1 - \theta_2))^2 \end{matrix}} \tag{4.9}$$

In Figure 4.3.a, base segment DA_3, leg 3 chain $A_3B_3C_3$, platform segment C_3E and end-effector line ED are coplanar. DA_3 direction is obtained by rotating X-axis about Y-axis by angle β. So unit vector along DA_3 is $\vec{x}_3 = [c\beta \;\; 0 \;\; -s\beta]^T$. Unit vector $\vec{w}$ along DE is already known. So, A_3DE angle γ can be found as:

$$\gamma = \cos^{-1}(\vec{w} \cdot \vec{x}_3) = \cos^{-1}\left(c\beta s\psi - s\beta\sqrt{1 - s^2\phi - s^2\psi}\right)$$

In local coordinates, $\vec{x}_3$ is the horizontal axis. So, locations of C_3 and B_3 are $(d - ic_3)e^{i\gamma}$ and $f + a_3e^{i\theta_3}$, respectively. Then,

$$\left|\left(d-ic_3\right)e^{i\gamma}-f-a_3e^{i\theta_3}\right|=b_3 \tag{4.10}$$

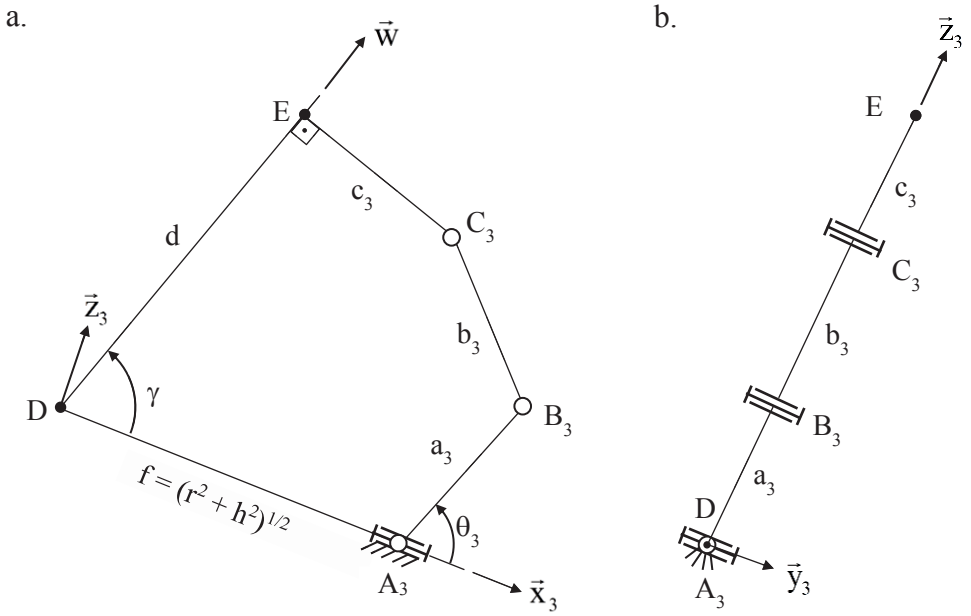

Figure 4.3 Views normal to a) $\vec{n}_3$ or $\vec{x}_3\vec{z}_3$ plane b) $\vec{y}_3\vec{z}_3$ plane

Direct kinematics:

For direct kinematics, by using (4.8) and (4.9), ψ and ϕ can be found as:

$$\psi=\sin^{-1}\frac{-s\alpha s2\beta s\theta_1 s\theta_2+c\alpha c\beta s\left(\theta_2-\theta_1\right)}{\left|\vec{n}_1\times\vec{n}_2\right|} \tag{4.11}$$

$$\phi=\sin^{-1}\frac{s\alpha c\beta s\left(\theta_1+\theta_2\right)}{\left|\vec{n}_1\times\vec{n}_2\right|} \tag{4.12}$$

If all the terms at the left hand side of (4.10) are divided by $e^{i\gamma}$, d can be found with the following steps:

$$\left|d-\left[ic_3+fe^{-i\gamma}+a_3e^{i(\theta_3-\gamma)}\right]\right|=b_3 \tag{4.13}$$

$$\left(d-\left[ic_3+fe^{-i\gamma}+a_3e^{i(\theta_3-\gamma)}\right]\right)\left(d-\left[-ic_3+fe^{i\gamma}+a_3e^{-i(\theta_3-\gamma)}\right]\right)=b_3{}^2 \tag{4.14}$$

$$\begin{aligned}d^2-2d\left[fc\gamma+a_3c(\theta_3-\gamma)\right]+\left[fc\gamma+a_3c(\theta_3-\gamma)\right]^2\\ +\left[c_3-fs\gamma+a_3s(\theta_3-\gamma)\right]^2-b_3{}^2=0\end{aligned} \tag{4.15}$$

$$d=fc\gamma+a_3c(\theta_3-\gamma)+\sqrt{b_3{}^2-\left[c_3-fs\gamma+a_3s(\theta_3-\gamma)\right]^2} \tag{4.16}$$

Inverse kinematics:

For the inverse kinematics, since $\vec{w}$ and $\vec{n}_1$ are orthogonal vectors, $\vec{w}^T\cdot\vec{n}_1=0$. Using (4.1) and (4.4),

$$\vec{w}^T\cdot\vec{n}_1=\begin{bmatrix}s\psi\\-s\phi\\\sqrt{1-s^2\phi-s^2\psi}\end{bmatrix}\cdot\begin{bmatrix}c\alpha s\beta s\theta_1+s\alpha c\theta_1\\-s\alpha s\beta s\theta_1+c\alpha c\theta_1\\c\beta s\theta_1\end{bmatrix}=0 \tag{4.17}$$

$$\vec{w}^T\cdot\vec{n}_1=(s\psi s\alpha-s\phi c\alpha)c\theta_1+\begin{pmatrix}(s\psi c\alpha+s\phi s\alpha)s\beta+\\\sqrt{1-s^2\phi-s^2\psi}c\beta\end{pmatrix}s\theta_1=0 \tag{4.18}$$

So, θ_1 can be found by solving (4.18) as

$$\theta_1=\tan^{-1}\frac{s\phi c\alpha-s\psi s\alpha}{(s\psi c\alpha+s\phi s\alpha)s\beta+\sqrt{1-s^2\phi-s^2\psi}c\beta} \tag{4.19}$$

Following similar procedure with $\vec{w}^T \cdot \vec{n}_2 = 0$, θ_2 can be found as

$$\theta_2 = \tan^{-1} \frac{s\phi c\alpha + s\psi s\alpha}{(s\psi c\alpha - s\phi s\alpha)s\beta + \sqrt{1 - s^2\phi - s^2\psi}c\beta} \tag{4.20}$$

When both sides of (4.10) are squared, it yields,

$$(dc\gamma + c_3 s\gamma - f - a_3 c\theta_3)^2 + (ds\gamma - c_3 c\gamma - a_3 s\theta_3)^2 = {b_3}^2 \tag{4.21}$$

$$2a_3(dc\gamma + c_3 s\gamma - f)c\theta_3 + 2a_3(ds\gamma - c_3 c\gamma)s\theta_3 = (dc\gamma + c_3 s\gamma - f)^2 + (ds\gamma - c_3 c\gamma)^2 + {a_3}^2 - {b_3}^2 \tag{4.22}$$

$$\Rightarrow Ac\theta_3 + Bs\theta_3 = C \tag{4.23}$$

where $A = 2a_3(dc\gamma + c_3 s\gamma - f)$, $B = 2a_3(ds\gamma - c_3 c\gamma)$ and $C = (dc\gamma + c_3 s\gamma - f)^2 + (ds\gamma - c_3 c\gamma)^2 + {a_3}^2 - {b_3}^2$

Let $A = Mc\delta$, $B = Ms\delta$ such that $M = \sqrt{A^2 + B^2} = |\overrightarrow{A_0 A_2}|$ and $\delta = a\tan 2(A, B) = R\overrightarrow{A_3 C_3}$.

Then

$$Ac\theta_3 + Bs\theta_3 = Mc(\theta_3 - \delta) = C \tag{4.24}$$

So, θ_3 can be found as:

$$\Rightarrow \theta_3 = \delta - \cos^{-1}(C/M) \tag{4.25}$$

Velocity Kinematics:

From (4.4), (4.5) and (4.8),

$$\vec{w}=\begin{bmatrix} s\psi \\ -s\phi \\ \sqrt{1-s^2\phi-s^2\psi} \end{bmatrix}=\frac{1}{\left|\vec{n}_1\times\vec{n}_2\right|}\begin{bmatrix} -s\alpha s2\beta s\theta_1 s\theta_2+c\alpha c\beta s\left(\theta_2-\theta_1\right) \\ -s\alpha c\beta s\left(\theta_1+\theta_2\right) \\ s2\alpha\left(c\theta_1 c\theta_2+s^2\beta s\theta_1 s\theta_2\right)+c2\alpha s\beta s\left(\theta_1-\theta_2\right) \end{bmatrix} \tag{4.26}$$

So, the following equalities can be written:

$$\begin{aligned} &\frac{-s\alpha s2\beta s\theta_1 s\theta_2+c\alpha c\beta s\left(\theta_2-\theta_1\right)}{s\psi}=\frac{s\alpha c\beta s\left(\theta_1+\theta_2\right)}{s\phi}=\ldots \\ &\qquad\ldots\ \frac{s2\alpha\left(c\left(\theta_2-\theta_1\right)-c^2\beta s\theta_1 s\theta_2\right)+c2\alpha s\beta s\left(\theta_1-\theta_2\right)}{\sqrt{1-s^2\phi-s^2\psi}} \end{aligned} \tag{4.27}$$

$$\begin{aligned} f_1\left(\theta_1,\theta_2,\phi,\psi\right)=&\sqrt{1-s^2\phi-s^2\psi}\left[-s\alpha s2\beta s\theta_1 s\theta_2+c\alpha c\beta s\left(\theta_2-\theta_1\right)\right] \\ &-s\psi\left[s2\alpha\left(c\left(\theta_2-\theta_1\right)-c^2\beta s\theta_1 s\theta_2\right)+c2\alpha s\beta s\left(\theta_1-\theta_2\right)\right]=0 \end{aligned} \tag{4.28}$$

$$\begin{aligned} f_2\left(\theta_1,\theta_2,\phi,\psi\right)=&\sqrt{1-s^2\phi-s^2\psi}s\alpha c\beta s\left(\theta_1+\theta_2\right) \\ &-s\phi\left[s2\alpha\left(c\left(\theta_2-\theta_1\right)-c^2\beta s\theta_1 s\theta_2\right)+c2\alpha s\beta s\left(\theta_1-\theta_2\right)\right]=0 \end{aligned} \tag{4.29}$$

(4.30), (4.31) can be obtained by taking time derivative of (4.28) and (4.29).

$$\begin{aligned} \frac{df_1}{dt}&=\frac{\partial f_1}{\partial\theta_1}\dot{\theta}_1+\frac{\partial f_1}{\partial\theta_2}\dot{\theta}_2+\frac{\partial f_1}{\partial\phi}\dot{\phi}+\frac{\partial f_1}{\partial\psi}\dot{\psi}=0 \\ \frac{df_2}{dt}&=\frac{\partial f_2}{\partial\theta_1}\dot{\theta}_1+\frac{\partial f_2}{\partial\theta_2}\dot{\theta}_2+\frac{\partial f_2}{\partial\phi}\dot{\phi}+\frac{\partial f_2}{\partial\psi}\dot{\psi}=0 \end{aligned} \tag{4.30}$$

$$\Rightarrow\begin{bmatrix} \frac{\partial f_1}{\partial\theta_1} & \frac{\partial f_1}{\partial\theta_2} \\ \frac{\partial f_2}{\partial\theta_1} & \frac{\partial f_2}{\partial\theta_2} \end{bmatrix}\begin{bmatrix} \dot{\theta}_1 \\ \dot{\theta}_2 \end{bmatrix}=\begin{bmatrix} -\frac{\partial f_1}{\partial\phi} & -\frac{\partial f_1}{\partial\psi} \\ -\frac{\partial f_2}{\partial\phi} & -\frac{\partial f_2}{\partial\psi} \end{bmatrix}\begin{bmatrix} \dot{\phi} \\ \dot{\psi} \end{bmatrix} \tag{4.31}$$

where

$$\frac{\partial f_1}{\partial \theta_1} = \sqrt{1-s^2\phi-s^2\psi}\left[-s\alpha s2\beta c\theta_1 s\theta_2 - c\alpha c\beta c(\theta_2-\theta_1)\right] - s\psi\left[s2\alpha\left(s(\theta_2-\theta_1)-c^2\beta c\theta_1 s\theta_2\right)+c2\alpha s\beta c(\theta_1-\theta_2)\right]$$

$$\frac{\partial f_1}{\partial \theta_2} = \sqrt{1-s^2\phi-s^2\psi}\left[-s\alpha s2\beta s\theta_1 c\theta_2 + c\alpha c\beta c(\theta_2-\theta_1)\right] - s\psi\left[s2\alpha\left(-s(\theta_2-\theta_1)-c^2\beta s\theta_1 c\theta_2\right)-c2\alpha s\beta c(\theta_1-\theta_2)\right]$$

$$\frac{\partial f_1}{\partial \phi} = \frac{-s\phi c\phi}{\sqrt{1-s^2\phi-s^2\psi}}\left[-s\alpha s2\beta s\theta_1 s\theta_2 + c\alpha c\beta s(\theta_2-\theta_1)\right]$$

$$\frac{\partial f_1}{\partial \psi} = \frac{-s\psi c\psi}{\sqrt{1-s^2\phi-s^2\psi}}\left[-s\alpha s2\beta s\theta_1 s\theta_2 + c\alpha c\beta s(\theta_2-\theta_1)\right] - c\psi\left[s2\alpha\left(c(\theta_2-\theta_1)-c^2\beta s\theta_1 s\theta_2\right)+c2\alpha s\beta s(\theta_1-\theta_2)\right]$$

$$\frac{\partial f_2}{\partial \theta_1} = \sqrt{1-s^2\phi-s^2\psi}s\alpha c\beta c(\theta_1+\theta_2) - s\phi\left[\begin{array}{r} s2\alpha\left(s(\theta_2-\theta_1)-c^2\beta c\theta_1 s\theta_2\right) \\ +c2\alpha s\beta c(\theta_1-\theta_2)\end{array}\right]$$

$$\frac{\partial f_2}{\partial \theta_2} = \sqrt{1-s^2\phi-s^2\psi}s\alpha c\beta c(\theta_1+\theta_2) + s\phi\left[s2\alpha\left(s(\theta_2-\theta_1)+c^2\beta s\theta_1 c\theta_2\right)+c2\alpha s\beta c(\theta_1-\theta_2)\right]$$

$$\frac{\partial f_2}{\partial \phi} = -\frac{s\phi c\phi s\alpha c\beta s(\theta_1+\theta_2)}{\sqrt{1-s^2\phi-s^2\psi}} - c\phi\left[s2\alpha\left(c(\theta_2-\theta_1)-c^2\beta s\theta_1 s\theta_2\right)+c2\alpha s\beta s(\theta_1-\theta_2)\right]$$

$$\frac{\partial f_2}{\partial \psi} = -\frac{s\psi c\psi s\alpha c\beta s(\theta_1+\theta_2)}{\sqrt{1-s^2\phi-s^2\psi}}$$

For $\beta = 0$ (explained in Section 4.2), (4.9), (4.26), (4.27), (4.28), (4.29), (4.30) and (4.31) simplify to (4.32), (4.33), (4.34), (4.35), (4.36), (4.37) and (4.38), respectively.

$$\left|\mathbf{n}_1 \times \mathbf{n}_2\right| = \sqrt{s^2\theta_2 c^2\theta_1 + c^2\theta_2 s^2\theta_1 - 2c2\alpha c\theta_1 s\theta_1 c\theta_2 s\theta_2 + 4s^2\alpha c^2\alpha c^2\theta_1 c^2\theta_2} \qquad (4.32)$$

$$\vec{w} = \begin{bmatrix} s\psi \\ -s\phi \\ \sqrt{1-s^2\phi-s^2\psi} \end{bmatrix} = \frac{1}{\left|\vec{n}_1 \times \vec{n}_2\right|} \begin{bmatrix} c\alpha s\left(\theta_2-\theta_1\right) \\ -s\alpha s\left(\theta_1+\theta_2\right) \\ s2\alpha c\theta_1 c\theta_2 \end{bmatrix} \tag{4.33}$$

$$\Rightarrow \frac{c\alpha s\left(\theta_2-\theta_1\right)}{s\psi} = \frac{s\alpha s\left(\theta_1+\theta_2\right)}{s\phi} = \frac{s2\alpha c\theta_1 c\theta_2}{\sqrt{1-s^2\phi-s^2\psi}} \tag{4.34}$$

$$\Rightarrow f_1\left(\theta_1,\theta_2,\phi,\psi\right) = \sqrt{1-s^2\phi-s^2\psi}\, s\left(\theta_2-\theta_1\right) - 2s\psi s\alpha c\theta_1 c\theta_2 = 0 \tag{4.35}$$

$$\Rightarrow f_2\left(\theta_1,\theta_2,\phi,\psi\right) = \sqrt{1-s^2\phi-s^2\psi}\, s\left(\theta_1+\theta_2\right) - 2s\phi c\alpha c\theta_1 c\theta_2 = 0 \tag{4.36}$$

$$\begin{aligned} \frac{df_1}{dt} &= \frac{\partial f_1}{\partial\theta_1}\dot{\theta}_1 + \frac{\partial f_1}{\partial\theta_2}\dot{\theta}_2 + \frac{\partial f_1}{\partial\phi}\dot{\phi} + \frac{\partial f_1}{\partial\psi}\dot{\psi} = 0 \\ \frac{df_2}{dt} &= \frac{\partial f_2}{\partial\theta_1}\dot{\theta}_1 + \frac{\partial f_2}{\partial\theta_2}\dot{\theta}_2 + \frac{\partial f_2}{\partial\phi}\dot{\phi} + \frac{\partial f_2}{\partial\psi}\dot{\psi} = 0 \end{aligned} \tag{4.37}$$

$$\Rightarrow \begin{bmatrix} \frac{\partial f_1}{\partial\theta_1} & \frac{\partial f_1}{\partial\theta_2} \\ \frac{\partial f_2}{\partial\theta_1} & \frac{\partial f_2}{\partial\theta_2} \end{bmatrix} \begin{bmatrix} \dot{\theta}_1 \\ \dot{\theta}_2 \end{bmatrix} = \begin{bmatrix} -\frac{\partial f_1}{\partial\phi} & -\frac{\partial f_1}{\partial\psi} \\ -\frac{\partial f_2}{\partial\phi} & -\frac{\partial f_2}{\partial\psi} \end{bmatrix} \begin{bmatrix} \dot{\phi} \\ \dot{\psi} \end{bmatrix} \tag{4.38}$$

where

$$\frac{\partial f_1}{\partial\theta_1} = -\sqrt{1-s^2\phi-s^2\psi}\, c\left(\theta_2-\theta_1\right) + 2s\psi s\alpha s\theta_1 c\theta_2$$

$$\frac{\partial f_1}{\partial\theta_2} = \sqrt{1-s^2\phi-s^2\psi}\, c\left(\theta_2-\theta_1\right) + 2s\psi s\alpha c\theta_1 s\theta_2$$

$$\frac{\partial f_1}{\partial\phi} = \frac{-s\phi c\phi s\left(\theta_2-\theta_1\right)}{\sqrt{1-s^2\phi-s^2\psi}} \;;\; \frac{\partial f_1}{\partial\psi} = \frac{-s\psi c\psi s\left(\theta_2-\theta_1\right)}{\sqrt{1-s^2\phi-s^2\psi}} - 2c\psi s\alpha c\theta_1 c\theta_2$$

$$\frac{\partial f_2}{\partial \theta_1} = \sqrt{1-s^2\phi-s^2\psi}\,c\left(\theta_1+\theta_2\right)+2s\phi c\alpha s\theta_1 c\theta_2$$

$$\frac{\partial f_2}{\partial \theta_2} = \sqrt{1-s^2\phi-s^2\psi}\,c\left(\theta_1+\theta_2\right)+2s\phi c\alpha c\theta_1 s\theta_2$$

$$\frac{\partial f_2}{\partial \phi} = -\frac{s\phi c\phi s\left(\theta_1+\theta_2\right)}{\sqrt{1-s^2\phi-s^2\psi}}-2c\phi c\alpha c\theta_1 c\theta_2;\quad \frac{\partial f_2}{\partial \psi} = -\frac{s\psi c\psi s\left(\theta_1+\theta_2\right)}{\sqrt{1-s^2\phi-s^2\psi}}$$

Rearranging (4.23):

$$\begin{aligned} f_3\left(d,\psi,\phi,\theta_3\right) = d^2 - 2d\left[fc\gamma + a_3 c\left(\theta_3-\gamma\right)\right] + \left[fc\gamma + a_3 c\left(\theta_3-\gamma\right)\right]^2 \\ + \left[c_3 - fs\gamma + a_3 s\left(\theta_3-\gamma\right)\right]^2 - {b_3}^2 = 0 \end{aligned} \tag{4.39}$$

where $\gamma = \cos^{-1}\left(c\beta\, s\,\psi - s\beta\sqrt{1-s^2\phi-s^2\psi}\right)$. Similarly, (4.41) and (4.42) can be found by using (4.40).

$$\frac{df_3}{dt} = \frac{\partial f_3}{\partial d}\dot{d} + \frac{\partial f_3}{\partial \psi}\dot{\psi} + \frac{\partial f_3}{\partial \phi}\dot{\phi} + \frac{\partial f_3}{\partial \theta_3}\dot{\theta}_3 = 0 \tag{4.40}$$

$$\dot{\theta}_3 = -\left(\frac{\partial f_3}{\partial d}\dot{d} + \frac{\partial f_3}{\partial \psi}\dot{\psi} + \frac{\partial f_3}{\partial \phi}\dot{\phi}\right)\Big/\frac{\partial f_3}{\partial \theta_3} \tag{4.41}$$

or

$$\dot{d} = -\left(\frac{\partial f_3}{\partial \psi}\dot{\psi} + \frac{\partial f_3}{\partial \phi}\dot{\phi} + \frac{\partial f_3}{\partial \theta_3}\dot{\theta}_3\right)\Big/\frac{\partial f_3}{\partial d} \tag{4.42}$$

where

$$\frac{\partial f_3}{\partial d} = 2\left[d - fc\gamma - a_3 c\left(\theta_3-\gamma\right)\right]$$

$$\frac{\partial f_3}{\partial \theta_3} = 2a_3 s(\theta_3 - \gamma)\left[d - fc\gamma - a_3 c(\theta_3 - \gamma)\right] + 2a_3 c(\theta_3 - \gamma)\left[c_3 - fs\gamma + a_3 s(\theta_3 - \gamma)\right]$$

$$\frac{\partial f_3}{\partial \psi} = \frac{\partial f_3}{\partial \gamma}\frac{\partial \gamma}{\partial \psi} \text{ and } \frac{\partial f_3}{\partial \phi} = \frac{\partial f_3}{\partial \gamma}\frac{\partial \gamma}{\partial \phi}$$

$$\frac{\partial f_3}{\partial \psi} = -2\begin{Bmatrix}\left[fs\gamma - a_3 s(\theta_3 - \gamma)\right]\left[d - fc\gamma - a_3 c(\theta_3 - \gamma)\right] \\ -\left[fc\gamma + a_3 c(\theta_3 - \gamma)\right]\left[c_3 - fs\gamma + a_3 s(\theta_3 - \gamma)\right]\end{Bmatrix}\frac{c\psi}{s\gamma}\left[c\beta + \frac{s\beta s\psi}{\sqrt{1 - s^2\phi - s^2\psi}}\right]$$

$$\frac{\partial f_3}{\partial \phi} = -2\begin{Bmatrix}\left[fs\gamma - a_3 s(\theta_3 - \gamma)\right]\left[d - fc\gamma - a_3 c(\theta_3 - \gamma)\right] \\ -\left[fc\gamma + a_3 c(\theta_3 - \gamma)\right]\left[c_3 - fs\gamma + a_3 s(\theta_3 - \gamma)\right]\end{Bmatrix}\frac{s\beta s\phi c\phi}{s\gamma\sqrt{1 - s^2\phi - s^2\psi}}$$

Now, the relationship between joint space and task space velocities can be constructed as:

$$\begin{bmatrix} \frac{\partial f_1}{\partial \theta_1} & \frac{\partial f_1}{\partial \theta_2} & 0 \\ \frac{\partial f_2}{\partial \theta_1} & \frac{\partial f_2}{\partial \theta_2} & 0 \\ 0 & 0 & \frac{\partial f_3}{\partial \theta_3} \end{bmatrix}\begin{bmatrix}\dot{\theta}_1 \\ \dot{\theta}_2 \\ \dot{\theta}_3\end{bmatrix} = \begin{bmatrix} -\frac{\partial f_1}{\partial \phi} & -\frac{\partial f_1}{\partial \psi} & 0 \\ -\frac{\partial f_2}{\partial \phi} & -\frac{\partial f_2}{\partial \psi} & 0 \\ -\frac{\partial f_3}{\partial \phi} & -\frac{\partial f_3}{\partial \psi} & -\frac{\partial f_3}{\partial d} \end{bmatrix}\begin{bmatrix}\dot{\phi} \\ \dot{\psi} \\ \dot{d}\end{bmatrix} \tag{4.43}$$

For the part involving the orientation of the end-effector line only

$$\begin{bmatrix} \frac{\partial f_1}{\partial \theta_1} & \frac{\partial f_1}{\partial \theta_2} \\ \frac{\partial f_2}{\partial \theta_1} & \frac{\partial f_2}{\partial \theta_2} \end{bmatrix}\begin{bmatrix}\dot{\theta}_1 \\ \dot{\theta}_2\end{bmatrix} = \begin{bmatrix} -\frac{\partial f_1}{\partial \phi} & -\frac{\partial f_1}{\partial \psi} \\ -\frac{\partial f_2}{\partial \phi} & -\frac{\partial f_2}{\partial \psi} \end{bmatrix}\begin{bmatrix}\dot{\phi} \\ \dot{\psi}\end{bmatrix} \rightarrow \begin{bmatrix}\dot{\theta}_1 \\ \dot{\theta}_2\end{bmatrix} = \hat{J}\begin{bmatrix}\dot{\phi} \\ \dot{\psi}\end{bmatrix} \tag{4.44}$$

where

$$\hat{J} = \frac{1}{\frac{\partial f_1}{\partial \theta_1}\frac{\partial f_2}{\partial \theta_2} - \frac{\partial f_2}{\partial \theta_1}\frac{\partial f_1}{\partial \theta_2}} \begin{bmatrix} \frac{\partial f_2}{\partial \theta_2} & -\frac{\partial f_1}{\partial \theta_2} \\ -\frac{\partial f_2}{\partial \theta_1} & \frac{\partial f_1}{\partial \theta_1} \end{bmatrix} \begin{bmatrix} -\frac{\partial f_1}{\partial \phi} & -\frac{\partial f_1}{\partial \psi} \\ -\frac{\partial f_2}{\partial \phi} & -\frac{\partial f_2}{\partial \psi} \end{bmatrix} = \frac{1}{\Delta}\begin{bmatrix} J_{11} & J_{12} \\ J_{21} & J_{22} \end{bmatrix} \quad (4.45)$$

with $J_{11} = \frac{\partial f_1}{\partial \theta_2}\frac{\partial f_2}{\partial \phi} - \frac{\partial f_2}{\partial \theta_2}\frac{\partial f_1}{\partial \phi}$, $J_{12} = \frac{\partial f_1}{\partial \theta_2}\frac{\partial f_2}{\partial \psi} - \frac{\partial f_2}{\partial \theta_2}\frac{\partial f_1}{\partial \psi}$, $J_{21} = \frac{\partial f_2}{\partial \theta_1}\frac{\partial f_1}{\partial \phi} - \frac{\partial f_1}{\partial \theta_1}\frac{\partial f_2}{\partial \phi}$,

$J_{22} = \frac{\partial f_2}{\partial \theta_1}\frac{\partial f_1}{\partial \psi} - \frac{\partial f_1}{\partial \theta_1}\frac{\partial f_2}{\partial \psi}$ and $\Delta = \frac{\partial f_1}{\partial \theta_1}\frac{\partial f_2}{\partial \theta_2} - \frac{\partial f_2}{\partial \theta_1}\frac{\partial f_1}{\partial \theta_2}$

For evaluating the condition number for $\hat{J}$

$$\hat{J}^T\hat{J} = \frac{1}{\Delta^2}\begin{bmatrix} J_{11}^2 + J_{21}^2 & J_{11}J_{12} + J_{21}J_{22} \\ J_{11}J_{12} + J_{21}J_{22} & J_{12}^2 + J_{22}^2 \end{bmatrix} \quad (4.46)$$

$$\Delta^2 \left|\hat{J}^T\hat{J} - \lambda\hat{I}\right| = \begin{vmatrix} J_{11}^2 + J_{21}^2 - \Delta^2\lambda & J_{11}J_{12} + J_{21}J_{22} \\ J_{11}J_{12} + J_{21}J_{22} & J_{12}^2 + J_{22}^2 - \Delta^2\lambda \end{vmatrix} \quad (4.47)$$

$$\begin{aligned} \Delta^2 \left|\hat{J}^T\hat{J} - \lambda\hat{I}\right| &= \left(J_{11}^2 + J_{21}^2 - \Delta^2\lambda\right)\left(J_{12}^2 + J_{22}^2 - \Delta^2\lambda\right) - \left(J_{11}J_{12} + J_{21}J_{22}\right)^2 \\ &= \Delta^4\lambda^2 - \left(J_{11}^2 + J_{12}^2 + J_{21}^2 + J_{22}^2\right)\Delta^2\lambda + \left(J_{11}^2 + J_{21}^2\right)\left(J_{12}^2 + J_{22}^2\right) - \left(J_{11}J_{12} + J_{21}J_{22}\right)^2 \quad (4.48) \\ &= k_1\lambda^2 + k_2\lambda + k_3 = 0 \end{aligned}$$

The eigenvalues of $\hat{J}$ are

$$\Rightarrow \lambda_{1,2} = \frac{-k_2 \mp \sqrt{k_2^2 - 4k_1k_3}}{2k_1} \quad (4.49)$$

Then the condition number of $\hat{J}$ can be found as:

$$\kappa = \sqrt{\frac{\max\left(|\lambda_1|,|\lambda_2|\right)}{\min\left(|\lambda_1|,|\lambda_2|\right)}} \tag{4.50}$$

Eigenvalue for θ_3 can be found by using (4.51) as:

$$\dot{\theta}_3 = -\left(\frac{\partial f_3}{\partial d}\dot{d} + \frac{\partial f_3}{\partial \psi}\dot{\psi} + \frac{\partial f_3}{\partial \phi}\dot{\phi}\right) \Big/ \frac{\partial f_3}{\partial \theta_3} \tag{4.51}$$

Let

$$\overline{J}' = \frac{1}{\partial f_3/\partial \theta_3}\begin{bmatrix} J_1 & J_2 & J_3 \end{bmatrix} \tag{4.52}$$

where $J_1 = \dfrac{\partial f_3}{\partial d}$, $J_2 = \dfrac{\partial f_3}{\partial \psi}$ and $J_3 = \dfrac{\partial f_3}{\partial \phi}$. Then

$$\overline{J}'^{T}\overline{J}' = \frac{1}{\left(\partial f_3/\partial \theta_3\right)^2}\begin{bmatrix} J_1 \\ J_2 \\ J_3 \end{bmatrix}\begin{bmatrix} J_1 & J_2 & J_3 \end{bmatrix} = \frac{1}{\left(\partial f_3/\partial \theta_3\right)^2}\begin{bmatrix} J_1^2 & J_1J_2 & J_1J_3 \\ J_1J_2 & J_2^2 & J_2J_3 \\ J_1J_3 & J_2J_3 & J_3^2 \end{bmatrix} \tag{4.53}$$

The nonzero eigenvalue can be found as:

$$\lambda = \left(J_1^2 + J_2^2 + J_3^2\right) \Big/ \left(\partial f_3/\partial \theta_3\right)^2 \tag{4.54}$$

The condition number in (4.49) and the eigenvalue in (4.53) are to be used in the kinematic design of the manipulator considering optimal force transmission characteristics.

4.2. Kinematic Design

In the kinematic design phase, firstly, the workspace of the manipulator needs to be defined. Dede et al. (2018) presented the desired workspace of the surgery area by using accelerometers mounted on an endoscope, which is placed and moved in the nasal cavity and by using data from a computed tomography scan. The results show that the endoscope has $33°$ for pitch and $23°$ for yaw motion about pivot point and 95 mm for heave motion along the pivot point for a transnasal operation. That is, $\Delta\psi = 33°$, $\Delta\phi = 23°$ and $\Delta d = 95$ mm. However, these values might slightly vary for different patients. So, the workspace of the manipulator is chosen as $\Delta\psi = 40°$, $\Delta\phi = 30°$ and $\Delta d = 100$ mm.

By applying (4.52), the condition numbers for different α and β are computed and tabulated by using Microsoft Excel (Table 4.1). For the each cell, the maximum condition number is found using the formulae in Section 4.1 with angle ϕ varying from -15° to 15° and angle ψ varying from -20° to 20° in the workspace for the specific α and β angles in the table. α = 0° and α = 90° correspond to the cases where all or some of the fixed R joint axes on the base coincide, so the condition number cannot be evaluated for those α values. As highlighted in the table, the minimum condition number (1,06) is obtained for $\alpha = 45°$ and $\beta = 0°$. In addition, for $\alpha = 45°$ and $\beta = 0°$, the condition numbers for the workspace of the manipulator are tabulated with a shaded gradation in Table 4.2. As can be seen, the maximum condition number (1,064) is obtained for $\phi = 0°$ and $\psi = -20°$ or $20°$, that is still very close to 1 which is the ideal condition number. So, the angle values for α and β in the base are optimized in terms of transmission characteristics.

The dimensions of the side legs do not have a significant effect on the input/output relationship of the manipulator. However, a dimensional design is performed for the middle leg. Then, the dimensions of the side legs are selected as same as those of the middle leg.

Table 4.1. Condition numbers for different α and β angles

β (deg) \ α (deg)	0	5	10	15	20	25	30	35	40	45	50	55	60	65	70	75	80	85	90
-45	##	15,0	7,47	4,96	3,70	2,94	2,44	2,08	2,04	2,20	2,58	3,29	4,60	7,54	19,3	107	223	55,6	##
-40	##	14,4	7,16	4,74	3,53	2,80	2,31	1,97	1,76	1,87	2,17	2,70	3,62	5,38	10,1	57,5	208	907	##
-35	##	13,9	6,90	4,57	3,39	2,68	2,21	1,87	1,63	1,65	1,90	2,33	3,04	4,28	6,99	17,6	72,2	115	##
-30	##	13,4	6,69	4,42	3,28	2,59	2,12	1,79	1,55	1,49	1,70	2,07	2,65	3,61	5,47	10,7	124	231	##
-25	##	13,1	6,51	4,30	3,18	2,51	2,05	1,72	1,48	1,36	1,56	1,89	2,39	3,15	4,55	7,8	25,1	117	##
-20	##	12,8	6,36	4,20	3,10	2,43	1,98	1,66	1,41	1,26	1,45	1,78	2,23	2,89	3,98	6,3	14,3	215	##
-15	##	12,5	6,23	4,11	3,03	2,37	1,93	1,60	1,36	1,18	1,39	1,69	2,09	2,67	3,60	5,3	10,1	96,1	##
-10	##	12,3	6,12	4,03	2,97	2,32	1,88	1,56	1,31	1,13	1,33	1,61	1,98	2,50	3,30	4,7	8,06	27,1	##
-5	##	12,2	6,06	3,99	2,94	2,29	1,85	1,53	1,28	1,08	1,28	1,54	1,88	2,35	3,05	4,2	6,78	16,2	##
0	##	12,2	6,04	3,97	2,92	2,28	1,84	1,52	1,27	1,06	1,23	1,48	1,79	2,22	2,84	3,9	5,87	11,8	##
5	##	12,2	6,06	3,99	2,94	2,29	1,85	1,53	1,28	1,08	1,28	1,54	1,88	2,35	3,05	4,2	6,78	16,2	##
10	##	12,3	6,12	4,03	2,97	2,32	1,88	1,56	1,31	1,13	1,33	1,61	1,98	2,50	3,30	4,7	8,06	27,1	##
15	##	12,5	6,23	4,11	3,03	2,37	1,93	1,60	1,36	1,18	1,39	1,69	2,09	2,67	3,60	5,3	10,1	96,1	##
20	##	12,8	6,36	4,20	3,10	2,43	1,98	1,66	1,41	1,26	1,45	1,78	2,23	2,89	3,98	6,3	14,3	215	##
25	##	13,1	6,51	4,30	3,18	2,51	2,05	1,72	1,48	1,36	1,56	1,89	2,39	3,15	4,55	7,8	25,1	117	##
30	##	13,4	6,69	4,42	3,28	2,59	2,12	1,79	1,55	1,49	1,70	2,07	2,65	3,61	5,47	10,7	124	231	##
35	##	13,9	6,90	4,57	3,39	2,68	2,21	1,87	1,63	1,65	1,90	2,33	3,04	4,28	6,99	17,6	72,2	115	##
40	##	14,4	7,16	4,74	3,53	2,80	2,31	1,97	1,76	1,87	2,17	2,70	3,62	5,38	10,1	57,5	208	907	##
45	##	15,0	7,47	4,96	3,70	2,94	2,44	2,08	2,04	2,20	2,58	3,29	4,60	7,54	19,3	107	223	55,6	##

Table 4.2. Condition numbers for the workspace

ψ(deg) \ ϕ (deg)	-15	-12	-9	-6	-3	0	3	6	9	12	15
-20,00	1,028	1,041	1,051	1,059	1,063	1,064	1,063	1,059	1,051	1,041	1,028
-15,56	1,003	1,015	1,025	1,032	1,037	1,038	1,037	1,032	1,025	1,015	1,003
-11,11	1,016	1,003	1,007	1,014	1,018	1,019	1,018	1,014	1,007	1,003	1,016
-6,67	1,028	1,015	1,006	1,001	1,005	1,007	1,005	1,001	1,006	1,015	1,028
-2,22	1,035	1,022	1,012	1,005	1,001	1,001	1,001	1,005	1,012	1,022	1,035
2,22	1,035	1,022	1,012	1,005	1,001	1,001	1,001	1,005	1,012	1,022	1,035
6,67	1,028	1,015	1,006	1,001	1,005	1,007	1,005	1,001	1,006	1,015	1,028
11,11	1,016	1,003	1,007	1,014	1,018	1,019	1,018	1,014	1,007	1,003	1,016
15,56	1,003	1,015	1,025	1,032	1,037	1,038	1,037	1,032	1,025	1,015	1,003
20,00	1,028	1,041	1,051	1,059	1,063	1,064	1,063	1,059	1,051	1,041	1,028

Slider-crank design for the center leg:

In the middle plane, the middle leg can be considered as a slider-crank mechanism with a crank A_3B_3, a connecting rod B_3C_3 and a slider on C_3 sliding parallel to line DE (Figure 4.4). The plane of this slider-crank mechanism can be rotated about the $\mathbf{x}_3$-axis. Also, the angle of the sliding direction of the slider can be changed by the angle γ. For this slider-crank mechanism, constant DEC_3 angle is chosen as $90°$ for maximum force transmission. Since β is determined as 0, $h = 0$ and $f = r$ (Figure 4.1). Choice of c_3 is arbitrary. However, numerical simulations show that $c_3 = r$ results in better transmission characteristics. Choice of r depends on the application. For our application it is determined according to the dimension of a typical patient's head. So, only the parameters a_3 and b_3 are to be designed.

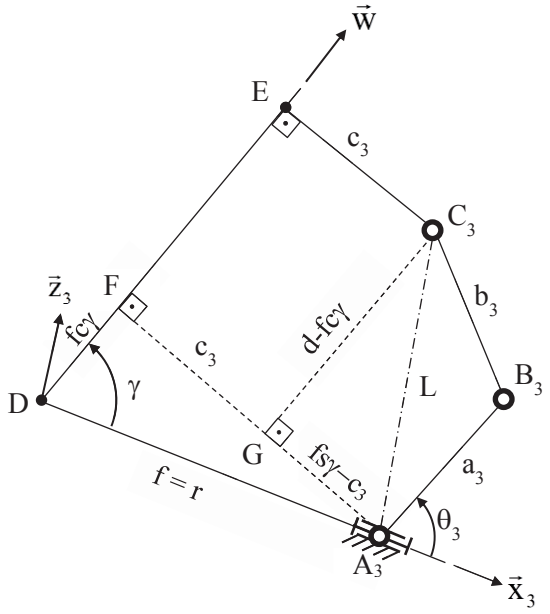

Figure 4.4 Dimension of the slider-crank mechanism

For the initial slider displacement, the distance between the center of mass (CoM) and the tip of the endoscope (Karl Storz, H3-Z Camera Head and 28731BWA Hopkins telescope) is taken as a reference value (Figure 4.5).

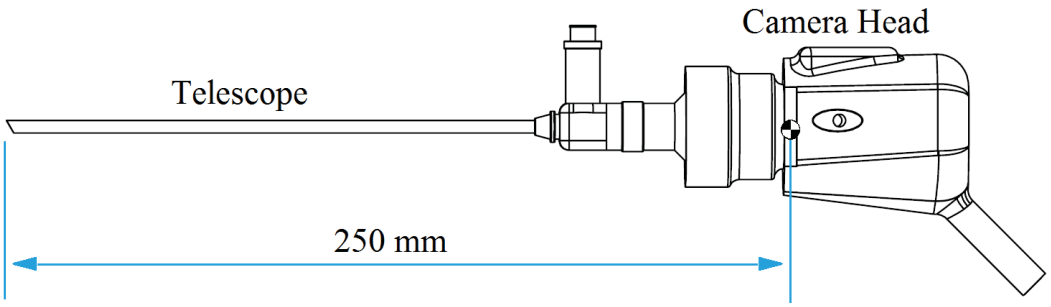

Figure 4.5. Distance from the CoM to the tip of Karl Storz™ Endoscope

As depicted in Figure 4.4, for the slider-crank mechanism,

- Eccentricity $|A_3G|$: $f\sin\gamma - c_3$
- Initial slider displacement: $d_0 = 250$ mm
- Stroke: $\Delta d = 100$ mm
- Effective workspace limits (at the end of the stroke): $\pm\Delta d_e = 20$ mm
- Zero position at the center of the workspace: $d = d_0 - \Delta d + \Delta d_e = 170$ mm

To satisfy the workspace limits $\Delta d = 100$ mm and $\Delta\gamma = 40°$: $\gamma_{min} = 70° \le \gamma \le 110° = \gamma_{max}$. The following limiting conditions on the link lengths in the limit configurations need to be taken into consideration:

$$b_3 + a_3 \ge \sqrt{\left(fs\gamma_{max} - c_3\right)^2 + \left(d_0 - fc\gamma_{max}\right)^2} = L_{max} \tag{4.55}$$

$$b_3 - a_3 \le \sqrt{\left(fs\gamma_{min} - c_3\right)^2 + \left(d_0 - \Delta d - fc\gamma_{min}\right)^2} = L_{min} \tag{4.56}$$

From (4.55) and (4.56),

$$a_3 \ge \frac{L_{max} - L_{min}}{2} \tag{4.57}$$

$$a_3 + L_{min} \geq b_3 \geq L_{max} - a_3 \tag{4.58}$$

The formulations are implemented in Microsoft Excel and the slider-crank mechanism is simulated. On the left side of Figure 4.6, design parameters and conditions are listed. After specifying a_3 and b_3 values, γ angle and d values can be changed with corresponding spin buttons to compute the transmission angle μ of the slider-crank mechanism. In Figure 4.6, for a_3 =135 mm and b_3 =195 mm, the worst transmission angle value is obtained as $\mu_{min} \cong 46.2°$ for $\gamma = 88°$ and d = 150 mm. Finally, all the kinematic formulations are crosschecked by a study in Microsoft Excel before starting the constructional design (Figure 4.7).

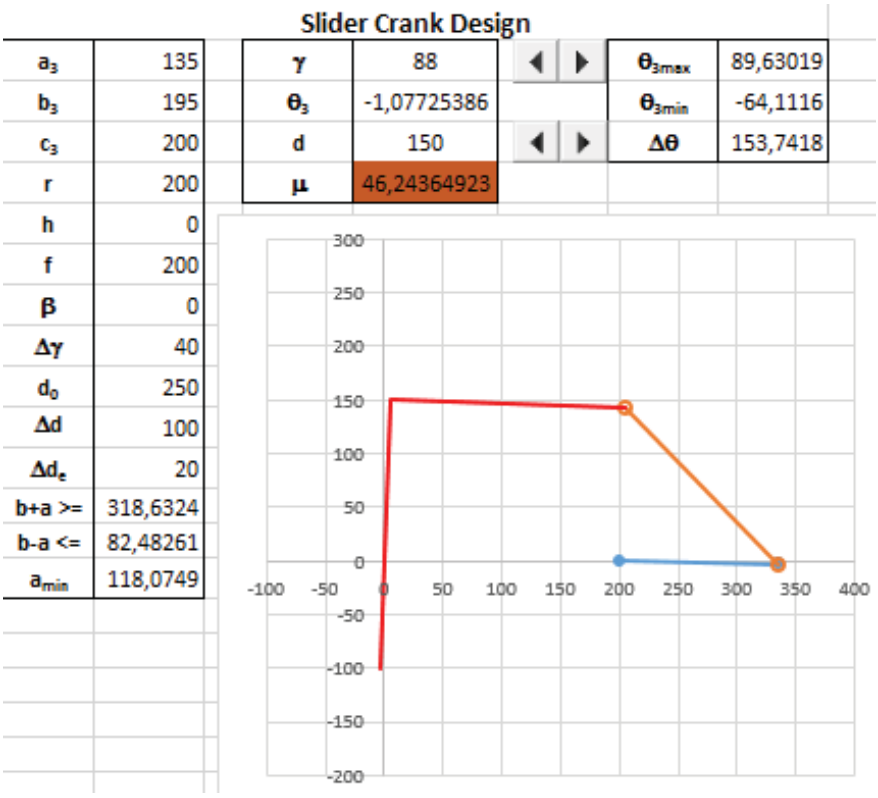

Figure 4.6 Slider-crank design study in Microsoft Excel

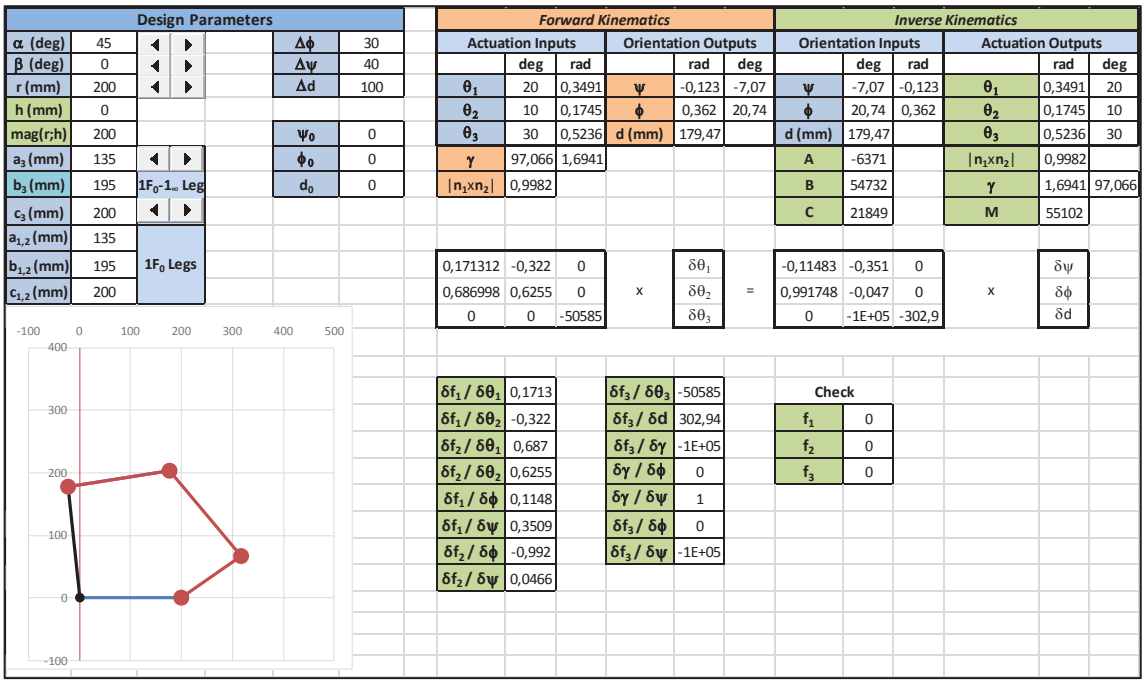

Design Parameters				
α (deg)	45	Δϕ	30	
β (deg)	0	Δψ	40	
r (mm)	200	Δd	100	
h (mm)	0			
mag(r;h)	200	ψ_0	0	
a_3 (mm)	135	ϕ_0	0	
b_3 (mm)	195	d_0	0	
c_3 (mm)	200			
$a_{1,2}$ (mm)	135			
$b_{1,2}$ (mm)	195			
$c_{1,2}$ (mm)	200			

1F0-1∞ Leg

1F0 Legs

Forward Kinematics						
Actuation Inputs			Orientation Outputs			
	deg	rad		rad	deg	
θ_1	20	0,3491	ψ	-0,123	-7,07	
θ_2	10	0,1745	ϕ	0,362	20,74	
θ_3	30	0,5236	d (mm)	179,47		
γ	97,066	1,6941				
$\lvert n_1 x n_2 \rvert$	0,9982					

0,171312	-0,322	0		$\delta\theta_1$	
0,686998	0,6255	0	x	$\delta\theta_2$	=
0	0	-50585		$\delta\theta_3$	

-0,11483	-0,351	0		$\delta\psi$	
0,991748	-0,047	0	x	$\delta\phi$	
0	-1E+05	-302,9		δd	

Inverse Kinematics						
Orientation Inputs			Actuation Outputs			
	deg	rad		rad	deg	
ψ	-7,07	-0,123	θ_1	0,3491	20	
ϕ	20,74	0,362	θ_2	0,1745	10	
d (mm)	179,47		θ_3	0,5236	30	
A	-6371		$\lvert n_1 x n_2 \rvert$	0,9982		
B	54732		γ	1,6941	97,066	
C	21849		M	55102		

$\delta f_1 / \delta\theta_1$	0,1713	$\delta f_3 / \delta\theta_3$	-50585
$\delta f_1 / \delta\theta_2$	-0,322	$\delta f_3 / \delta d$	302,94
$\delta f_2 / \delta\theta_1$	0,687	$\delta f_3 / \delta\gamma$	-1E+05
$\delta f_2 / \delta\theta_2$	0,6255	$\delta\gamma / \delta\phi$	0
$\delta f_1 / \delta\phi$	0,1148	$\delta\gamma / \delta\psi$	1
$\delta f_1 / \delta\psi$	0,3509	$\delta f_3 / \delta\phi$	0
$\delta f_2 / \delta\phi$	-0,992	$\delta f_3 / \delta\psi$	-1E+05
$\delta f_2 / \delta\psi$	0,0466		

Check	
f_1	0
f_2	0
f_3	0

Figure 4.7 Kinematic analysis study in Microsoft Excel

CHAPTER 5

CONSTRUCTIONAL DESIGN AND BALANCING

This chapter gives information about the constructional design, the static balancing, the manufacturing and the testing of the manipulator.

5.1 Constructional Design

Four subsystems are considered: base group, middle leg group, side leg group and platform group (Figure 5.1). Each group is explained in detail in the following sections.

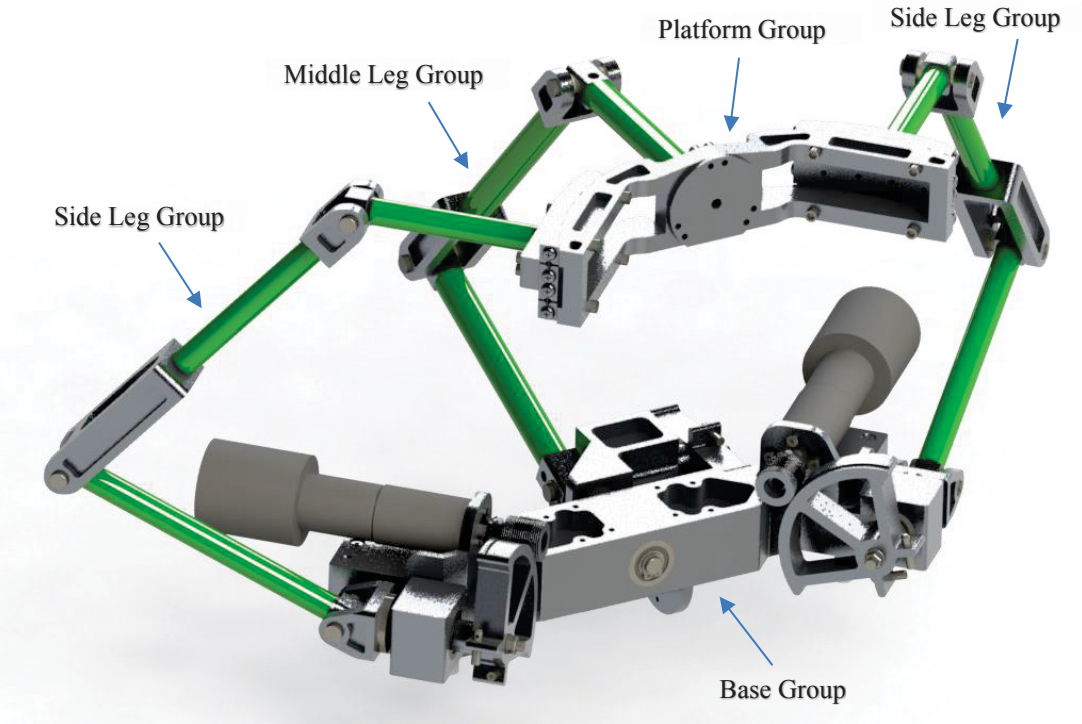

Figure 5.1. Constructional design of the system

5.1.1 Base Group

Base group carries two of the motors and is connected to the platform via leg groups. As depicted in Figure 5.2, it consists of a base, two motors and their motor holders, six roller bearings and two capstan pinions which are attached to the shaft of the motors by M3 setscrews. In each hole for the roller bearings in the base part, there are two roller bearings placed in two ends of the hole to get a better bearing for the shaft. Besides, self-aligning type bearings are selected to prevent any eccentricity between the rotation axes of two roller bearing facing each other.

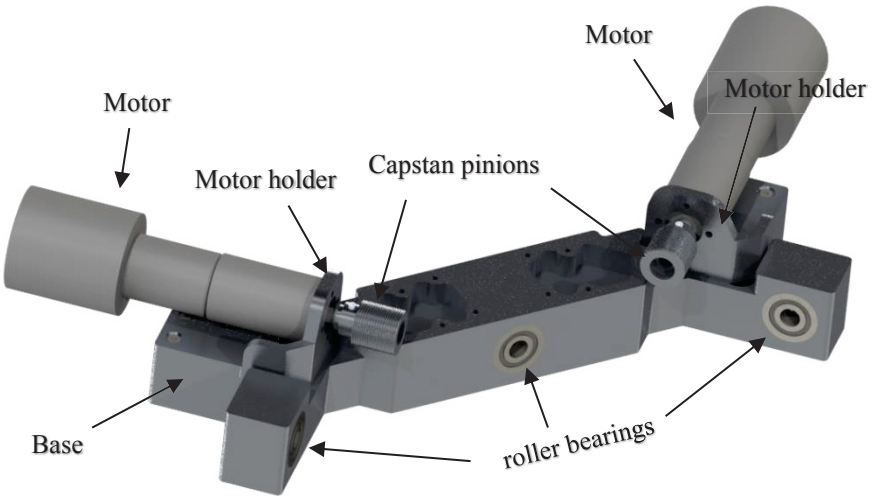

Figure 5.2. Assembly of the base group

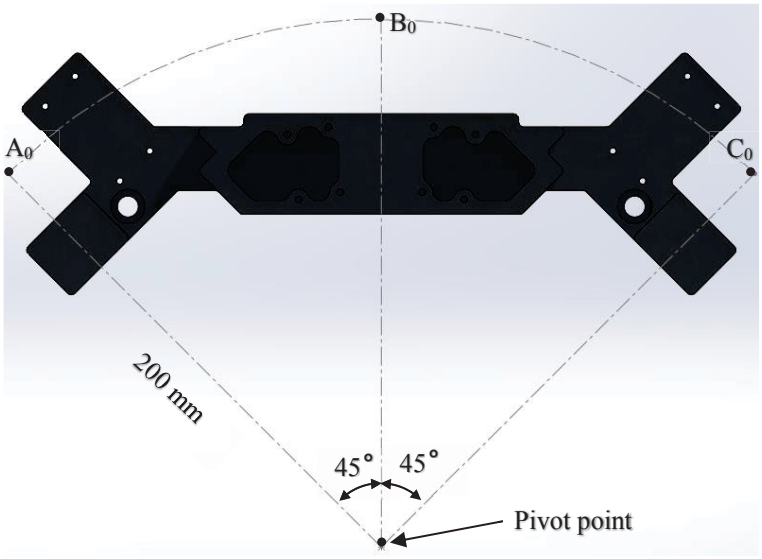

Figure 5.3. Top view of the base part

In the design of the base part in Figure 5.3, the key point is that the axes of the three roller bearings have to intersect at the pivot point with 45° angles in between them.

Based on simulations performed by other teams in the Neuroboscope project for an approximate CAD model with external forces, the maximum torque and the maximum speed on the steel shafts passing through the roller bearings in the base part is determined as 6 N·m and 10 rpm, respectively. So, these values were taken as the reference torque and speed requirements to select appropriate motors and gearheads for the mechanism. Also, due to the space constraints in the mechanism, the ratio for the capstan drive is determined as 1:5.

The motors to be used in the mechanism are relatively small motors and they need to have brakes. However, there are not many small motor options with brakes in the market. So, the smallest motors with brakes and appropriate gearheads satisfying the torque and speed requirements are investigated in the website of Maxon Motors. As a result, Maxon RE25 - 339155 motor (with a nominal torque of 27,5 mNm and a nominal speed of 8310 rpm) and Maxon Planetary Gearhead GP 26A, 406771 (with a gear ratio of 1:181) are chosen for the three of the motors. Thus, with a total reduction (gearhead ratio × capstan ratio) of 1:905, the nominal torque and the nominal speed for the steel shafts are obtained as 25 N·m and 9 rpm and they satisfy the requirements. The characteristic curve of the selected motor can be found in Figure 5.4.

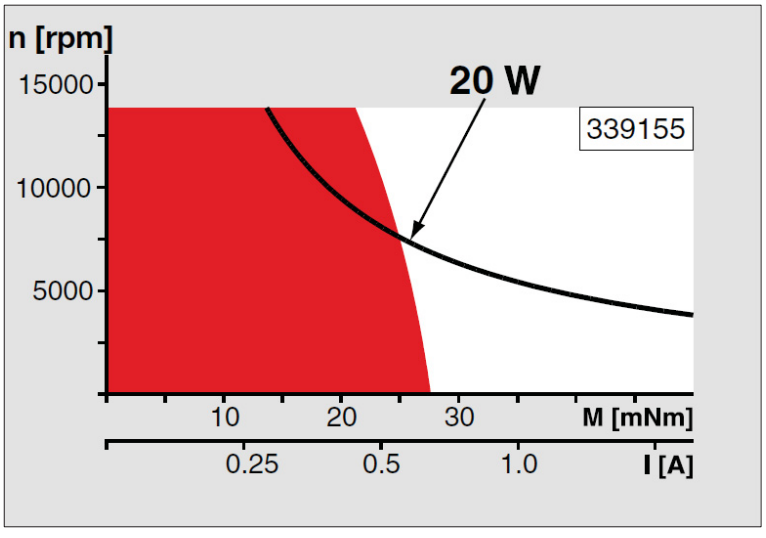

Figure 5.4. The characteristic curve of Maxon RE25 - 339155 motor
(Source: Maxon Motor, 2018)

5.1.2 Middle Leg Group

The middle leg group is the central leg system that is rigidly connected to the platform group with the distal link of the leg. Since the revolute joint at B_0 in Figure 5.5 needs to be actuated, the motor is attached to the middle leg with a capstan system called as central capstan system. As depicted in Figure 5.6, two standard 2x2x10 mm keys are used for connecting the capstan disc rigidly to the 8 mm diameter steel shaft. Also, M8 snap rings and M4 nuts are used to keep parts in their places.

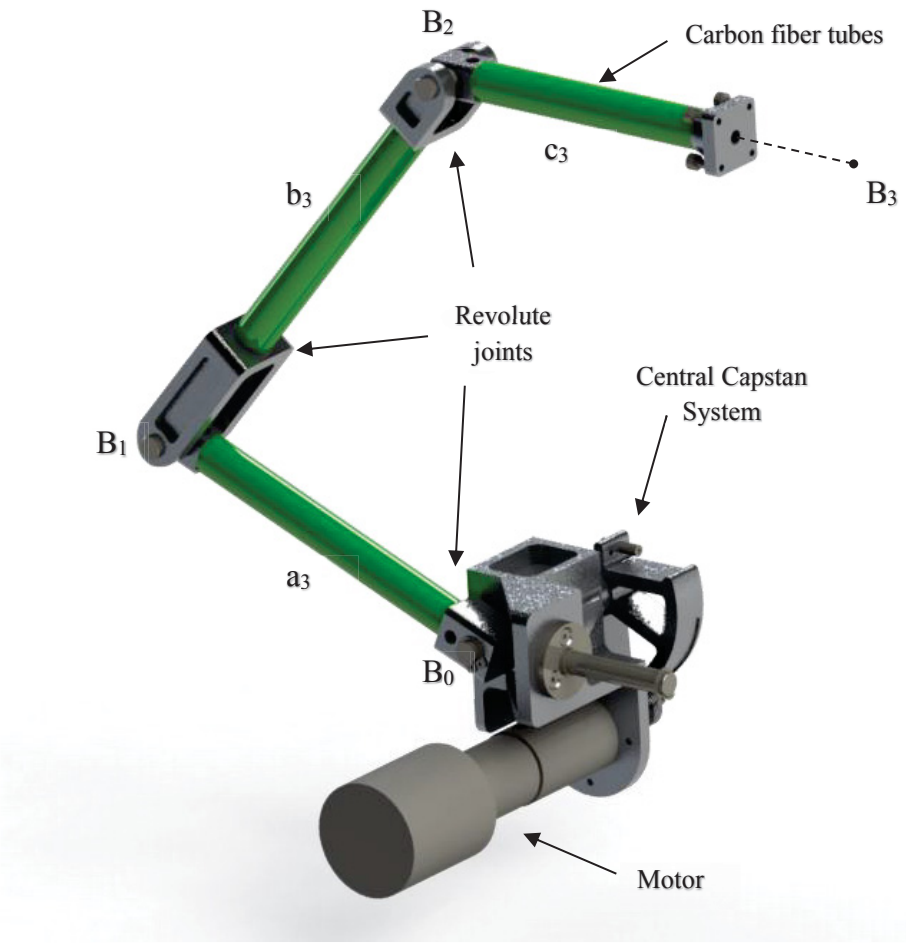

Figure 5.5. Assembly of the middle leg group

For the links in the middle leg group, carbon fiber tubes with a diameter of 14 mm are used in order to reduce the weight of the links while for the side leg groups, 12 mm carbon tubes are used. Diameter of the tubes in the middle leg group is bigger than the

ones in the side leg groups due to the cables going through all the links from the platform to the base for the sensors in the endoscope group connected to the platform part.

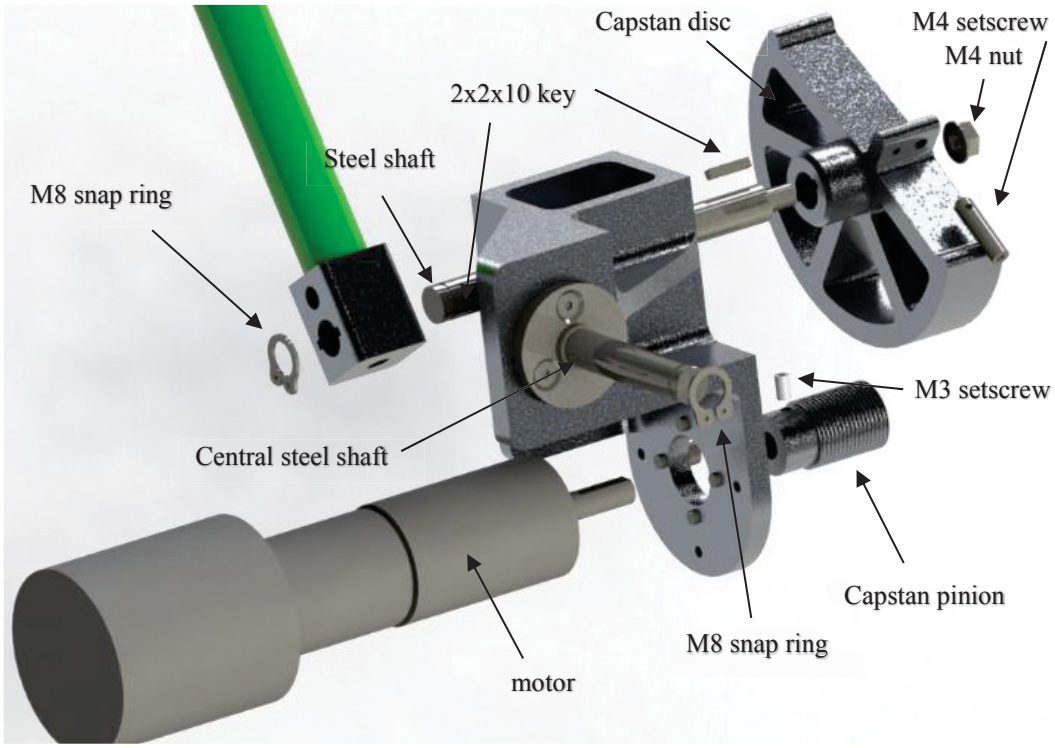

Figure 5.6. Exploded view of the central capstan system

Except the first and last revolute joints in the middle and side leg groups, all revolute joints are constructed as illustrated in Figure 5.7. In these joints, instead of using roller bearings, nylon bushes are used to have joints with more friction for the ease of control of the system. Also, these bushes have flanges to prevent wears between aluminum joint parts.

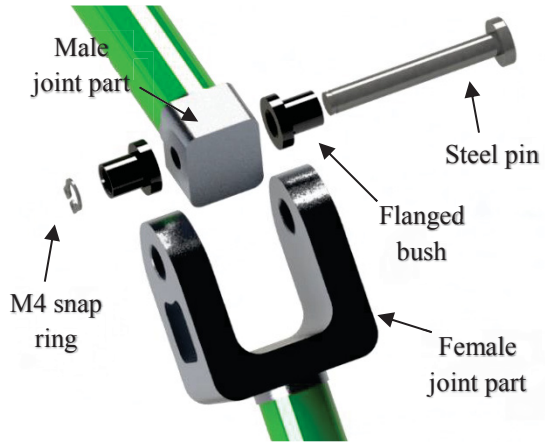

Figure 5.7. Revolute joint assembly

For the central capstan system, firstly, radii of capstan disc and capstan pinion are calculated by using (5.1). Then, they are constructed according to the calculated and tabulated dimension in Table 5.1.

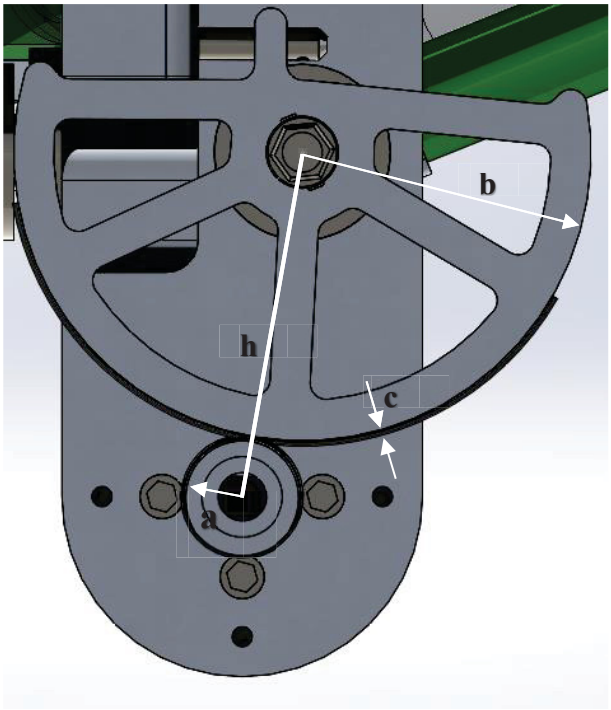

Figure 5.8. Dimensions of the central capstan system

$$h = a + b + \frac{c}{2} \quad \text{and} \quad b = 5a + \frac{c}{2} \quad \Rightarrow \quad a = \frac{h}{6} \tag{5.1}$$

Table 5.1. Calculations for central capstan system

Distance, h (mm)	43,65
Rope diameter, c (mm)	0,7
Capstan ratio	5

	Radius (mm)
Capstan pinion, a	7,27
Capstan disc, b	36,02

For the design of the central steel shaft, the worst operation conditions are evaluated for the middle leg group. The maximum bending moment applied on the central shaft is obtained when $\psi = 20°$. In that case, the information about the CoM of the middle

leg and the endoscope group is given in Figure 5.9. According to these values, the strength calculations can be done for 8 mm diameter AISI 1050 steel in hand.

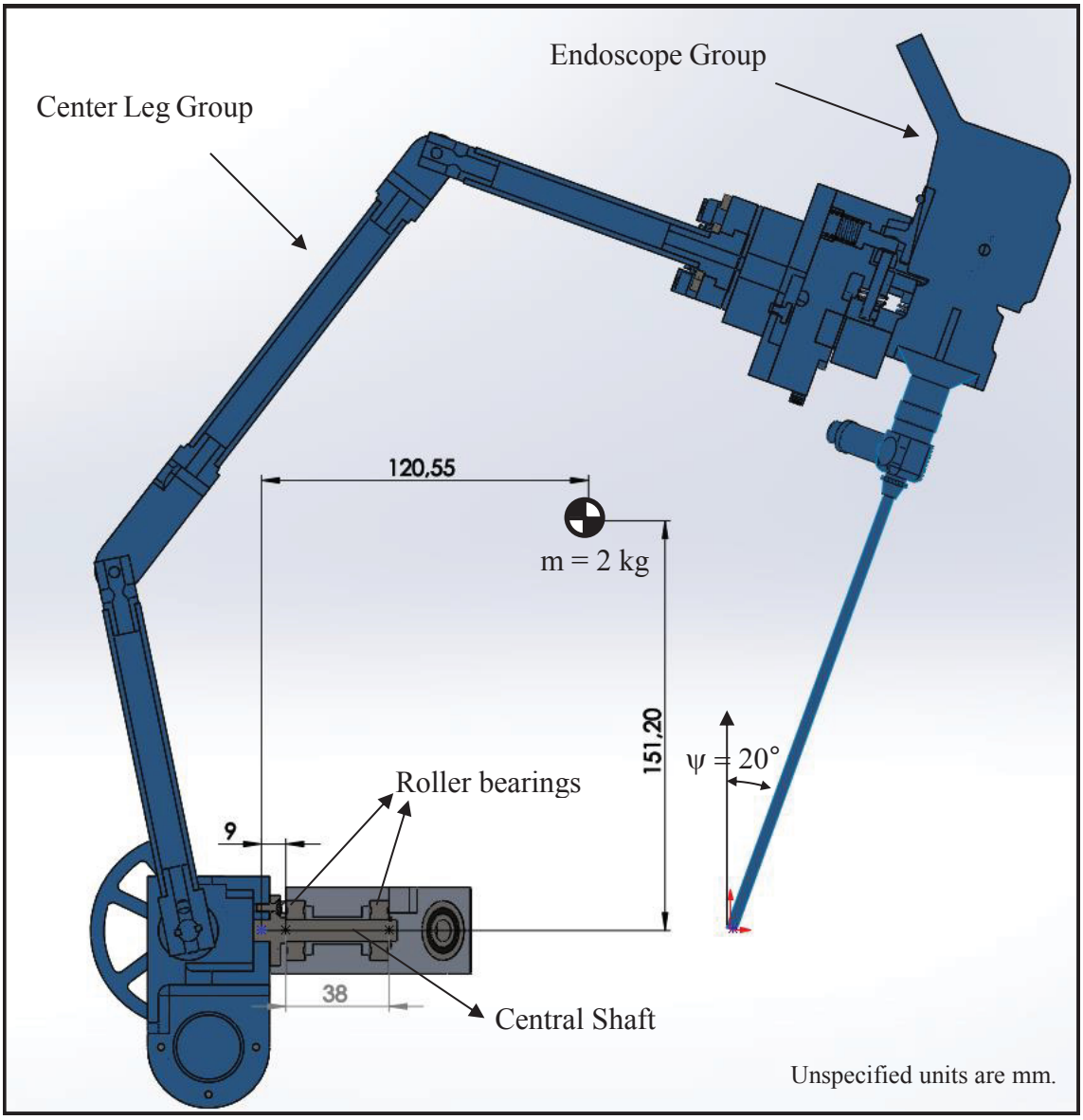

Figure 5.9 Dimensions for the CoM of the middle leg group and the endoscope group

By using the mass and the dimension values in Figure 5.9, the load and moment on point O can be found as 2 kg × 9,81 m/s^2 = 19,62 N and 19,62 N × 120,55 mm = 2,36 N·m respectively. First, reaction forces are calculated and then shear-moment diagrams are drawn (Figure 5.10).

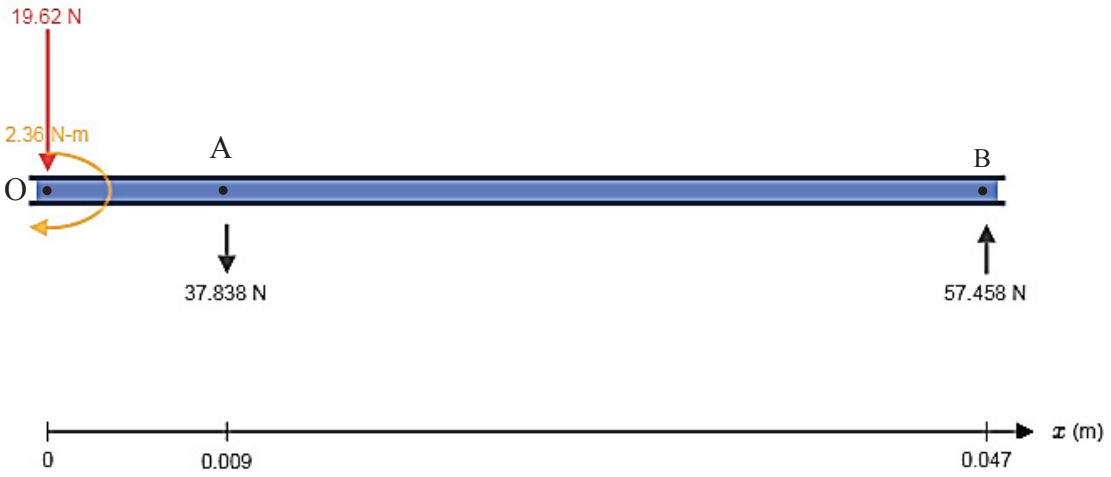

Figure 5.10 Free-body diagram of the central steel shaft

In the shear-moment diagrams in Figure 5.11, it is seen that maximum bending moment of 2,36 N·m occurs at x = 0 mm and the maximum shear force of 57,46 N occurs at x = 9 mm. These two maximum values can be used together just for the sake of safety to find the worst-case combined load.

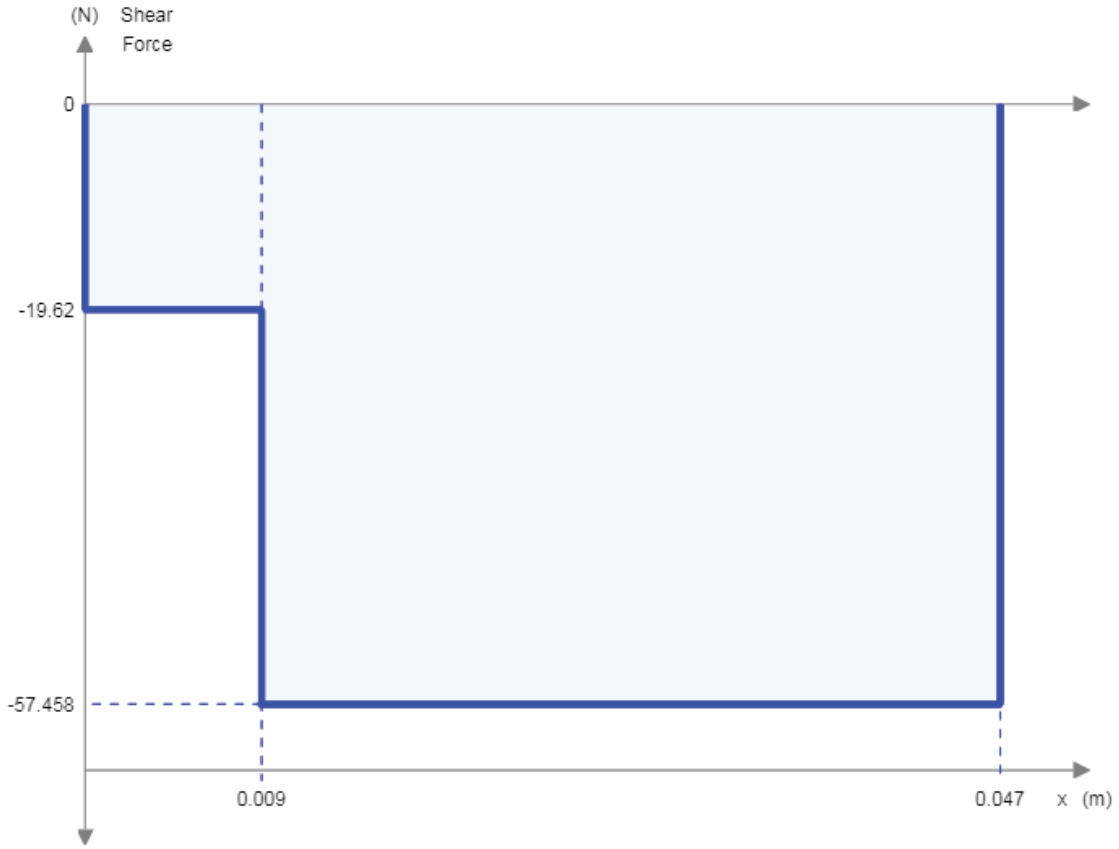

Figure 5.11 Shear force and bending moment diagrams **(Continued on next page)**

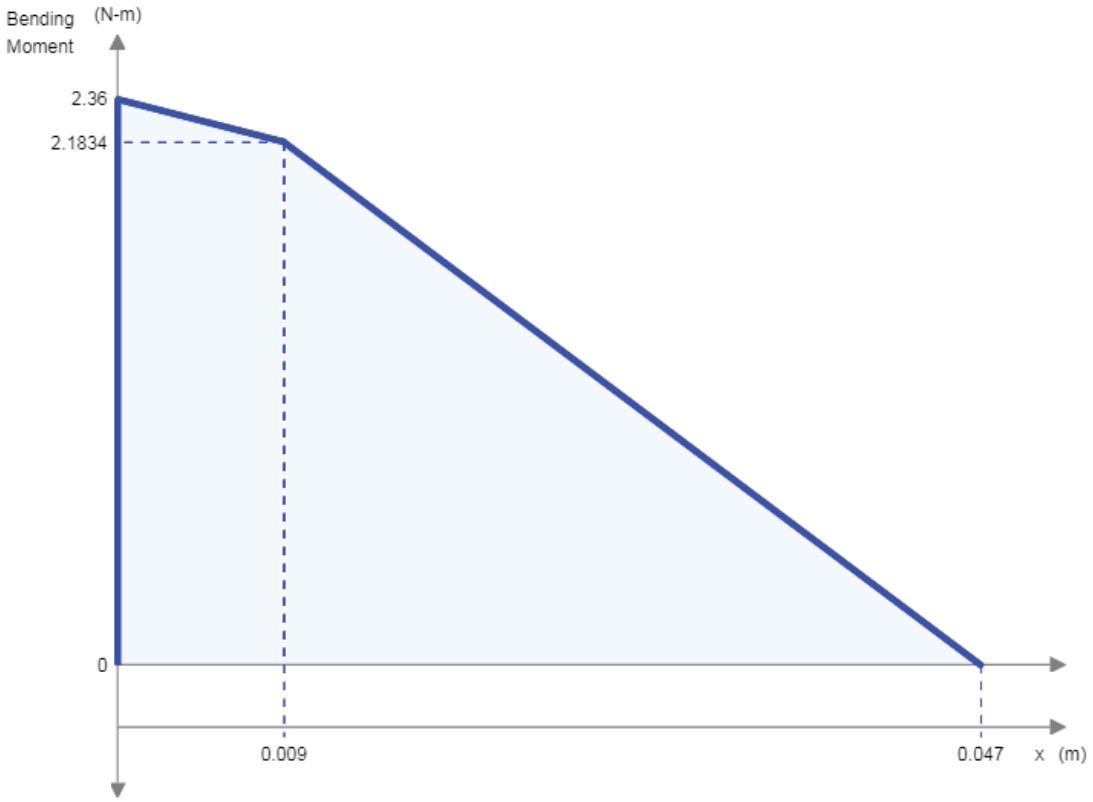

Figure 5.11 **(Continued)**

For V = 57,46 N, M = 2,36 N·m, r = 4 mm and yield strength σ_{yield} for AISI 1050 steel = 580 MPa

$$\sigma_{combined} = \sigma_{shear} + \sigma_{bending} \tag{5.2}$$

$$= \frac{4V}{3A} + \frac{Mr}{I} = \frac{4V}{3\pi r^2} + \frac{4M}{\pi r^3} \tag{5.3}$$

$$= 48 \text{ MPa} \quad < \quad \sigma_{yield} = 580 \text{ MPa} \tag{5.4}$$

As a result, 1050 carbon steel with 8 mm diameter is quite safe to be used as a central shaft for the mechanism. For ease of manufacturing and for the consistency in machine elements to be used in the mechanism, all the shafts in the base link and the capstan shaft of the middle leg are selected from the same material with the same diameter.

5.1.3 Side Leg Group

In the system, the left side leg and right side leg are identical (Figure 5.12). The side legs are connected to the platform group via slide ways, which will be explained in detail in Section 5.1.4. Also, for the link b_1 (or b_2), the bottom female joint part is designed longer than the upper one in order to prevent any collision with link a_1 (or a_2) throughout the workspace of the mechanism.

The exploded view of the lateral capstan system is available in Figure 5.13. The same machine elements used for the lateral capstan discs are used. Similarly, radii of capstan disc and capstan pinion are calculated using (5.1) and the parameters depicted in Figure 5.14 and Table 5.2.

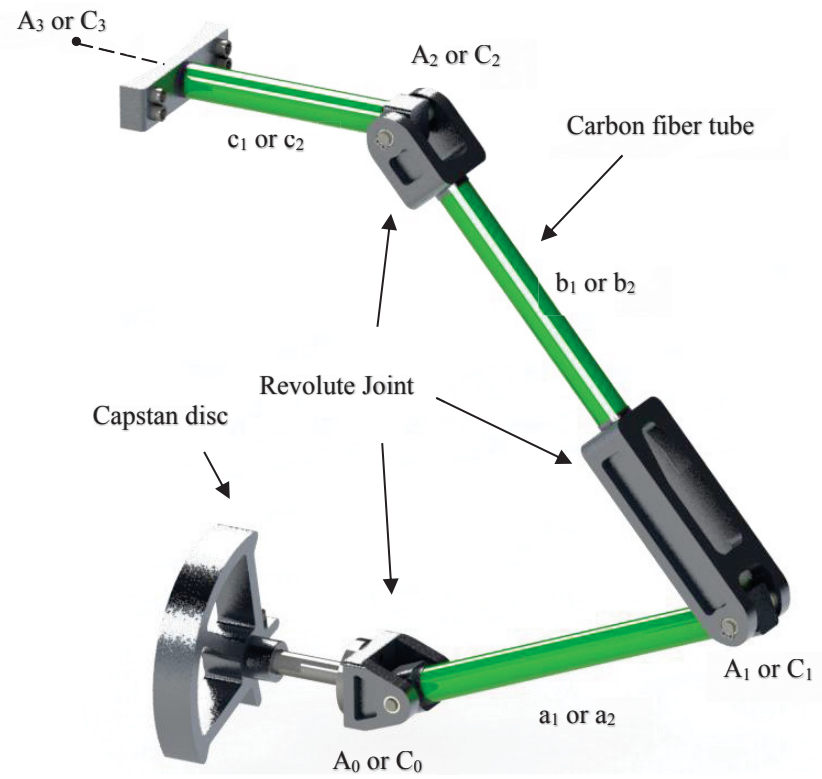

Figure 5.12. Assembly of side leg group

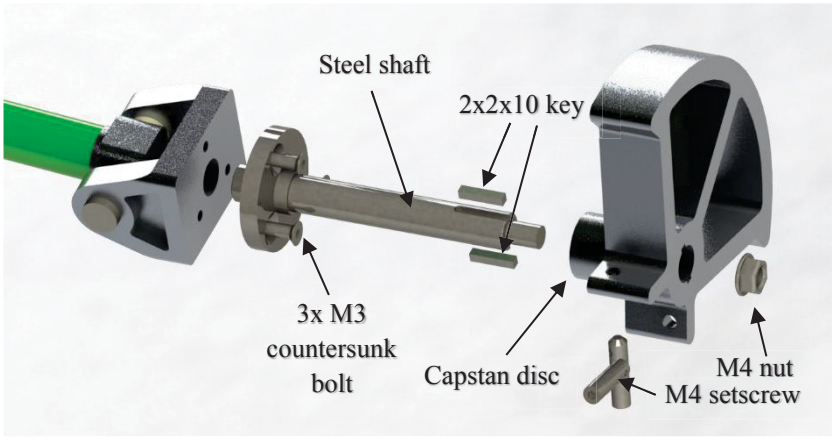

Figure 5.13. Exploded view of the lateral capstan system

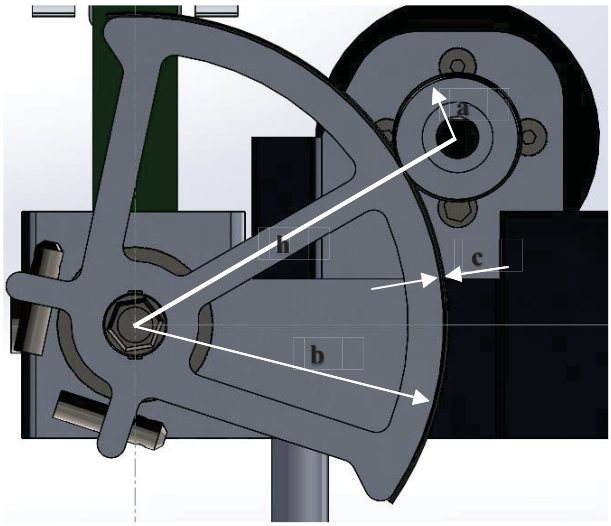

Figure 5.14. Dimensions of the lateral capstan system

Table 5.2. Calculations for lateral capstan system

Distance, h (mm)	52,67
Rope diameter, c (mm)	0,7
Capstan ratio	5

	radius (mm)
Capstan pinion, a	8,72
Capstan disc, b	43,60

5.1.4 Platform Group

In the platform group, there are three different sub parts: endoscope platform, sliding bearings and the endoscope (Figure 5.15). The design of the endoscope group is not in the scope of this thesis. While the side legs are connected to this group with a revolute joint, the middle leg group is rigidly connected to the platform part through the leg's distal link.

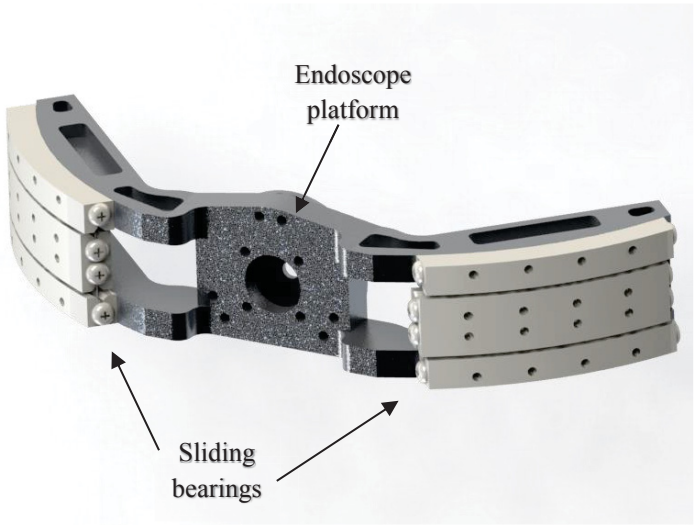

Figure 5.15. Assembly of the platform group

For the revolute joints whose center of rotations coincide with the end-effector axis, Gonio Way RV type slide ways of Nippon Bearing Company are used. These curved slide ways are used to construct a low-friction rotary motion bearing. Two sets of RV3070-110-10Z model are used in the constructional design.

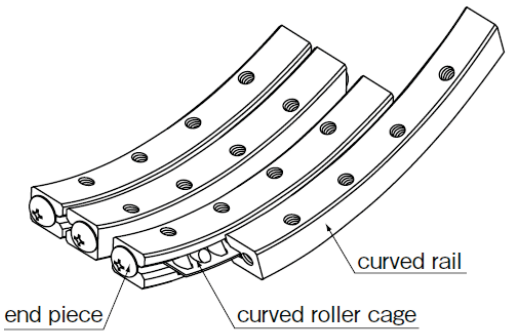

Figure 5.16. Structure of a set of RV3070-110-10Z of Gonio Way
(Source: Nippon Bearing, 2018)

5.2 Static Balancing

In this Section, the static balancing of the active arm with counter-masses and springs is performed. Firstly, the case in which only counter-masses are used for static balancing is investigated. The masses of the links are neglected and the payload comprising the platform and the endoscope groups are equally distributed to the three legs and the distributed masses are lumped at the end of the distal link in each leg.

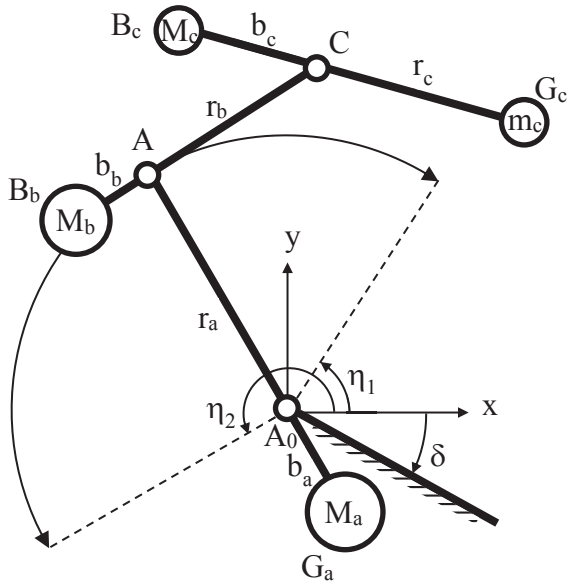

Figure 5.17 Diagram for mass balancing

In Figure 5.17, a diagram for balancing of one of the legs in the mechanism is given. The payload for the mechanism is m_c, which is one-third of the mass of the platform and endoscope group. M_a, M_b and M_c are the counter-masses and b_a, b_b and b_c are their extension lengths from the joints A_0, A and C, respectively. Parameters r_a, r_b and r_c are the link lengths. δ is the angle of the base of the mechanism with respect to the ground horizontal level. η_1 and η_2 are the angle limits for the proximal link of the leg. The payload of the mechanism is 12 kg in total. So, for a leg, m_c = 400 gr. Also, η_1 = 57,2° and η_2 = 209,7° are calculated from the kinematic design. By using the following equations, the counter-masses can be found:

$$M_c b_c = m_c r_c \quad \Rightarrow \quad M_c = \frac{m_c r_c}{b_c} \tag{5.5}$$

$$M_b b_b = (m_c + M_c) r_b \quad \Rightarrow \quad M_b = \frac{(m_c + M_c) r_b}{b_b} \tag{5.6}$$

$$M_a b_a = (m_c + M_c + M_b) r_a \quad \Rightarrow \quad M_a = \frac{(m_c + M_c + M_b) r_a}{b_a} \tag{5.7}$$

Counter-mass distances b_a, b_b, b_c are selected considering link collusions and the footprint of the mechanism. The link parameters are set according to the kinematic design and the counter-masses are calculated (Figure 5.18).

Link	Length (mm)	Extension	Length (mm)	Link	Mass (gr)
r_a	135	b_a	100	M_a	3712,5
r_b	195	b_b	80	M_b	1950
r_c	200	b_c	200	M_c	400
				m_c	400
			for one leg	m_{total}	6462,5
			for three legs	M_{total}	**19387,5**

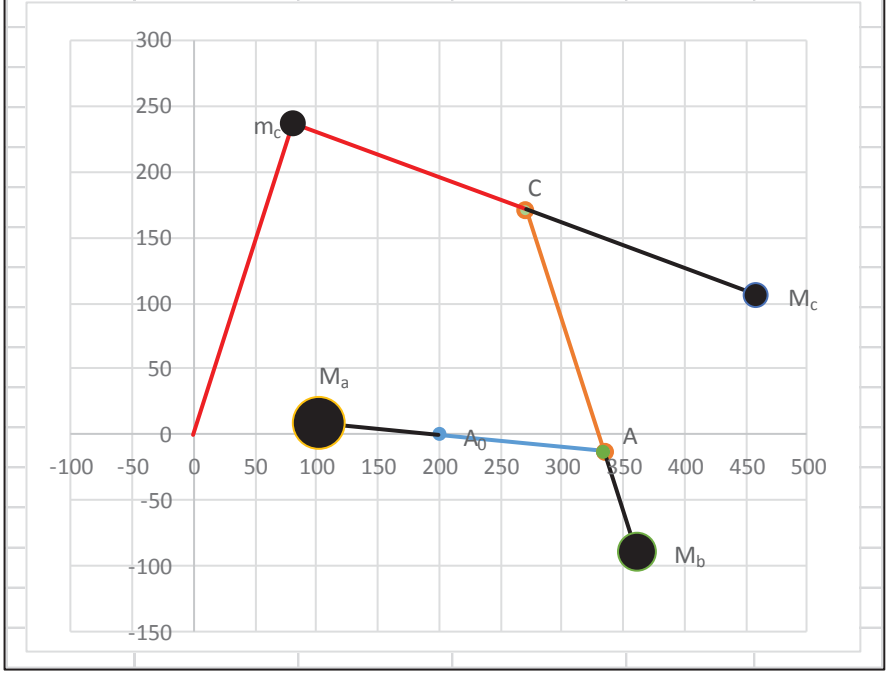

Figure 5.18 Mass balancing study

As a result of this study, even though the masses of the links are neglected, approximately 19 kg additional mass in total is needed to balance 1,2 kg payload. A balancing with that amount of mass is not practical since the mechanism needs to be compact and lightweight. Also, due to the motion range of the proximal link, there may be some collisions with the manipulator's base. Therefore, a hybrid balancing option with counter-masses and springs is devised (Figure 5.19). Performing the whole balancing with springs is not feasible because the springs need a vertical reference frame and it is not practical to construct these frames for the distal links.

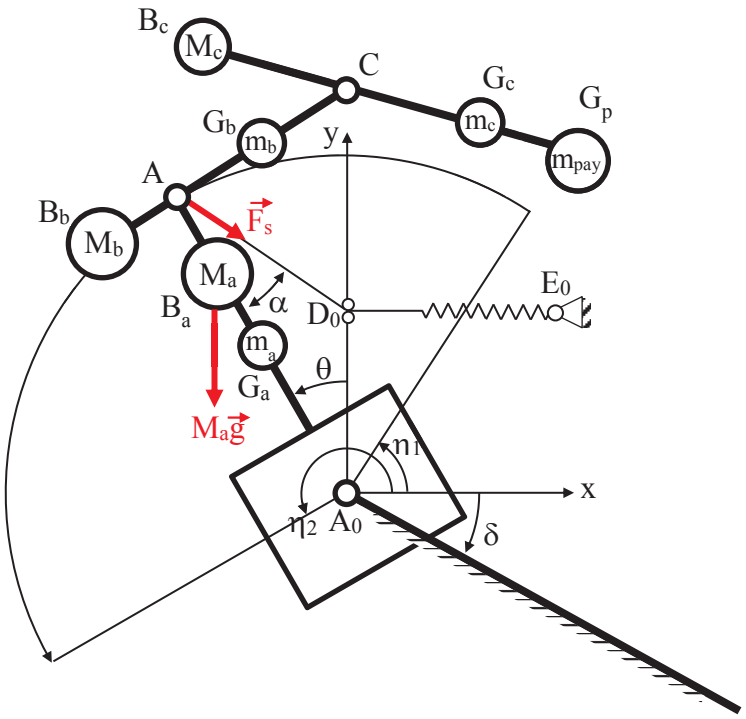

Figure 5.19. Diagram for mass and spring balancing

This time, the link masses are also taken into account. The counter-masses M_c and M_b are computed by formulations similar to (5.5) and (5.6), but also considering the link masses and locations. However the counter-mass M_a in Figure 5.17 is not the same mass as M_a in Figure 5.19. It is the total leg mass and $g_a^{eff}=|A_0B_a|$ is the total CoM location of the whole leg. Also, m_{pay} is the payload for a leg. Let $|A_0G_a| = g_a$, $|AG_b| = g_b$ and $|CG_c| = g_c$ denote the locations of the masses of links a, b and c. So,

$$M_a = m_a + m_b + m_c + m_{pay} + M_b + M_c \tag{5.8}$$

$$g_a^{eff} = \frac{(m_c + m_{pay} + M_c + M_b)r_a + m_a g_a}{M_a} \tag{5.9}$$

Let $|A_0D_0| = f$, where D_0 is one end of the spring attached on the vertical axis. Using sine theorem in triangle A_0AD_0:

$$\frac{f}{\sin\alpha} = \frac{|AD_0|}{\sin\theta} \quad \Rightarrow \quad |AD_0|\sin\alpha = f\sin\theta \tag{5.10}$$

Using (5.10) and moment equilibrium for M_a about A_0:

$$g_a^{eff} M_a g \sin\theta = r_a F_s \sin\alpha = r_a k |AD_0| \sin\alpha = r_a k f \sin\theta \tag{5.11}$$

$$\Rightarrow \quad kf = \frac{g_a^{eff} M_a g}{r_a} \tag{5.12}$$

where k is the spring constant. $|D_0E_0|$ length and length of the string attach to the spring depend on the free length l_0 of the spring and should be evaluated such that the spring is load-free when G_a is on the y-axis.

After these formulations, a numerical study is carried out in Microsoft Excel (Table 5.3). In this study, the values of the link masses and their distances to the proximal links are taken from CAD model. Most of the mass of the platform is carried by the distal link of the link 3. The remaining payload (endoscope group), m_{pay}^{tot} is distributed to legs in various ratios such that the same spring can be used for the whole legs. For f = 30 mm, a spring with k = 0,7753 N/mm is determined to be used for each leg. As a result, hybrid balancing method reduced the total mass approximately from 19 kg to 7 kg. When compared to mass balancing case, it is more practical to implement to the mechanism.

Table 5.3. Balancing study in Microsoft Excel

		gr		mm			mm		gr	f (mm)	k (N/mm)
Leg 1	m_{a1}	43,48	g_{a1}	79,49		g_{a1}^{eff}	133,99	M_{a1}	2388,91	30	0,7753
	m_{b1}	47,39	g_{b1}	117,79		b_{b1}	80	M_{b1}	1649,82		
	m_{c1}	63,21	g_{c1}	90,69		b_{c1}	200	M_{c1}	293,84		
	m_{pay1}	291,18	g_{pay1}	182,14							
	m_{c1}^{eff}	354,39	g_{c1}^{eff}	165,83							
Leg 2	m_{a2}	43,48	g_{a2}	79,49		g_{a2}^{eff}	133,99	M_{a2}	2388,91	30	0,7753
	m_{b2}	47,39	g_{b2}	117,79		b_{b2}	80	M_{b2}	1649,82		
	m_{c2}	63,21	g_{c2}	90,69		b_{c2}	200	M_{c2}	293,84		
	m_{pay2}	291,18	g_{pay2}	182,14							
	m_{c2}^{eff}	354,39	g_{c2}^{eff}	165,83							
Leg 3	m_{a3}	53	g_{a3}	69,08		g_{a3}^{eff}	133,54	M_{a3}	2396,96	30	0,7753
	m_{b3}	54,1	g_{b3}	112,74		b_{b3}	80	M_{b3}	1567,96		
	m_{c3}	314	g_{c3}	126,04		b_{c3}	200	M_{c3}	297,99		
	m_{pay3}	109,92	g_{pay3}	182,14							
	m_{c3}^{eff}	423,92	g_{c3}^{eff}	140,59				Total Mass (gr)	7174,8		
	m_{pay}^{tot}	692,27	g_{pay}	182,14		payload distribution ratios					
						Leg 1	Leg 2	Leg 3			
			r_a	135		0,4206	0,4206	0,1588			
			r_b	195							

Although the computations for counter-mass and spring balancing are performed, they are not implemented in the conceptual design and prototyping phase yet. The implementation of the balancing remains as a future work.

5.3 Prototyping

After the constructional design is completed, the prototyping phase began. First, CAM files for the CAD models of the parts to be manufactured in CNC machine were prepared using CREO software. Then, the parts are machined by using a lathe and a CNC milling machines.

The manufacturing process was started with the base part, which was the most challenging part to manufacture precisely. Since it has two angled faces having two roller bearings, it is hard to manufacture by using a regular 3-axes CNC machine. Considering the cost of machining with a 4- or 5-axes CNC, it was more preferable to use 3-axes CNC

machine with a rotary table. First, an aluminum block was clamped and contoured as in Figure 5.20. Then, the holes for the bolts are drilled.

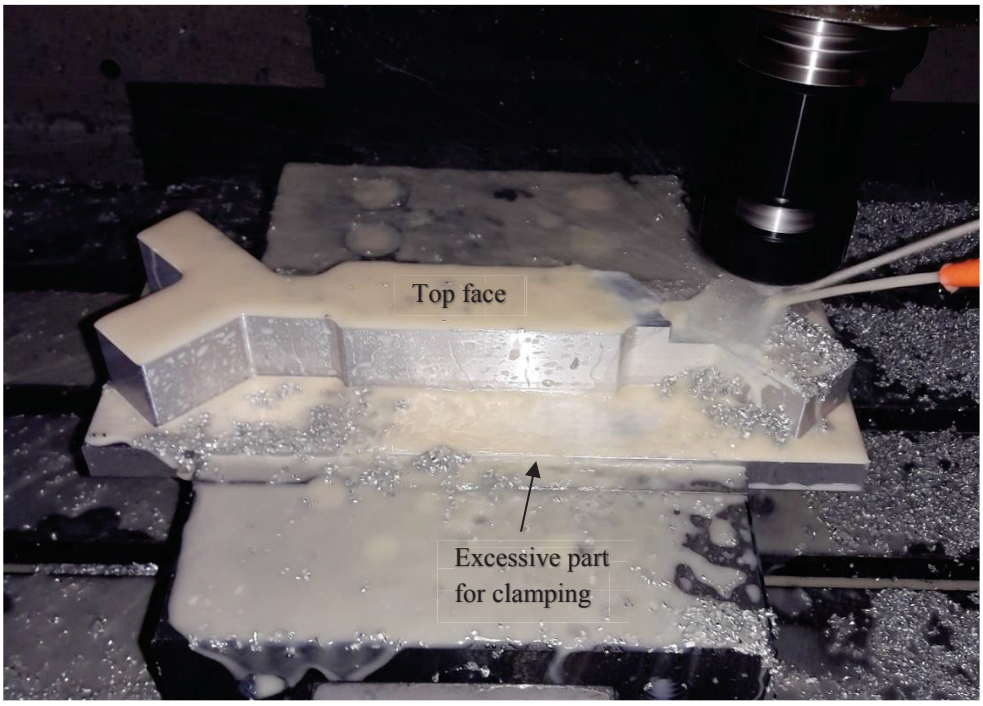

Figure 5.20. Contouring the base part from an aluminum block

After one side is completed, the part is clamped from the other side by using a fixture apparatus in order to remove the excessive part (Figure 5.21). For attaching the part to the apparatus, two temporary bolt holes and two temporary centering pin holes are drilled inside the lightening holes on the top face (Figure 5.24).

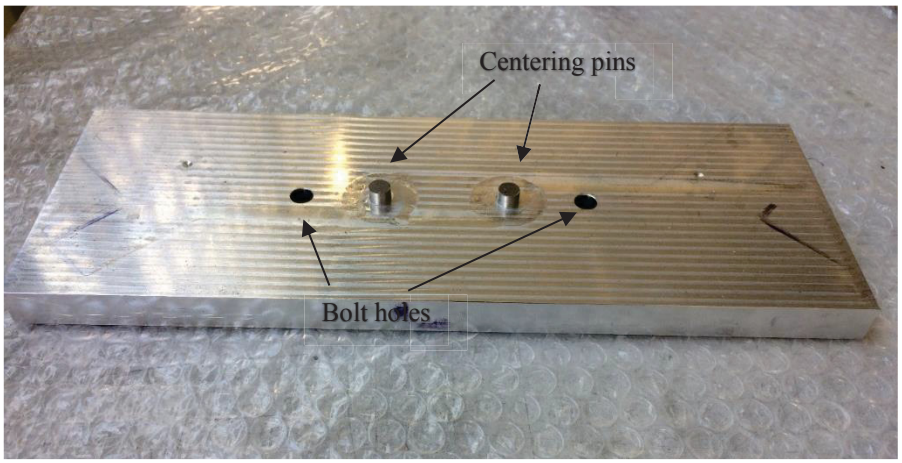

Figure 5.21 Fixture apparatus for the base part

For drilling the holes for roller bearings, the part is clamped on a rotary table and it is positioned horizontally by using a dial indicator (Figure 5.22). A dial indicator with 0,01 mm precision (Figure 5.23) is used by sliding its probe on the surface that is needed to be horizontal. If its indicator does not move, it means that the surface is horizontal with respect to the ground. Then, the holes are drilled. The manufactured base part is depicted in Figure 5.24.

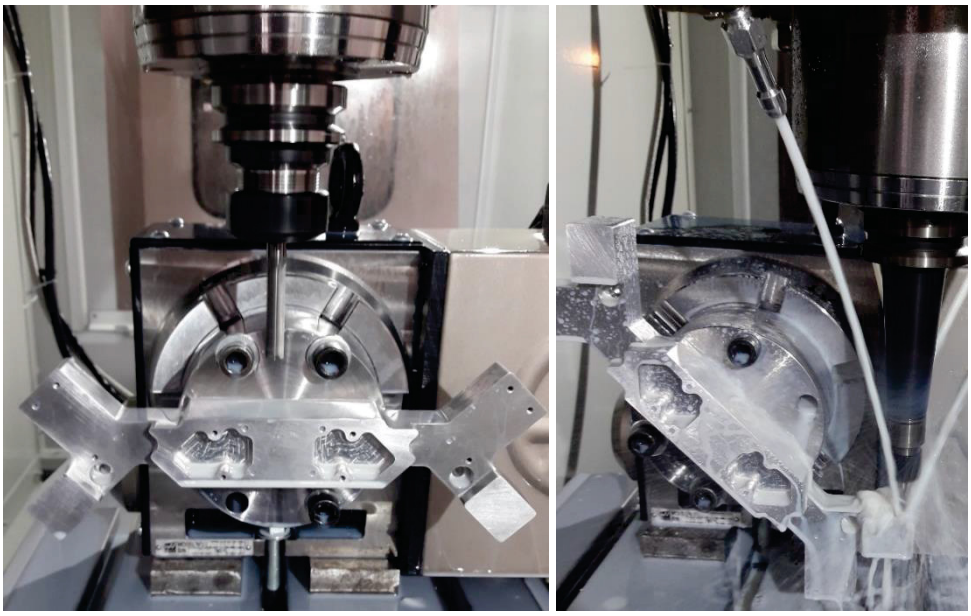

Figure 5.22 Using rotary table for drilling the holes of roller bearings

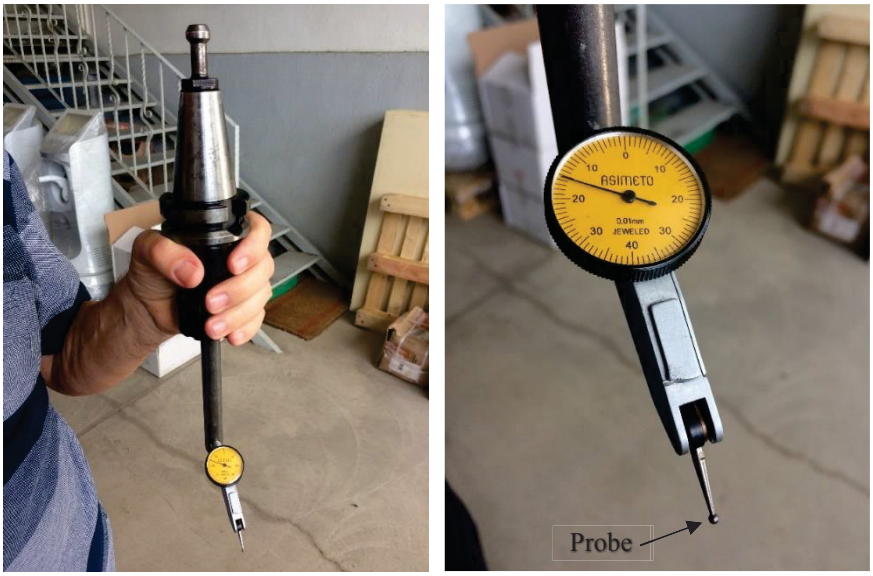

Figure 5.23 Dial indicator tool used along with the CNC milling machine

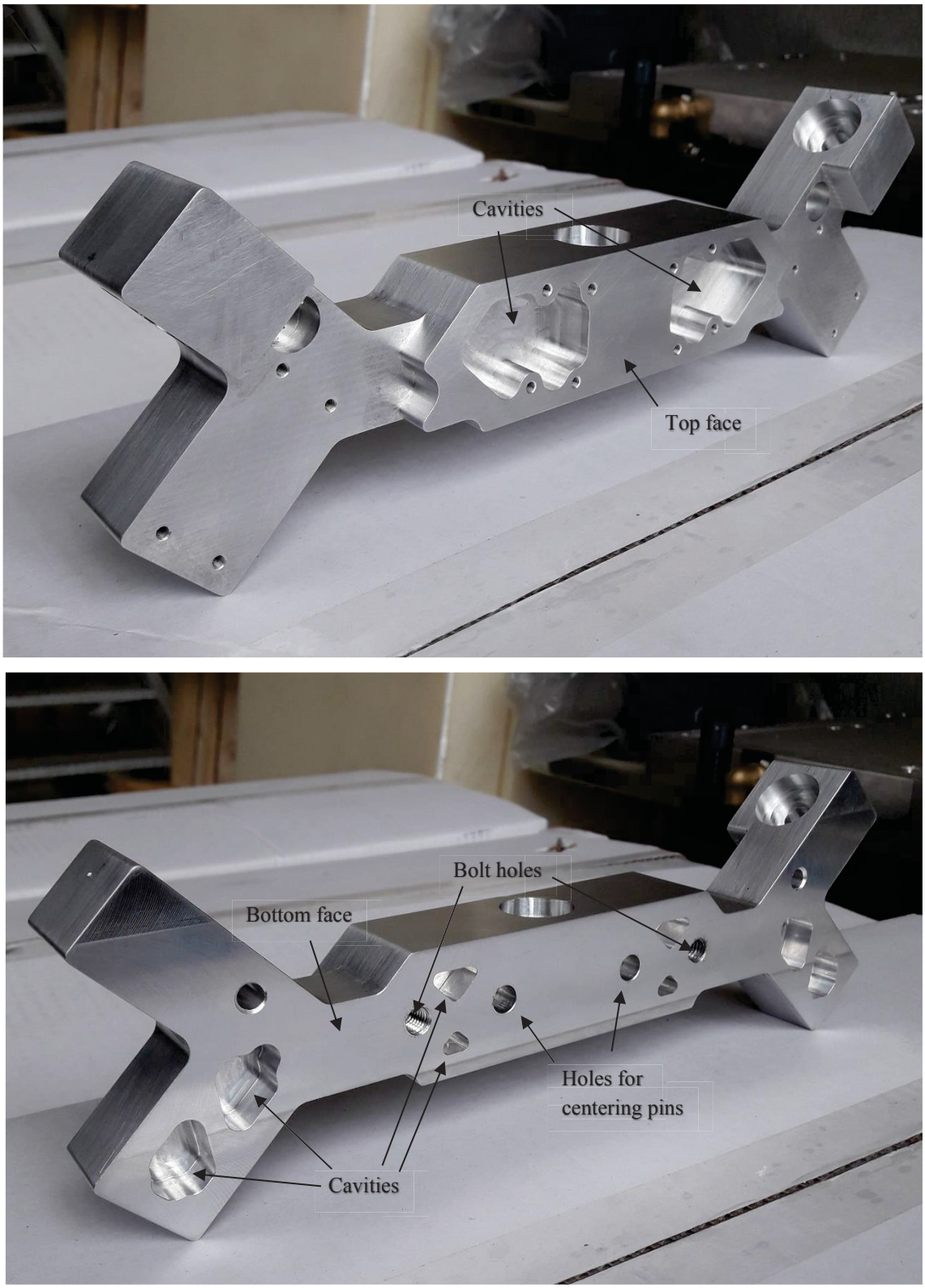

Figure 5.24 Two views of the manufactured base part

After the base part, the platform part were manufactured. Similar with the base part, an aluminum block was clamped and contoured. Then, the cavities are machined.

Finally, the clamped part was surface-finished and the cavities are machined on the other side by using the fixture apparatus in Figure 5.25.

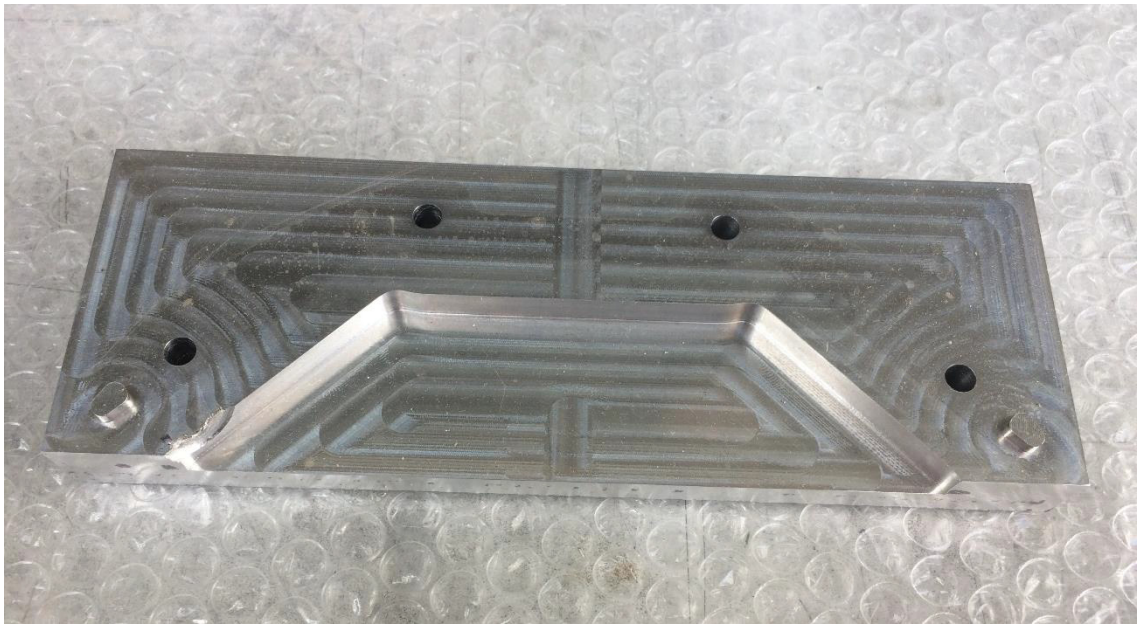

Figure 5.25 Fixture apparatus for the platform part

In the platform part, the tolerances of the holes for the slide ways are very critical in order to have smooth sliding in the slide ways. Since they are on the angled faces, it was hard drill them precisely. So, the part was clamped in a way that angled faces are parallel to the ground respectively as depicted in Figure 5.26. These faces were positioned horizontally with respect to the ground using a dial indicator. Then, the holes for slide ways and the other cavities are machined. As the last step, the part was clamped such that its front face is horizontal with respect to the ground. Then, the holes in that face are drilled and the manufacturing process of the platform is completed. Manufactured platform part can be seen in Figure 5.27 together with the two slide way groups.

The next part to be manufactured was the capstan disc parts. Similar with the previous parts, a fixture apparatus was manufactured to machine two faces of the parts. The fixture apparatus can be seen in Figure 5.28. The outer bolt holes are for the central capstan disc part while the inner ones for the lateral capstan disc parts.

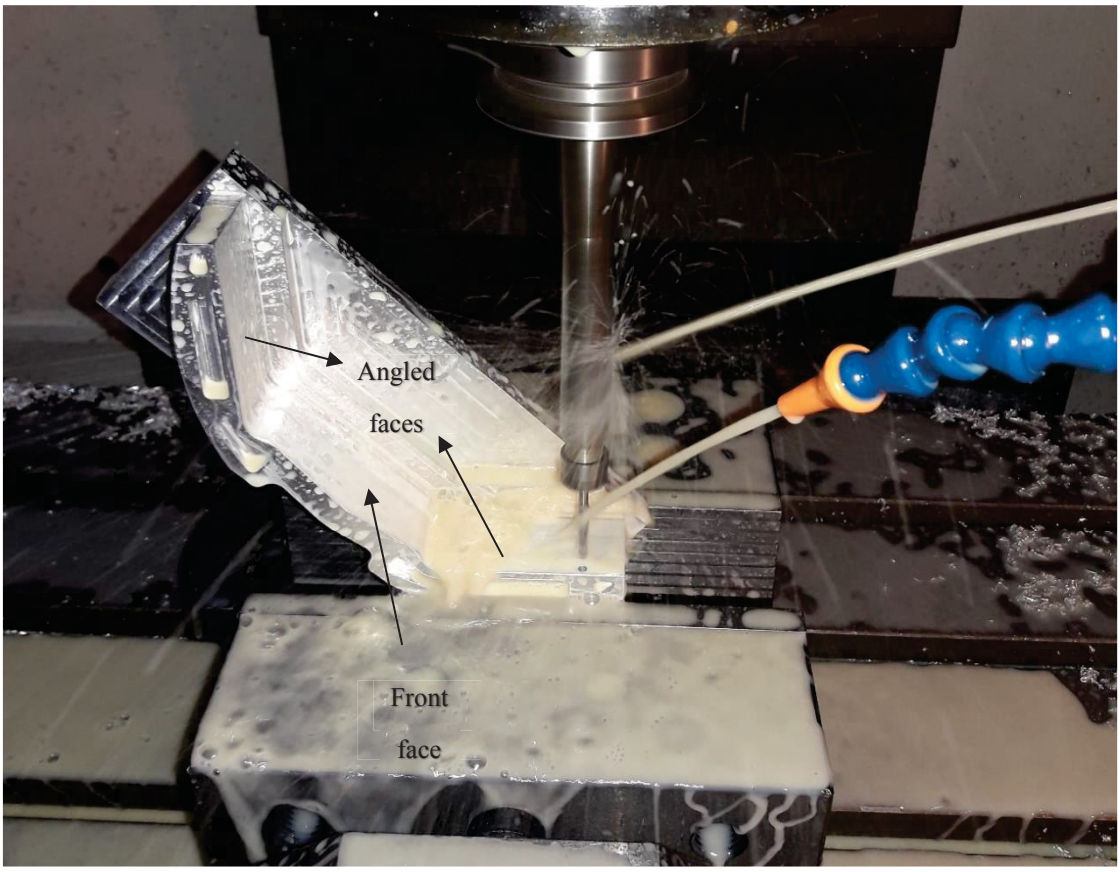

Figure 5.26 Machining of the platform part

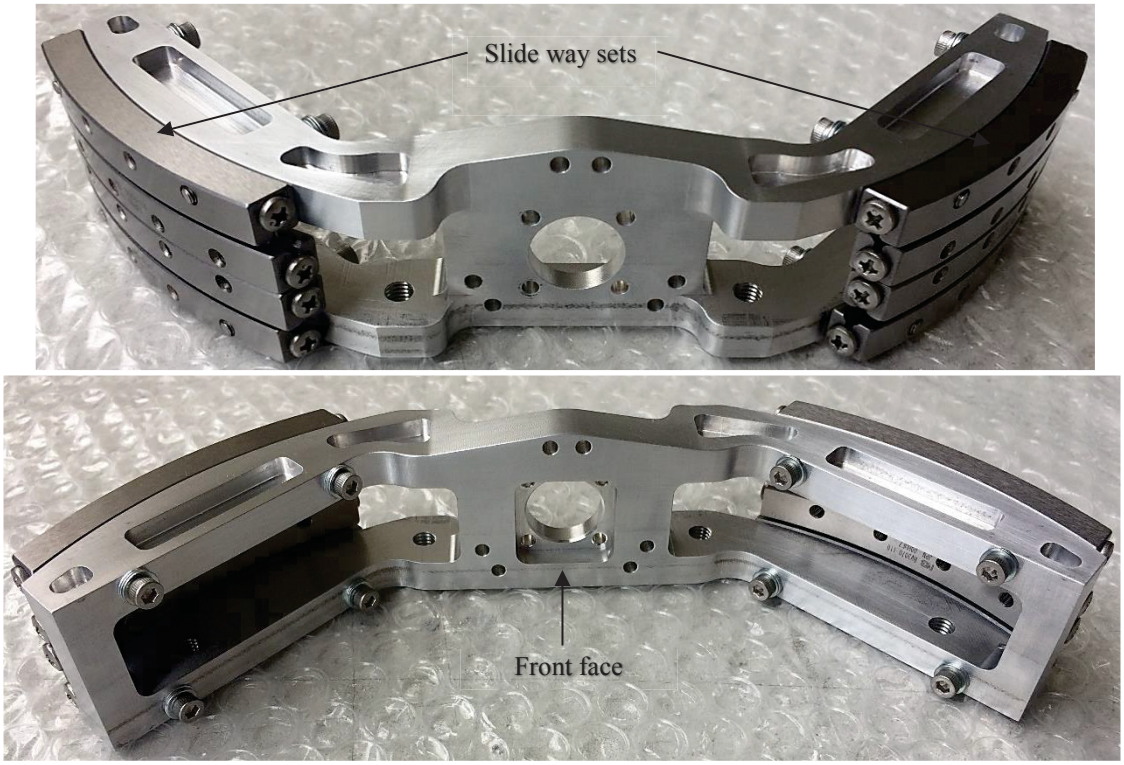

Figure 5.27 Manufactured platform part with the slide ways

Figure 5.28 Fixture apparatus for the capstan parts

After contouring the capstan discs and machining the cavities, the parts were ready to be drilled for M4 setscrew holes in the side extensions. In Figure 5.29, the lateral capstan discs before drilling the setscrew holes in the side extensions are shown.

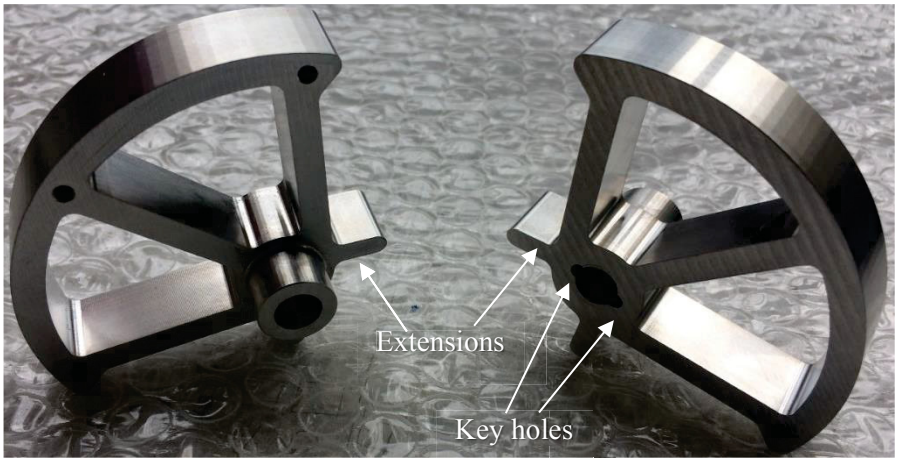

Figure 5.29 Manufactured lateral capstan discs

As can be noticed in Figure 5.29, the keyways are not rectangular. Because the keys are relatively small (2x2x10 mm), it was needed to use very small size (smaller than 1 mm diameter) drilling bits for the radii on the edge of the keyways. To avoid that, drilling the keyway a bit bigger was a solution. However, this might cause a backlash problem. Therefore, the key design in the whole parts were changed to circular pins from

rectangular keys in order not to lose rigidity of the connection between the capstan disc and the shaft passing through it. In Figure 5.30, the capstan disc can be seen with two pins. The result was almost a zero backlash connection.

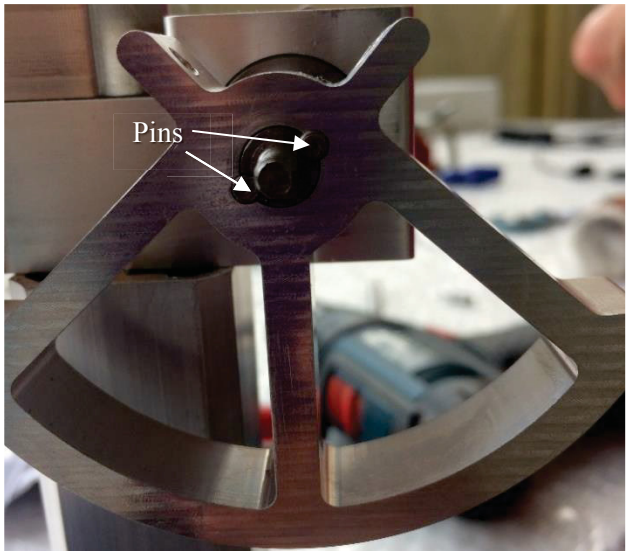

Figure 5.30 Pins used instead of keys in the capstan disc

After the capstan discs, the male and female joint parts were machined with a CNC milling machine without any fixture apparatus. However, when assembling the nylon flanged bushes with the female joint parts, some problems were encountered due to the elasticity of the nylon bushes resulting in unpredictable tolerances. Therefore, instead of the purchased nylon bushes, new bushes are manufactured in the same size by using delrin material (Figure 5.31). Thus, the problem was solved by using stiffer bushes.

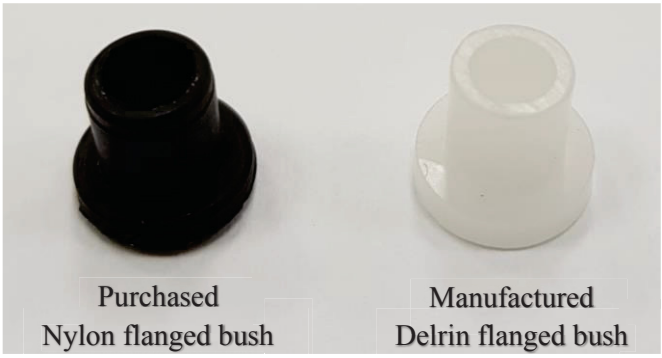

Figure 5.31 Nylon and delrin flanged bush

For a rigid connection, all the steel shafts to be manufactured have two circular keyways placed opposite to each other. In circular shafts, the problematic part is to precisely position the two keyways with respect to each other. After milling the keyways on one side, an apparatus was manufactured to be able to precisely machine the keyways on the other side. Then, the steel shaft was rigidly connected to the apparatus from one side by using a circular key *i.e.* a pin and the keyways on the other side were drilled. As can be seen in Figure 5.32, the shaft was fixed to the apparatus from its bottom keyway to drill the keyways on its top.

Finally, all other parts were manufactured and became ready to be assembled. The assembly process started with the gluing the joint parts and carbon fiber tubes. As a glue, Loctite 9466 epoxy adhesive was used. After gluing, the parts were placed on a machined aluminum surface and some weights were put on each of them to prevent warping while curing (Figure 5.33). As the parts completely cured after 24 hours, all the parts were assembled in an order from the base to the platform.

To move the whole mechanism after the assembly, the mechanism base needed to be raised up due to the rotating motor in the middle leg. So, a fixture part is built to be used during the tests to raise the mechanism up to prevent collisions with table and to fix the mechanism to the table. In Figure 5.34, the assembled mechanism and the fixture part comprising an aluminum plate and aluminum profiles can be seen.

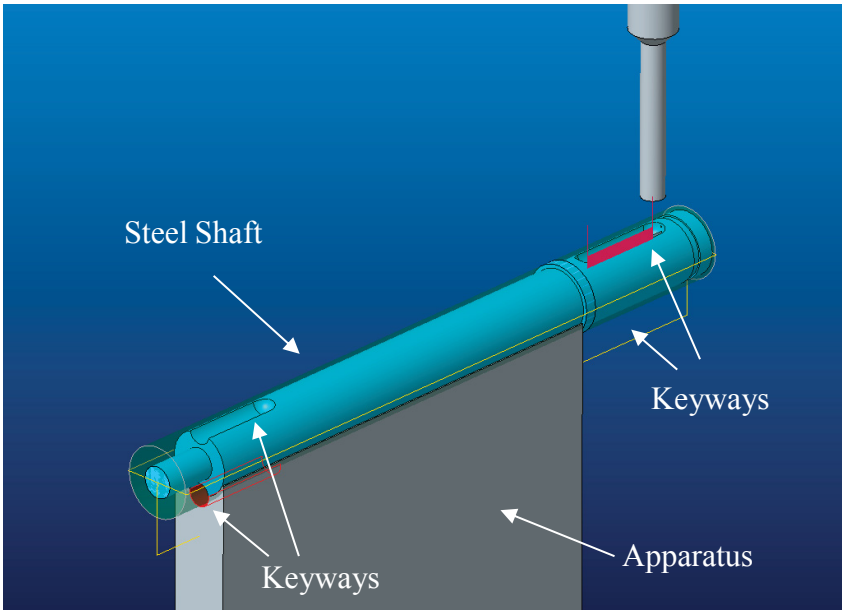

Figure 5.32 Apparatus for steel shafts

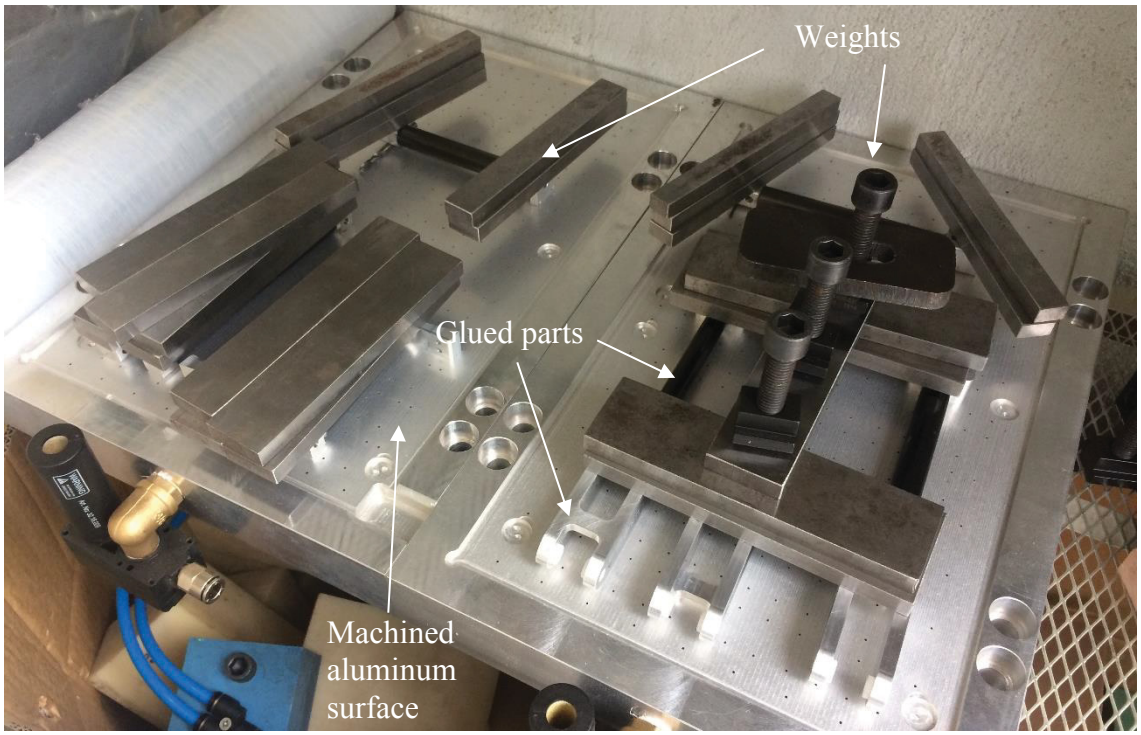

Figure 5.33 Curing process for the glued parts

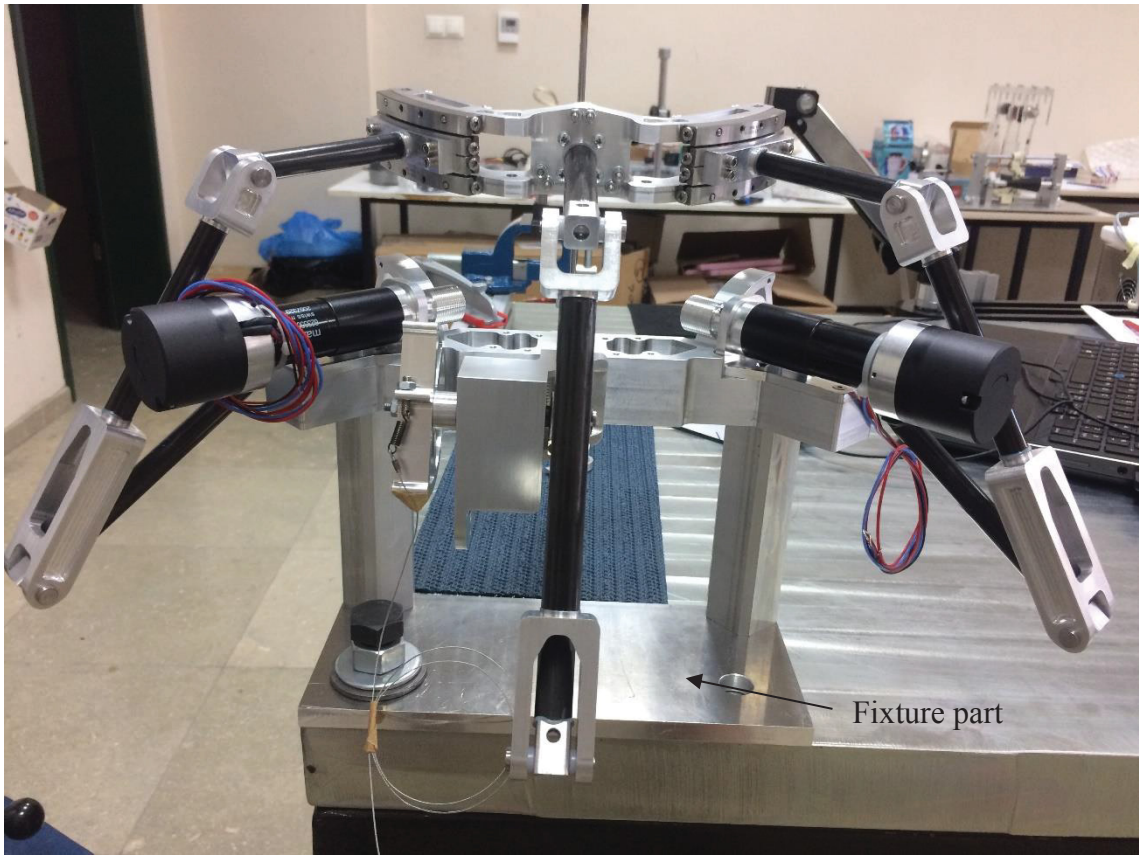

Figure 5.34 Assembled mechanism and the fixture part

5.4 Tests

As the manufacturing process and the assembly of the system were completed, the tests of the system were performed. For testing the system, several apparatuses were manufactured according to the kinematic model of the system. These parts are as follows: telescope model, which is an available product in the market as 4 mm diameter ejector pin for injection mold, telescope holder, RCM hole. Telescope model and RCM hole are used for visualizing the RCM behavior of the mechanism. They are depicted in Figure 5.35. For the measurements, Faro Prime Arm, which is a coordinate measurement machine (CMM) and its computer software CAM2 Measure were used. The test setup is shown in Figure 5.36.

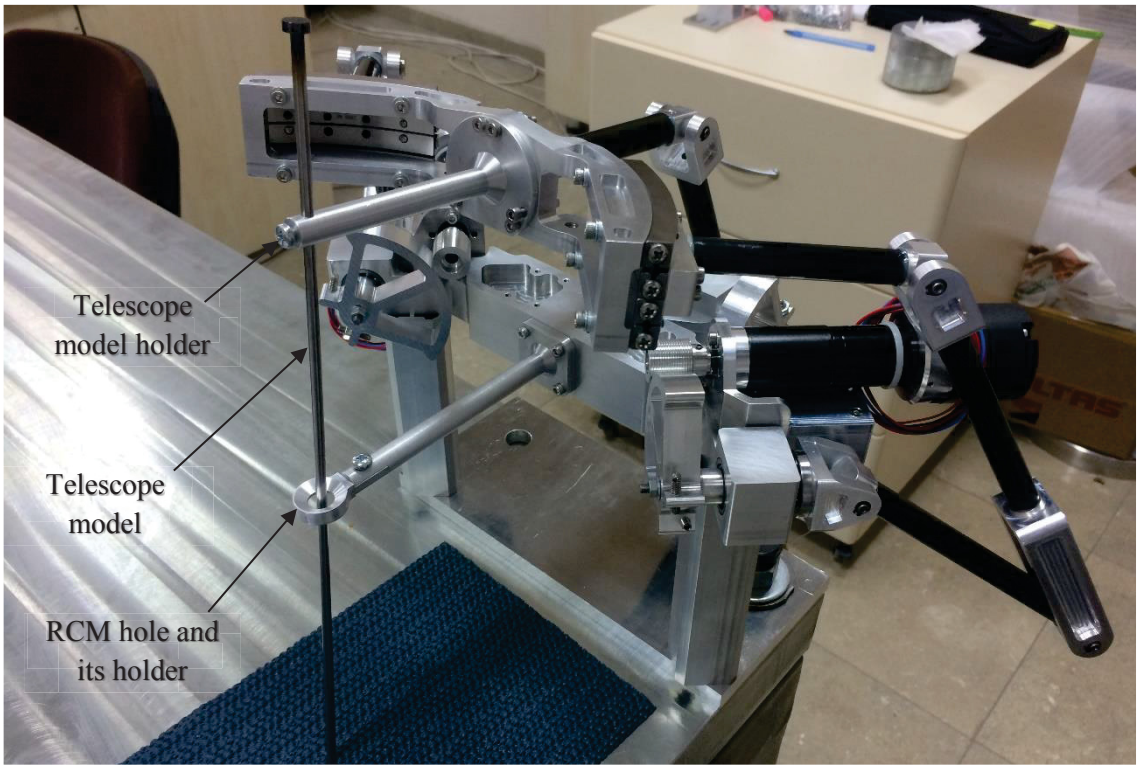

Figure 5.35 Apparatus manufactured for measurements

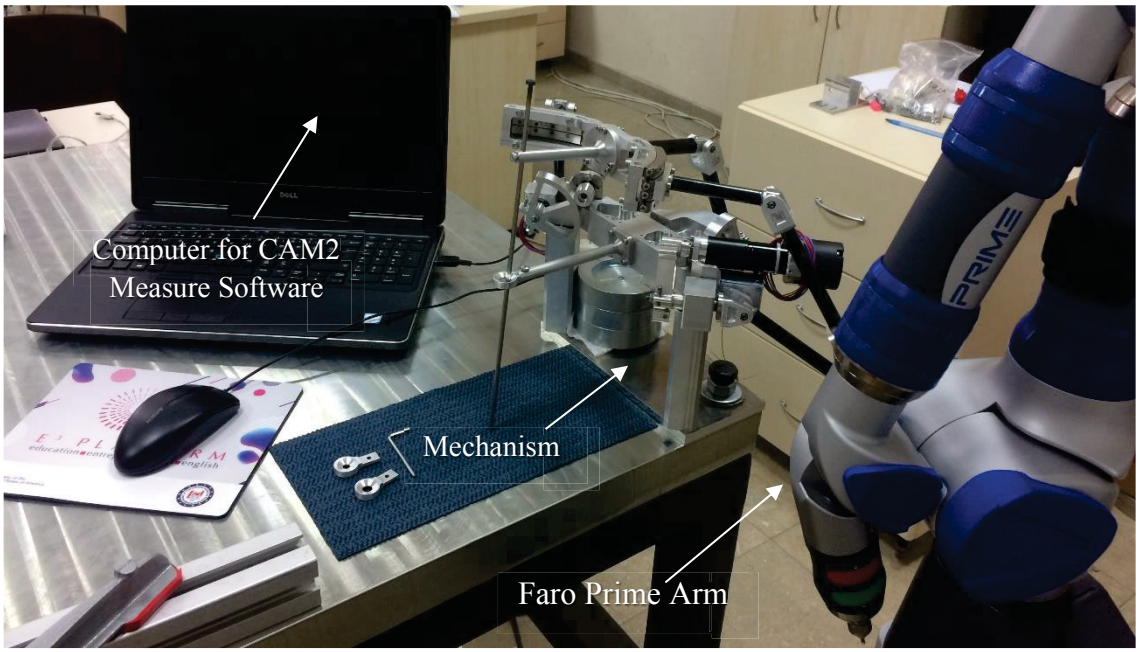

Figure 5.36 Test setup for measurements

First test was to the check kinematic design parameters. The kinematic design parameters to be measured are r_1, a_1, b_1, c_1, r_2, a_2, b_2, c_2, r_3, a_3, b_3, c_3, α_1 and α_2 as depicted in Figure 5.37. Also, $e_1=|D'D''|$ and $e_2=|E'E''|$ are eccentricities due to the manufacturing errors. The values of these parameters are listed in Table 5.4.

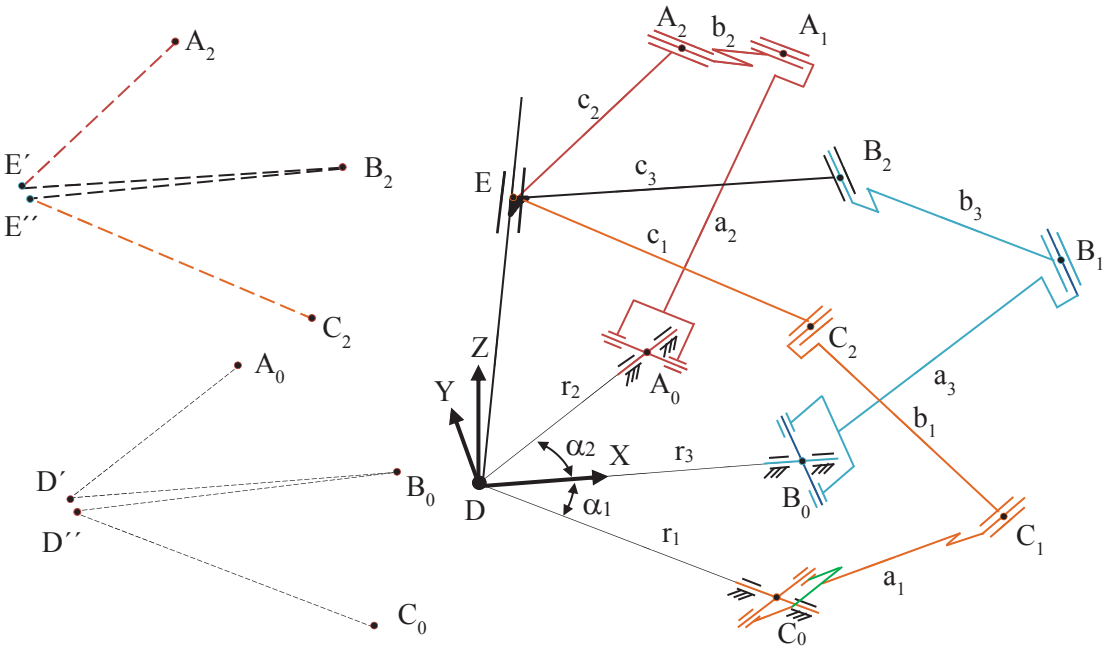

Figure 5.37. Kinematic diagram of the mechanism

As can be seen from Table 5.4, the maximum error of 0,82 mm was measured for r_2 and except that, others have errors less than approximately 0,3 mm. The errors in the link lengths have no effect on the RCM characteristics of the manipulator because the RCM of the manipulator is constructed by the intersecting planes of the legs. They affect the force transmission characteristics of the manipulator. However, e_1 and e_2 errors are directly affects the RCM. Besides, the distortions in the links after glueing the carbon fiber tubes and aluminum parts and the elasticities in the joints affect the RCM because they damage the planarity of the legs. These errors cause some deviations from the RCM point while the manipulator are moving.

The remaining tests and design modifications to eliminate manufacturing errors are future works of the study.

Table 5.4 Measurements of the kinematic parameters

	Dimension	Measured	Calculated	Error	
Leg 1	r_1	200,04	200	0,04	mm
	a_1	134,82	135	0,18	
	b_1	195,04	195	0,04	
	c_1	199,98	200	0,02	
Leg 2	r_2	199,18	200	0,82	
	a_2	135,24	135	0,24	
	b_2	194,69	195	0,31	
	c_2	200,11	200	0,11	
Leg 3	r_3	200,33	200	0,33	
	a_3	135,24	135	0,24	
	b_3	195,16	195	0,16	
	c_3	199,88	200	0,12	
Base	a_1	45°1' 23,23"	45°	1' 23,23"	
	a_2	45°7' 15,14"	45°	7' 15,14"	
	e_1	0,27	0	0,27	mm
Platform	e_2	0,58	0	0,58	

CHAPTER 6

CONCLUSIONS

In this study, the design of a 3-dof surgical robotic arm for minimally invasive transnasal surgery applications is presented. This robotic arm is designed to be capable of 2R1T motion around a remote center of motion. For the synthesis of such a manipulator, the type synthesis method of Kong and Gosselin (2007) is used. In this case, this synthesis method is used to design a structure for a surgical application but it also can be used to develop different structures for any kind of 2R1T-type applications. After synthesis, the resulting manipulators are evaluated according to several evaluation criteria such as ease of dynamic balancing, number of links, structural symmetry, input/output decoupling and number of actuators connected to the base. After evaluation, the best structure is determined as two 1 F_0-system and one 1 F_0-1 F_∞-system leg structure which has 2URRR-URR structure and it has a total degree of overconstraint of 1. Architecture of the selected PM is designed to be suitable for a transnasal surgery by placing its legs on one side of the base so that the mechanism occupies the surgeon's workspace minimally. Then, the rotational and translational motions of the end-effector are synthesized by simplifying the spatial architecture of the PM to three intersecting planes. Thus, dimensional design of the selected PM is performed for the desired workspace and a CAD model is created to determine the constructional details. In the constructional design, carbon fiber and aluminum materials are used to have a lightweight structure. Also, a balancing system consisting of counter-masses and springs is designed for this spatial mechanism. After constructional design being completed, a prototype is manufactured. The tests on the prototype have been initiated, but most of the tests, design modifications and the implementation of the balancing to the manipulator remains as a future work.

REFERENCES

Almeida, P., De Albuquerque, L. A., Fabbro, M. D., Sampaio, M., Medina, R., Chacon, M., & Gondim, J. (2015). Endoscopic skull base surgery: Evaluation of current clinical outcomes. *Journal Of Neurosurgical Sciences*.

Baek, S., & Kim, S. (2014). Robotics in general surgery: An evidence-based review. *Asian Journal of Endoscopic Surgery*, 7(2), 117–123. doi:7. 10.1111/ases.12087.

Berker, M., Isikay I., Berker, D., Bayraktar, M., & Gürlek, A. (2014). Early promising results for the endoscopic surgical treatment of Cushing's disease. Neurosurgical Review, vol. 37, no. 1, pp. 105–114.

Best Spine & Neuro Care In India. (2018, July 15). TNTS (TransNasal TransSphenoidal) Surgery. Retrieved from http://www.bestspinesurgeryhospitalindia.com/tnts.html

Blumenkranz, S.J., & Rosa D.J. (1998). US6441577B2. Washington, DC: U.S. Patent and Trademark Office

Bihlmaier, A. (2016). Learning Dynamic Spatial Relations. doi: 10.1007/978-3-658-14914-7.

Broderick, M.P., Petrenko, S., Raphalovitz, A. & Zhelyaskov, V.(2008). US7395607B1. United States Patent

Cinquin, P., Troccaz, J., Demongeot, J., Lavallee, S., Champleboux, G., Brunie, L., Leitner, F., Sautot, P., Mazier, B., Perez, A., Djaid, M., Fortin, T., Chenic, M., & Chapel, A. (1992). IGOR: image guided operating robot. Innovation et technologie en biologie et médecine, 13, 374–394.

Davies, B.L., Hibberd, R.D. et al. (1996). A Clinically Applied Robot for Prostatectomies. in Taylor RH, Lavallée S, et al., Eds, *Computer-Integrated Surgery: Technology and Clinical Applications*, Cambridge, Massachusetts, USA, MIT Press, pp. 593–601.

Dede, M.I.C., Maaroof, O., Ateş, G., Berker, M., Isikay, I. & Hanalioglu, S. (2017). Unilateral Teleoperation Design for a Robotic Endoscopic Pituitary Surgery System. 101-115. 10.1007/978-3-319-59972-4_8.

Dede M.İ.C., Kiper G., Ayav T., Tatlıcıoğlu E., Özdemirel B., Maaroof O., Ateş G., Berker M., Işıkay İ. & Hanalioğlu Ş. (2018). Cerrahın anlık yönlendirilebildiği

robot yardımlı endoskop kontrol sistemi mimarisi – NeuRoboScope. Türkiye Robotbilim Konferansı (TORK 2018), İstanbul, April 12-14. 25-30.

Gleich A. (2010). DE102010018802A1. Munich, German Patent and Trademark Office

Gogu, G. (2012). *Structural Synthesis of Parallel Robots - Part 4:Other Topologies with Two and Three Degrees of Freedom*, Springer.

Guthart, G. S., & Salisbury, J. K., Jr., (2000), The IntuitiveTM Telesurgery System: Overview and Application. IEEE International Conference on Robotics and Automation (ICRA'00), San Francisco, CA, Apr. 24–28, pp. 618–621.

Hasselvander, R., Zaremba, D., & Legrand, F. (2011). FR2974322A1. Paris: National Institute of Industrial Property

Hourtash A. (2016). US9510911B2. Washington, DC: U.S. Patent and Trademark Office

Intuitive Surgical Inc. (2018, May 20) Retrieved from http://www.intuitivesurgical.com/

Kim, K., Song, H., Park, S., Lee, J. & Yoon, Y. (2010). Design and evaluation of a teleoperated surgical manipulator with an additional degree of freedom for laparoscopic surgery. *Advanced Robotics*, 24, 1697-1718.

Kiper, G., Dede, M.İ.C. & Yaşır A. (2017). Uzak Dönme Merkezli Paralel Manipülatör, TPE 2017/22148 (pending)

Komotar, R.J. (2012). Endoscopic endonasal compared with microscopic transsphenoidal and open transcranial resection of giant pituitary adenomas. Pituitary 15(2), 150–159.

Kong, X. & Gosselin, C. (2007). *Type Synthesis of Parallel Mechanisms*. Springer.

Kuo, C. H. & Dai, J. S. (2009). Robotics for minimally invasive surgery: A historical review from the perspective of kinematics. In International Symposium on History of Machines and Mechanisms, pp. 337-354. doi: 10.1007/978-1-4020-9485-9.

Kuo, C-H. & Dai, J. S. (2012). Kinematics of a fully-decoupled remote center-of-motion parallel manipulator for minimally invasive surgery, *Journal of Medical Devices*, 6, 021008-1.

Kuo, C-H., Dai, J. S. & Dasgupta, P. (2012). Kinematic Design Considerations for Minimally Invasive Surgical Robots: An Overview. *The International Journal of Medical Robotics and Computer Assisted Surgery*. 8 (2). Wiley: 127–45. doi:10.1002/rcs.453.

Kwoh, Y.S., Hou, J. et al. (1988). A Robot with Improved Absolute Positioning Accuracy for CT Guided Stereotactic Brain Surgery, *IEEE Transactions on Biomedical Engineering*, Vol. 35, No. 2, pp. 153–160.

Levy, A. (2004). Pituitary disease: presentation, diagnosis, and management. *Journal of Neurology, Neurosurgery, and Psychiatry*, 75(Suppl 3), iii47–iii52.

Li, Q. & Hervé, J. M. (2010). 1T2R parallel mechanisms without parasitic motion. *IEEE Transactions on Robotics,* 26(3), 401–41 doi: 10.1109/TRO.2010.2047528

Li, J., Zhang, G., Müller, A. & Wang, S. (2013). A family of remote center of motion mechanisms based on intersecting motion planes. *Journal of Mechanical Design*, 135, 091009-1.

Li, J., Xing, Y., Liang, K., & Wang, S. (2015). Kinematic Design of a Novel Spatial Remote Center-of-Motion Mechanism for Minimally Invasive Surgical Robot. *Journal of Medical Devices*, 9, 10.1115/1.4028651.

Liu, S., Chen, B., Caro, S., Briot, S., Harewood, L. & Chen, C. (2016). A cable linkage with remote centre of motion. *Mechanism and Machine Theory*, 105, 583–605. doi: 10.1016/j.mechmachtheory.2016.07.023.

Lum, M. J. H., Friedman, D. C. W., King, G. S. H., Fodero, K., Leuschke, R., Kannaford, B., Rosen, J. & Sinanan, M. N. (2009). The RAVEN: Design and validation of a telesurgery system, *The International Journal of Robotics Research*, 28, 1183–1197.

Madhani, A. J., Niemeyer, G. & Salisbury, J. K. (1998). The black falcon: A teleoperated surgical instrument for minimally invasive surgery, *Proceedings IEEE/RSJ International Conference on Intelligent Robots and Systems*, 2, 936–944, 1998.

Maxon Motor (2018, May 5). Online Shop. Retrived from https://www.maxonmotor.com/maxon/view/catalog/

Mcpherson, M.J., Hobson, A.D., Hayes, M.E., Marvin, C.C., Schmidt, D., Waegell, W., Goess, C., Ohjr, J.Z., Hernandez, A., & Randolph J.T. (2016). WO2017210471A1. Geneva: World Intellectual Property Organization

Nippon Bearing (2018, April 17). Products. Retrived from http://www.nb-linear.co.jp/english/product/pdf/07slide_way.pdf

Popovic, A., & Noonan D.P. (2017). WO2017114860A1. Geneva: World Intellectual Property Organization

Taboada J. (2005). US20060196299A1. Washington, DC: U.S. Patent and Trademark Office

Taniguchi, K., Nishikawa, A., Sekimoto, M., Kobayashi, T., Kazuhara, K., Ichihara, T., Kurashita, N., Takiguchi, S., Doki, Y., Mori, M. & Miyazaki, F. (2010). Classification, design and evaluation of endoscope robots. In: Baik, S. H. (Ed.), *Robot Surgery*. InTech doi: 10.5772/6893.

Taylor, R. H., Menciassi, A., Fichtinger, G. & Dario, P. (2008). Medical Robotics and Computer-Integrated Surgery. *Robotics*, 1199–1222. http://doi.org/10.1007/978-3-540-30301-5

Tetik, H. (2016). *Modelling and Control of a 3-RRS Parallel Manipulator*. (Master's Thesis), İzmir Institute of Technology.

Vierra, M. (1995). Minimally Invasive Surgery, *Annual Review of Medicine*, Vol. 46, pp. 147–158.

Yaşır, A. & Kiper, G. (2018). Structural synthesis of 2R1T type mechanisms for minimally invasive surgery applications. In: Dede MIC, İtik M, Lovasz EC, Kiper G (Eds), *Mechanisms, Transmissions and Applications: Proceedings of the Fourth MeTrApp Conference 2017*, Springer, 31-38.

Zhang, N. & Huang, P. & Li, Q. (2018). Modeling, design and experiment of a remote-center-of-motion parallel manipulator for needle insertion, *Robotics and Computer-Integrated Manufacturing*, Volume 50, Pages 193-202, ISSN 0736-5845, https://doi.org/10.1016/j.rcim.2017.09.014.